

A Census of the Bright $z=8.5\text{--}11$ Universe with the *Hubble* and *Spitzer* Space Telescopes in the CANDELS Fields

STEVEN L. FINKELSTEIN,¹ MICAELA BAGLEY,¹ MIMI SONG,² REBECCA LARSON,^{1,*} CASEY PAPOVICH,³ MARK DICKINSON,⁴
KEELY FINKELSTEIN,¹ ANTON M. KOEKEMOER,⁵ NORBERT PIRZKAL,⁶ RACHEL S. SOMERVILLE,⁷ L. Y. AARON YUNG,⁸
PETER BEHROOZI,⁹ HARRY FERGUSON,⁶ MAURO GIAVALISCO,² NORMAN GROGIN,⁶ NIMISH HATHI,⁶
TAYLOR A. HUTCHISON,^{3,*} INTAE JUNG,^{10,11} DALE KOCEVSKI,¹² LALITWADEE KAWINWANICHAKIJ,¹³ SOFÍA ROJAS-RUIZ,^{14,†}
RUSSELL RYAN JR.,⁶ GREGORY F. SNYDER,⁶ AND SANDRO TACCHELLA¹⁵

¹*Department of Astronomy, The University of Texas at Austin, Austin, TX, USA*

²*University of Massachusetts, Amherst, MA, USA*

³*George P. and Cynthia Woods Mitchell Institute for Fundamental Physics and Astronomy, Department of Physics and Astronomy, Texas A&M University, College Station, TX, USA*

⁴*National Optical-Infrared Astronomy Research Laboratory, Tucson, AZ, USA*

⁵*Space Telescope Science Institute, Baltimore, MD 21218, USA*

⁶*Space Telescope Science Institute, Baltimore, MD, USA*

⁷*Center for Computational Astrophysics, Flatiron Institute, NY, USA*

⁸*NASA/Goddard Space Flight Center, Greenbelt, MD, USA*

⁹*University of Arizona, Tucson, AZ, USA*

¹⁰*Astrophysics Science Division, Goddard Space Flight Center, Greenbelt, MD 20771, USA*

¹¹*Department of Physics, The Catholic University of America, Washington, DC 20064, USA*

¹²*Department of Physics and Astronomy, Colby College, Waterville, ME, USA*

¹³*Kavli Institute for the Physics and Mathematics of the Universe, The University of Tokyo, Kashiwa 277-8583 (Kavli IPMU, WPI), Japan*

¹⁴*Max-Planck-Institut für Astronomie, Königstuhl 17, D-69117, Heidelberg, Germany*

¹⁵*Center for Astrophysics | Harvard & Smithsonian, Cambridge, MA, USA*

ABSTRACT

We present the results from a new search for candidate galaxies at $z \approx 8.5\text{--}11$ discovered over the 850 arcmin² area probed by the Cosmic Assembly Near-Infrared Deep Extragalactic Legacy Survey (CANDELS). We use a photometric redshift selection including both *Hubble* and *Spitzer Space Telescope* photometry to robustly identify galaxies in this epoch at $H_{160} < 26.6$. We use a detailed vetting procedure, including screening against persistence and stellar contamination, and the inclusion of ground-based imaging and followup *Hubble Space Telescope* imaging to build a robust sample of 11 candidate galaxies, three presented here for the first time. The inclusion of *Spitzer*/IRAC photometry in the selection process reduces contamination, and yields more robust redshift estimates than *Hubble* alone. We constrain the evolution of the rest-frame ultraviolet luminosity function via a new method of calculating the observed number densities without choosing a prior magnitude bin size. We find that the abundance at our brightest probed luminosities ($M_{UV} = -22.3$) is consistent with predictions from simulations which assume that galaxies in this epoch have gas depletion times at least as short as those in nearby starburst galaxies. Due to large Poisson and cosmic variance uncertainties we cannot conclusively rule out either a smooth evolution of the luminosity function continued from $z=4\text{--}8$, or an accelerated decline at $z > 8$. We calculate that the presence of seven galaxies in a single field (EGS) is an outlier at the 2σ significance level, implying the discovery of a significant overdensity. These scenarios will be imminently testable to high confidence within the first year of observations of the *James Webb Space Telescope*.

Keywords: early universe — galaxies: formation — galaxies: evolution

1. INTRODUCTION

The epoch of reionization marks the time when the first luminous sources in the Universe, presumably massive stars in nascent galaxies, began to impact the universe around them. Ionizing ultraviolet (UV) photons from these early objects leaked into the intergalactic medium (IGM), beginning the process of ionizing the pervasive hydrogen (and singly-ionizing helium) gas. Significant effort has gone into studying the end of this process, with a general consensus that reionization is complete by $z \sim 6$ (e.g., Fan et al. 2006; Pentericci et al. 2018), with some islands of neutral gas remaining to $z \sim 5.5$ (e.g. Becker et al. 2015; Kulkarni et al. 2018; Becker et al. 2021).

Studies of galaxies have concluded that if the ionizing photon escape fraction is high enough ($\sim 10\text{--}20\%$) then the observed galaxy population, extrapolated to a reasonable level beyond the limits of modern observations, can supply the necessary ionizing photons (e.g., Finkelstein et al. 2010, 2012a, 2015c; Robertson et al. 2013, 2015; Bouwens et al. 2015a; Naidu et al. 2020). The reionization history implied by these moderately-leaking galaxies is one with a very slow beginning and a rapid rise in the ionized fraction at $z < 8$ for a “late reionization” scenario. However, theoretical models predict that it is likely the tiniest dwarf galaxies which have the highest escape fractions due to feedback processes more easily clearing channels for escape (e.g. Paardekooper et al. 2015; Xu et al. 2016), with the massive, presently observable galaxies, contributing little (e.g., Yung et al. 2020). Finkelstein et al. (2019) explored reionization scenarios adopting these simulation-based escape fractions, and found that reionization can still be completed by $z \sim 5.5$ with population-averaged escape fractions of $< 5\%$ (and a small contribution by active galactic nuclei at $z < 6$). The reionization history in this scenario evolves more slowly than previous models as the dependence on very faint galaxies yields an earlier start to reionization and a quasi-linear evolution in the ionized fraction through the end of reionization. Both scenarios are consistent with *Planck* measurements of the electron scattering optical depth to the cosmic microwave background (CMB, Planck Collaboration et al. 2016).

These scenarios differ the most at $z \sim 9$, where the former scenario implies a low ionized fraction of $\sim 20\%$, and the latter implies a larger $\sim 50\%$ ionized fraction.

Moving robust studies of the galaxy populations to $z > 8$ thus has the power to observationally constrain these models, helping improve our understanding of reionization. Observing galaxies at $z > 8$ also pushes us closer to the epoch when we expect the first galaxies to be forming ($z \sim 10\text{--}15$), constraining the formation of the first massive galaxies at these epochs, measuring their chemical enrichment, placing constraints on their star-formation histories, and exploring whether the physics which regulate star formation are evolving to the earliest times (Behroozi & Silk 2015; Finkelstein et al. 2015b; Stefanon et al. 2017a; Tacchella et al. 2018; Behroozi et al. 2020; Yung et al. 2020).

Understandably, after the first big near-infrared surveys with Wide Field Camera 3 (WFC3) on the *Hubble Space Telescope* (*HST*) robustly constrained the $z = 4\text{--}8$ galaxy population (e.g. McLure et al. 2013; Finkelstein et al. 2015c; Bouwens et al. 2015b), attention turned to the $z > 8.5$ universe. This is more difficult, as at $z \sim 9\text{--}10$, the Ly α break is passing through the WFC3 F125W filter, with most deeply covered regions of the sky being covered by only F160W imaging fully redward of the break (though a few small fields include F140W to a commensurate depth).

The first large sample of $z > 8.5$ candidate galaxies was published by Oesch et al. (2013), who found nine candidate $z \geq 9$ candidate galaxies in the Hubble Ultra Deep Field (HUDF, Beckwith et al. 2006) and Great Observatories Origins Deep Survey (GOODS Giavalisco et al. 2004a) South field using Lyman break color-color selection. This was followed up by Oesch et al. (2014), who did a similar search in the GOODS-North field, finding four surprisingly bright candidates at $z \sim 9\text{--}10$, including a source with a grism spectroscopic redshift of $z = 11.1$ (Oesch et al. 2016). At a similar time, Bouwens et al. (2015b) also used color selection to identify six candidate $z \sim 10$ galaxies in the two GOODS fields (including two in the HUDF), followed up by Bouwens et al. (2016a) who used additional imaging to find a full sample of 15 $z \sim 9\text{--}10$ galaxies over the five fields from the Cosmic Assembly Near-infrared Deep Extragalactic Legacy Survey (CANDELS; Grogin et al. 2011; Koekoer et al. 2011) fields (inclusive of the bright Oesch et al. objects). Oesch et al. (2018) added a few faint candidate $z \sim 10$ galaxies from the Hubble Frontier Fields survey (Lotz et al. 2017), while recently Bouwens et al. (2019) added a few additional bright sources from a re-analysis of the CANDELS fields, this time using a more inclusive photometric-redshift selection (updated again in Bouwens et al. 2021). Each of these studies examined the implications of their sample on the evolution

* NSF Graduate Fellow

† Fellow of the International Max Planck Research School for Astronomy and Cosmic Physics at the University of Heidelberg (IMPRS-HD)

of the rest-UV luminosity function, and they each concluded that the evolution from $z = 8$ to 10 is more rapid (per unit redshift) than at $z = 4\text{--}8$, where the decline with increasing redshift is observed to be smooth (e.g., Finkelstein et al. 2015c; Bouwens et al. 2015b; Finkelstein 2016).

Other groups have also explored this epoch. McLeod et al. (2015) and McLeod et al. (2016) used photometric redshift selection to select $z \sim 9\text{--}10$ galaxies from the narrow yet deep HUDF and HFF fields. They concluded that the integrated luminosity density at these redshifts is consistent with a continued smooth decline, and not an accelerated drop-off, when integrating down to similar magnitudes as previous studies ($M_{UV} = -17.7$). Ishigaki et al. (2018) also used data from the HFF survey, making the interesting point that they too find an accelerated decline at $z > 8$ in the UV luminosity density when integrating to $M_{UV} = -17$ (as previous studies did), but when they integrate to -15 , the decline is smooth. This should be unsurprising, as at earlier times, one may expect more of the luminosity density to come from less luminous systems (e.g., due to the evolution of the halo mass function). Bowler et al. (2020) used ground-based imaging from the UltraVISTA survey finding seven even brighter galaxies at $z > 8$. Their calculated luminosity function was also in excess of that predicted from a smoothly evolving Schechter function, potentially indicating a double power-law shape as has been found at $z \sim 6\text{--}7$ (Bowler et al. 2014, 2015). Other studies searching for bright galaxies in this epoch from *HST* pure parallel surveys such as the Brightest of Reionizing Galaxies (BoRG) survey have explored a new parameter space, probing several randomly-placed fields across the sky, with results less susceptible to cosmic variance. Interesting, several studies from different teams with these data have found more bright galaxies than expected, more consistent with a non-accelerated decline in the luminosity density at $z > 8$ (Trenti et al. 2011; Calvi et al. 2016; Bernard et al. 2016; Morishita et al. 2018; Rojas-Ruiz et al. 2020; Roberts-Borsani et al. 2021). While these data are less deep than the legacy fields such as CANDELS, and thus potentially more prone to contamination, the ~ 100 independent pointings also provide a more robust probe of the underlying density field.

There is thus considerable uncertainty about the evolution of the UV luminosity density, and hence the star-formation rate (SFR) density to the highest redshifts presently accessible. The underlying evolution will soon be revealed in high fidelity with the launch of the *James Webb Space Telescope (JWST)* and its associated early-release science and guaranteed time programs, such as

the Cosmic Evolution Early Release Science (CEERS) survey (Finkelstein et al. 2017), the JWST Advanced Deep Extragalactic Survey (JADES, Williams et al. 2018), and the lensing program “Through the Looking Glass” (Treu et al. 2017), as well as several other recently approved large Cycle 1 General Observer programs. However, more insight can be gleaned from a re-examination of the existing data, focusing on three aspects.

First, the majority of previous studies, in particular those which concluded that there is an accelerated decline in the luminosity density at $z > 8$, used simple color-selection to identify their candidate galaxies. While this is a robust way to identify galaxy candidates, it requires galaxies to satisfy strict color criteria, which means that photometric scatter can remove otherwise valid candidates from a galaxy sample. Photometric redshift-based selection makes no such color cuts, though it is necessary to implement “quality control” using the redshift probability distribution function measured during this process. A number of previous studies have noted the inclusivity of photometric redshift selection when opting to use this technique (e.g. McLure et al. 2010; Finkelstein et al. 2010; Ellis et al. 2013; Finkelstein et al. 2015c; McLeod et al. 2016), which also has the advantage in that it provides information on plausible low-redshift alternatives. Second, previous studies were heterogeneous in their usage of available *Spitzer*/IRAC imaging, with some studies using it in the original selection, while others first select galaxies with *HST* imaging only, and then examine the IRAC imaging in a separate step. As we discuss below, when used in the sample selection process IRAC imaging has tremendous leveraging power to probe likely contaminants and increase the robustness of the photometric redshifts at $z > 8$. Finally, three of the CANDELS wide fields lack *Y*-band ($1\ \mu$) imaging, which is just below the $\text{Ly}\alpha$ break at $z \sim 9$. In this work we include new followup *HST* imaging for all selected candidates below the $\text{Ly}\alpha$ break (F098M in most cases) to further increase our confidence in a $z > 8.5$ solution.

In this study, we aim to make a robust census of the $z = 9\text{--}11$ universe in the *HST* CANDELS fields, which have the most complete set of moderately-deep yet wide imaging on the sky with both *HST* and *Spitzer*/IRAC. We make use of the IRAC photometry in the initial sample selection, utilizing a deblending technique to measure accurate IRAC photometry for all but the most crowded sources, which we then use to select a galaxy sample via photometric redshifts. In this paper, we restrict ourselves to the bright end of the luminosity function ($H < 26.6$), as this is the luminosity regime

where *Spitzer* has the greatest constraining power. In §2 we discuss the imaging data we used, and lay out our photometric measurement process, including simulations we ran to justify our detection algorithms. In §3 we describe our sample selection, including our contaminant rejection process. We also discuss our screening for persistence, which can mimic single-band-selected high-redshift galaxies. In §4 we describe the vetting process for our initial sample, making use of all available ground-based photometry and followup *Hubble* imaging, while in §5 we compare to previous galaxy samples in this field. In §6 we present our luminosity function and discuss plausible physical interpretations, and in §7 we discuss a potential overdensity in the EGS field. Our conclusions are presented in §8. In the appendix we show all objects manually removed from our sample for a variety of reasons following visual examination. All magnitudes are presented in the AB system, and we assume a cosmological model with $H_0 = 67.74 \text{ km s}^{-1} \text{ Mpc}^{-1}$, $\Omega_m = 0.309$ and $\Omega_\Lambda = 0.691$, consistent with the latest results from *Planck* (Planck Collaboration et al. 2020).

2. OBSERVATIONS AND CATALOGS

2.1. Imaging

The CANDELS survey (Grogin et al. 2011; Koekemoer et al. 2011) imaged five fields in the sky: GOODS-North, GOODS-South, COSMOS, the UKIDSS Deep Survey (UDS) and the Extended Groth Strip (EGS). The central 50% of each of the GOODS fields was observed longer and represents the CANDELS “deep” survey, while the remaining regions of GOODS, and the other three fields, comprise the CANDELS “wide” survey. One exception is the northern 25% of GOODS-S, which was observed by the WFC3 Early Release Science (ERS) team, and has a depth in between CANDELS wide and deep (Windhorst et al. 2011). Each of these fields had previous *HST* imaging with the optical Advanced Camera for Surveys (ACS), which was also utilized by CANDELS in parallel. The mosaics used here include all such previously available data. The data reduction and mosaic procedure is outlined in Koekemoer et al. (2011). We use the latest available CANDELS internal-team mosaics for each of our fields.

2.2. Catalog Detection Parameters

We use v2.19.5 of the Source Extractor Software (Bertin & Arnouts 1996) to measure photometry of our sources, using two-image mode with the F160W image as the detection image. We set the weight type to MAP_RMS, with the CANDELS-provided rms image as the weight image. This software has a number of user-definable choices which can impact the complete-

ness and purity of a catalog, and the accuracy of the photometry. The primary factors affecting the completeness and purity are DETECT_THRESH (D_σ) and DETECT_MINAREA (D_N). The former is a significance threshold, while the latter is a number of pixels. Source Extractor will extract a source if it has D_N connected pixels with a significance greater than D_σ . In our previous work (Finkelstein et al. 2015c) we assumed $D_\sigma = 0.6$ and $D_N = 7$ (with the same 60 milli-arcsecond pixel scale as we use here). We arrived at these values based on visually inspecting the results of several parameter combinations, attempting to maximize completeness while minimizing inclusion of spurious sources. As our goal in this paper is to push *Hubble* to its limits by probing the $z > 9$ universe, it is crucial to validate these choices via simulations.

To optimize these parameters we performed simulations in each of the five fields, inserting 30,000 simulated sources in the F160W science image. We assumed the sources followed a Sersic light profile, with a half-light radius in arcseconds drawn from a log-normal distribution (e.g., Shibuya et al. 2016) of the form: $r = e^{A+B \times \mathcal{R}}$, where $A = -0.1$ is the central value, $B = 1.8$ is the width, and \mathcal{R} denotes a Gaussian random deviate. This functional form produces a distribution with a peak at 0.2 physical kpc and a relatively shallow decline to a maximum of 1 physical kpc ($\sim 0.25''$), expected for moderately bright $z > 8$ galaxies (e.g., Kawamata et al. 2018). The Sersic index also assumed a log-normal distribution, with a peak at the minimum of $n = 1$, and a tail to $n = 5$; this distribution was much tighter than that of the radius, with the majority of simulated objects having $n < 2$. The axis ratio also had a lognormal distribution, peaked at 0.8, and the position angle was random. These simulated objects were created with the GALFIT package (Peng et al. 2002), and added to the image at random positions.

We then ran Source Extractor on this image in two-image mode, using this modified F160W-band image as both the detection and the measurement image. We ran 18 independent catalogs, testing values of $D_\sigma \in \{0.5, 0.6, 0.7, 0.8, 0.9, 1.0\}$ and $D_N \in \{5, 7, 9\}$. For this test, we used the default Kron aperture for measuring photometry, as this approximately reproduces the total flux. As we know the true flux for each of our sources, we tested this assumption by comparing the input and recovered fluxes for our simulated sources. We found that the ratio of our input flux to that measured in the default Kron aperture was consistently $\sim 1.20 \pm 0.01$ in all five CANDELS fields. We thus applied this aperture correction to all sources for the purpose of these simulations. We matched each of these catalogs to our

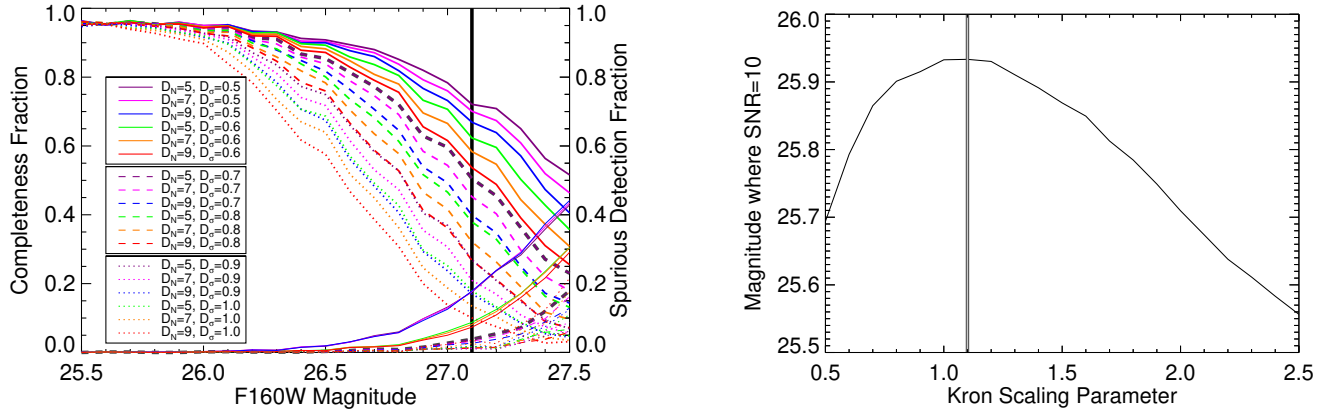


Figure 1. The results from the optimization of our Source Extractor catalogs in the CANDELS EGS field. *Left*) The completeness (thick lines = fraction of recovered simulated sources recovered) and spurious fraction (thin lines = ratio of sources recovered from a negative image to those in the original image) as a function of total F160W magnitude. We used this analysis to select fiducial values of DETECT_THRESH (D_σ) = 0.7 and DETECT_MINAREA (D_N) = 5 pixels, shown as the thickest dashed purple line. This combination maximizes completeness while minimizing contamination. A 20–40% higher completeness is possible, but the catalogs become much less pure, with spurious fractions more than doubling. *Right*) The magnitude where the signal-to-noise ratio is equal to 10 as a function of the Kron scaling parameter k (also for the EGS field). This shows that Kron apertures with a value of $k=1.1$ results in a catalog which is nearly 0.4 mag deeper than the default value of $k=2.5$.

simulated source list, and calculated the completeness as the fraction of sources recovered divided by the total number input into the image in magnitude bins of $\Delta m=0.1$.

To calculate the fraction of spurious sources, we performed another run of Source Extractor for each detection parameter combination, now using a “negative” version of the original science image (created by multiplying each pixel in the original image by -1). Assuming that the background is zero (see Koekemoer et al. 2011 for details on the reduction of these images), any significant “source” in this image is spurious, as it is made up of a random clumping of negative pixels due to noise in the image. We calculated the spurious fraction as the number of sources detected in this negative image in a given magnitude bin divided by the number of sources detected in the original positive image (based on an independent Source Extractor run) in that same magnitude bin.

The result of this exercise is an estimate of both the completeness and spurious detection fraction as a function of magnitude for each of our Source Extractor parameter combinations. In Figure 1 we show the results for the EGS field, comparing both the completeness and the spurious detection fraction to the total 5σ limiting magnitude in this field (where the 1σ noise was estimated as the standard deviation of fluxes measured in randomly placed $0.4''$ -diameter apertures, corrected to total by dividing by the fraction of a point-spread function [PSF] enclosed in a $0.4''$ aperture [0.64 for F160W]).

This figure shows that the completeness at this 5σ limit falls monotonically with increasing values of both D_σ and D_N . The spurious fraction on the other hand shows little dependence on D_N , but a strong dependence on D_σ . We elected to use values of $D_\sigma = 0.7$ and $D_N = 5$ pixels, shown by the dashed purple line. This produces a completeness fraction of 50.5% at the 5σ limiting magnitude in this field, and a spurious fraction (or catalog impurity) of only 3.8% at this limiting magnitude.

As shown in Figure 1, smaller values of D_σ (solid lines) do result in higher completeness fractions (55–70%), but at the cost of significantly higher spurious fractions (8–18%). We decided that a potential 40% gain in completeness was not worth a 2–4 \times increase in the spurious fraction. We emphasize that, though low, our fiducial spurious fraction is non-zero, and we must take care to ensure selected candidate galaxies are not spurious. As discussed below, this is done by imposing a detection significance (i.e., minimal signal to noise) further tuned to eliminate such spurious sources. We note that the Finkelstein et al. (2015c) parameters of $D_\sigma = 0.6$ and $D_N = 7$ pixels result in a completeness fraction 15% higher than our fiducial value, at the cost of a spurious fraction 2.1 \times larger.

We performed this same analysis in all five CANDELS fields (including splitting the GOODS fields into their different depth components). We find that our fiducial choice of detection parameters appears to be preferred in all fields regardless of depth, thus we adopt them for all

Table 1. Quality of the CANDELS Photometric Catalogs

| Field | F160W 5σ | Completeness | Spurious |
|--------------|-----------------|--------------|----------|
| Field | Limiting Mag | Fraction | Fraction |
| EGS | 27.10 | 0.505 | 0.038 |
| COSMOS | 26.87 | 0.486 | 0.061 |
| UDS | 26.92 | 0.526 | 0.066 |
| GOODS-N Deep | 27.64 | 0.634 | 0.029 |
| GOODS-N Wide | 26.98 | 0.586 | 0.094 |
| GOODS-S Deep | 27.47 | 0.615 | 0.025 |
| GOODS-S Wide | 26.79 | 0.426 | 0.068 |

NOTE—The completeness fraction and spurious fraction (i.e., catalog impurity) at the 5σ limiting magnitude in each of the five CANDELS fields for our chosen detection parameters of DETECT_THRESH=0.7 and DETECT_MINAREA=5. The limiting magnitude was measured in a $0.4''$ -diameter aperture, and corrected to total under the assumption of a point-source flux distribution.

fields. In Table 1, we give the completeness and spurious fraction at the typical 5σ depth for each (sub) field.

2.3. Photometric Aperture

We follow our previous works [Finkelstein et al. \(2010, 2012b,a, 2015c\)](#) and make use of small Kron elliptical apertures to measure the colors of objects in our catalog (see also, e.g., [Bouwens et al. 2007, 2015b](#)). These elliptical apertures are tuned to match the shapes of the measured objects, and typically achieve higher signal-to-noise than similarly sized circular or isophotal apertures (e.g., [Finkelstein et al. 2010](#)). Source Extractor parameterizes this radius with a ‘‘Kron factor’’ k and a minimum radius R_{min} . As shown in the Source Extractor manual, the default parameters of $k=2.5$, $R_{min}=3.5$ contain $> 90\%$ of an object’s flux (see further discussion in [Graham et al. 2005](#)). However, this aperture is typically significantly larger than the region defined by the detection threshold for most high-redshift galaxies, and so does not result in the optimal signal-to-noise. It is thus typical to use a smaller Kron factor when measuring colors, with $k=1.2$ commonly used. We explored a range of Kron factors, running several iterations of Source Extractor with Kron factors ranging from 0.5 to 2.5 (keeping the ratio of R_{min}/k fixed to $3.5/2.5$). using the same simulated sources from the preceding subsection. The results are shown in the right panel of Figure 1 for the EGS field (and are similar for the other CANDELS fields). This figure shows the magnitude where a typical source has a signal-to-noise of 10, as a function of

Kron parameter k . This distribution shows a clear peak at $1.0 < k < 1.2$, with a steep decline to higher and lower values. Notably, at the default value of $k=2.5$ a catalog would be nearly 0.4 mag shallower than one using $k=1.1$. We thus adopt $k=1.1$, $R_{min}=1.6$ for color measurements in our analysis.

2.4. Point-Spread Function Matching

To measure accurate colors in constant-sized apertures, it is necessary to match the PSFs of the imaging used. This is relevant as the diffraction limit of *Hubble* varies by $>2\times$ across the wavelength range used here. While this is slightly mitigated as the pixel scale used in our drizzled images (60 mas) results in the bluer-band PSFs being somewhat larger than the diffraction limit in those bands, we find that the effective PSFs in our WFC3/IR images are still significantly larger than that in our ACS images. We therefore match the PSF in all images to that in our F160W images.

The first step is to construct the PSF. As our main concern is accurate colors, we elected to measure empirical PSFs by stacking stars in our images. We selected stars by identifying the stellar locus in a plot of the half-light radius versus magnitude, constructed using a preliminary run of Source Extractor. The exact location of the stellar locus varies from band-to-band (and a bit from field-to-field), thus the stellar selection box was manually derived for each band/field combination. To mitigate the effect of crowding, we only accepted a star as a PSF star if it had no object within $200''$ brighter than one magnitude fainter than the star in question. This preliminary list of PSF stars was then visually inspected, to remove remaining crowded sources, objects near the edge of an image, and non-stellar-like interlopers. The stars which passed this cut were then stacked together, in 101×101 pixel cutouts. During this process, the stars were centered in the cutout by upsampling by a factor of 10, recentering, then sampling back down to the original 60 mas pixel scale. Each star was also rotated by a random amount, such that the final PSF did not contain significant diffraction spikes (this is relevant as some fields were obtained at multiple orient, so the final PSF had several diffraction spikes; the fraction of flux in these spikes is negligible, so we elected to remove them from the PSF in this manner). Each stacked-star PSF then had any remaining residual background subtracted, and was normalized to unity. Example PSFs from the EGS field are shown in Figure 2.

For each field, we created kernels to match the individual PSFs to that in the F160W band in each field using

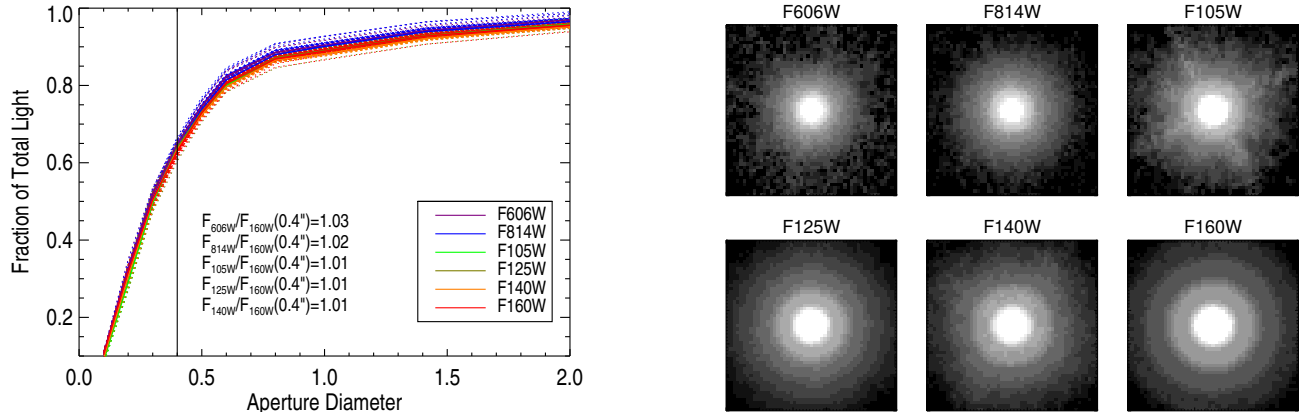


Figure 2. *Left*) The curve-of-growth measured for stars in the EGS field after the implementation of PSF matching. The thin dotted lines show individual stars, while the thick solid lines show the average. The vertical line indicates an aperture diameter of $0.4''$, while the inset text highlights that all images have an enclosed flux within 3% of the F160W image at this diameter. *Right*) Empirical stacked-star point-spread-functions for the six images in the EGS field. These cutout images show the central 51×51 pixels ($\sim 3''$), and are displayed with logarithmic scaling. The measured full-width at half-maximum for these PSFs are $0.142''$, $0.147''$, $0.208''$, $0.222''$, $0.223''$, and $0.234''$ for F606W, F814W, F105W, F125W, F140W and F160W.

the `pypher` Python routine¹. Each image was then convolved with its respective kernel. To examine the accuracy of this PSF homogenization process, we measured the curves-of-growth of the identified stars in these images, and compared those from each band to the F160W band. In nearly all cases, the enclosed flux at a radius of $0.4''$ matched that in the F160W band to within 1-3%. We show the results from the EGS field in Figure 2.

2.5. Catalog Construction

Using the conclusions from the above tests, we proceeded to construct our photometric catalog in each of our fields. For each catalog, we used the F160W image as the detection image, and cycled through every available image as the measurement image. For the remainder of this paper, we will refer to filters by their characteristic letter, with their three-number identifier in a subscript (e.g., F160W \rightarrow H_{160}). The EGS, COSMOS and UDS fields are fully covered by the V_{606} , I_{814} , J_{125} , JH_{140} and H_{160} filters. We note that the JH_{140} was obtained as direct imaging for the 3D-HST slitless spectroscopy program (Momcheva et al. 2016), and is thus quite shallow. We also used available Y_{105} data in these fields, which consists of a few pointings obtained to followup potential high-redshift sources (PID 13792, PI Bouwens). The two GOODS fields contain these same filters (including full-field Y_{105} coverage), as well as full-field coverage in the B_{435} , i_{775} , and z_{850} filters. The exception is the ERS region of GOODS-S, which has

Y_{098} rather than Y_{105} . We collate the Source Extractor results into a single catalog per field, including several measures of the photometry (e.g, Kron, isophotal, and circular apertures). Fluxes and errors in all filters were corrected for Galactic extinction assuming a Cardelli et al. (1989) Milky Way attenuation curve, with $E(B-V) = 0.006, 0.016, 0.019, 0.010$ and 0.008 for the EGS, COSMOS, UDS, GOODS-N and GOODS-S fields, respectively.

2.5.1. Aperture Correction

Our default photometry consists of colors measured in the small Kron aperture, corrected to total using an aperture correction. To calculate the appropriate aperture correction, we performed one additional run of Source Extractor per field with the H_{160} -band as the measurement image, this time with the default larger Kron parameters, which as mentioned above approximately recover the total flux. The aperture correction is thus the ratio of the flux measured in this larger Kron aperture to that in our tuned smaller Kron aperture. As we discovered in our simulations in §2.2, even this larger Kron aperture fails to recover the flux in the wings of the PSF. Our simulations found that an additional 20% correction was needed to recover the total flux of simulated sources. Our final aperture correction thus includes this additional multiplicative factor. As all images have been PSF-matched to the H_{160} -band PSF, we apply this H_{160} -measured aperture correction to all filters, though we again reiterate that colors are measured in small Kron apertures.

2.5.2. Empirical Noise Estimation

¹ <https://pypher.readthedocs.io>

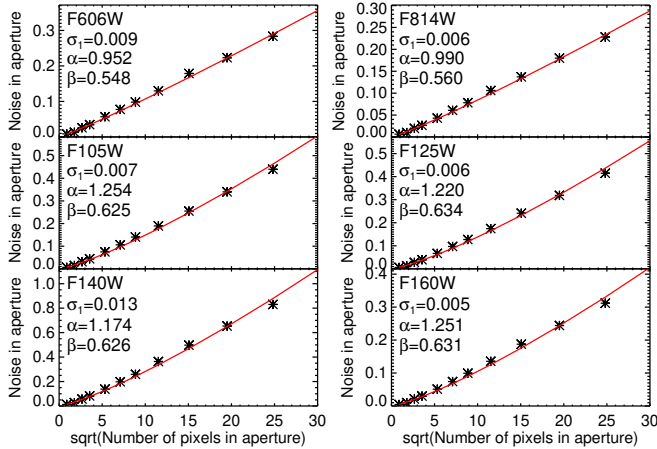


Figure 3. The results of our empirical noise simulations for each filter in the COSMOS field. The data points show the measured σ from a Gaussian fit to the negative side of the flux distribution in randomly placed apertures of different sizes (plotted versus the square root of the number of pixels in the aperture). The red line shows the fit to the data using Equation 1, with the parameters of the fit inset in the panels. This fits were used to calculate the noise for each object given the number of pixels in its custom Kron aperture.

While Source Extractor provides a noise estimate based on the provided rms map, we have elected to calculate our noise empirically. We follow the procedure outlined in Papovich et al. (2016), omitting the Poisson correction, as our sources of interest will be faint and this noise component will be negligible (see also Wold et al. 2019, Rojas-Ruiz et al. 2020 and Stevans et al. 2021 for implementations of this procedure). This calculation relies on measuring the noise fluctuations as a function of the number of pixels in an aperture. We do this by measuring the flux at 10^4 random positions in each science image. We do this with Source Extractor, making a detection image which contains zeroes at all locations, except at these random positions, where we set the pixel values to 1.0. At each of these positions, we measure the flux in 12 circular apertures, ranging from 1–35 pixels (0.06 – 2.1”) in diameter. For each of these aperture diameters, we measure the noise as the spread in the 10^4 measured values. We do this by fitting a Gaussian to the negative side of the measured flux distribution, to omit any positive flux from real sources. The measured σ value from this Gaussian fit is thus the 1σ noise value in an aperture of that size.

Inspecting these measured σ values, it is apparent that, as expected, there is a clear dependence of the noise on the number of pixels in an aperture. We were able to robustly fit a curve to this distribution using the

functional form of:

$$\sigma_N = \sigma_1 \alpha N^\beta \quad (1)$$

where σ_N is the noise in an aperture containing N pixels, and σ_1 is the pixel-to-pixel noise (measured in each image as the sigma-clipped standard deviation of all pixels, omitting pixels belonging to real objects using the Source Extractor segmentation map), following several previous works (e.g., Labbé et al. 2007; Whitaker et al. 2011; Papovich et al. 2016). The parameters α and β are free parameters, which we fit for using the IDL implementation of MPFIT. We note that Papovich et al. (2016) had an extra term in their noise equation ($\sigma_1 \gamma N^\delta$), however, in our exploration, we were able to achieve good fits with just the two free parameters. We show an example of these fits for the COSMOS field in Figure 3.

To calculate the noise for a given source, we calculated N for our Kron aperture using the Source Extractor measured ellipse properties (KRON_RADIUS, A_IMAGE and B_IMAGE), and using a given aperture diameter for the circular apertures. Lastly, these noise estimates were multiplied by the ratio of the rms image value at the central position of a given source to the median rms value of the whole map, thereby allowing the noise to be representative of the local noise level. In Table 2 we list the implied 5σ point-source depths for each filter and field using these noise functions. As a sanity check, we calculated the ratio between our adopted empirical errors to the Source Extractor calculated errors, finding a median ratio of ~ 0.8 – 0.9 in the catalogs for all five fields.

2.5.3. IRAC Photometry with TPHOT

We performed IRAC photometry on the final SCANDELS 3.6 and 4.5 μm mosaics in the five CANDELS fields (Ashby et al. 2015), which achieve a total integration time of at least 50 hr for most of the area used in this study. Because IRAC images have significantly lower spatial resolution (PSF FWHM $\sim 2''$) than *HST*/WFC3 ($\sim 0.2''$), multiple sources in the *HST*/WFC3 imaging may appear blended together in the IRAC imaging. To mitigate the effect of source confusion in IRAC on flux estimation, we performed PSF-matched IRAC photometry using information in a high-resolution image as a prior. Specifically, we exploited the T-PHOT software (Merlin et al. 2015, 2016), using our H_{160} detection image as a prior and the IRAC PSF as transfer kernel between the *HST* H_{160} -band and IRAC data, following the procedure outlined in Song et al. (2016).

The IRAC PSF was constructed by identifying and stacking point sources in the IRAC mosaics. Simi-

Table 2. Limiting Magnitudes in *HST* Imaging

| Field | B_{435} | V_{606} | i_{775} | I_{814} | z_{850} | Y_{098}^* | Y_{105} | J_{125} | JH_{140} | H_{160} |
|--------------|-----------|-----------|-----------|-----------|-----------|-------------|-----------|-----------|------------|-----------|
| EGS | — | 27.95 | — | 27.60 | — | — | 26.79 | 27.05 | 26.36 | 27.10 |
| COSMOS | — | 27.63 | — | 27.31 | — | — | 26.93 | 26.94 | 26.33 | 26.87 |
| UDS | — | 27.63 | — | 27.53 | — | — | 27.01 | 26.96 | 26.23 | 26.92 |
| GOODS-S Wide | 28.04 | 28.43 | 27.71 | 27.80 | 27.46 | 27.32 | 27.02 | 27.14 | 26.24 | 26.79 |
| GOODS-S Deep | 28.20 | 28.59 | 27.96 | 28.13 | 27.52 | — | 27.74 | 27.79 | 26.34 | 27.47 |
| GOODS-N Wide | 27.99 | 28.06 | 27.82 | 27.92 | 27.40 | — | 27.01 | 27.13 | 26.59 | 26.98 |
| GOODS-N Deep | 28.01 | 28.23 | 28.14 | 28.46 | 27.59 | — | 27.66 | 27.94 | 26.69 | 27.64 |

NOTE—The listed values are 5σ limiting magnitudes measured in $0.4''$ -diameter apertures, and corrected to total assuming a point source flux distribution. Y_{098}^* data is only available in the northern section of GOODS-S (in the WFC3 “Early Release Science” field).

lar to §2.4, we first identified point sources in each band in a half-light radius versus magnitude diagram in IRAC imaging. Then, we visually inspected them in the *HST*/ H_{160} and IRAC data, to make sure that they appear to be point sources in the *HST* imaging and not to be severely blended with nearby sources in either IRAC band. “Clean” point-sources for each field identified from the above step were then over-sampled to the pixel scale of the *HST*/ H_{160} image, registered, normalized, and median-combined to create the final IRAC PSFs in each band and in each field.

Before feeding the *HST* segmentation map into T-PHOT, we enlarged the segmentation map using the program `dilate` (DeSantis et al. 2017). This is to account for the previous finding that Source Extractor tends to underestimate the isophotal area of fainter objects more (Galametz et al. 2013; Guo et al. 2013). To prevent their IRAC fluxes measured based on isophotes from being underestimated, we thus enlarged the segmentation map using the factor devised by the CANDELS team (Galametz et al. 2013; Guo et al. 2013).

The IRAC fluxes for each source detected in the *HST* imaging were then measured with T-PHOT. In T-PHOT, models for the IRAC data for each source were generated by convolving the enlarged segmentation map with a transfer kernel, leaving the IRAC flux as free parameter. The best-fit IRAC fluxes were then obtained by solving for the solution that best-matches the observed IRAC data. We refer the reader to Song et al. (2016) for full details.

3. SAMPLE SELECTION

One concern when selecting such distant galaxies is sample contamination. The number of $z > 8$ galaxies in these *HST* data are likely few, and contaminating objects at lower redshifts with similar colors likely

outnumber our galaxies of interest. With this in mind, previous work in this epoch typically employs a highly conservative sample selection, including strict color-cuts designed to rule out these interlopers. While the upcoming *James Webb Space Telescope*, with its larger collecting area and longer wavelength baseline will significantly improve our knowledge of galaxy evolution in this epoch, we can make gains now by using all available imaging when selecting galaxies. Specifically, *Spitzer*/IRAC photometry is not often used as a primary observable when selecting galaxies, due to its shallower depth, and larger point-response function size. However, the CANDELS fields all now have deep 50 hr imaging at both 3.6 and 4.5 μm from the S-CANDELS survey (§2.5.3), extending to $m_{3\sigma} \sim 26.5$, reaching the potential rest-optical brightnesses expected for our objects of interest.

In the left panel of Figure 4, we highlight this issue further, showing a model spectrum of a $z = 9$ galaxy, compared to likely contaminants, including a passive galaxy at $z = 2.2$, a dusty-star-forming galaxy (Casey et al. 2014) at $z = 2.2$, and example M, L and T brown dwarfs. This figure highlights that these objects all have very similar observed colors at $\sim 1.2\text{--}1.8 \mu\text{m}$, the wavelengths where we detect light from true $z > 8$ galaxies with *HST*. While these contaminants all have flux at shorter wavelengths, it is weak, and often not detectable at typical *HST* depths. However, moving to redder wavelengths, these objects have divergent colors. The spectral energy distribution (SED) of a true high-redshift galaxy is mostly flat, with a potential small jump due to the Balmer break (depending on the age of the galaxy, e.g., Roberts-Borsani et al. 2020; Laporte et al. 2021) or nebular emission lines (not shown for clarity). The $z = 2.2$ galaxies are both much brighter due to their intrinsically red SEDs, while the potential stellar contaminants become blue at these wavelengths, as we are probing

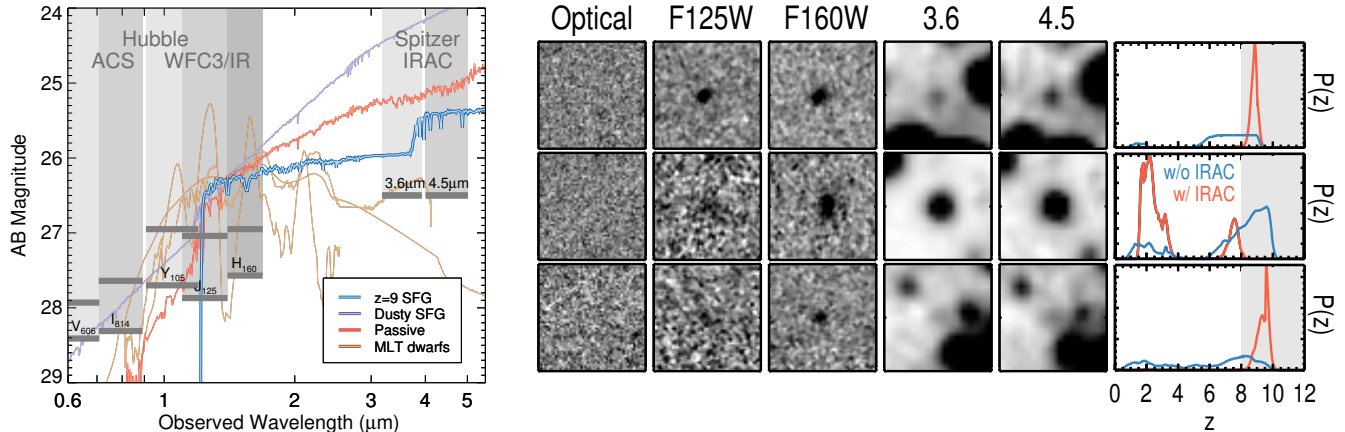


Figure 4. *Left*) Model spectra of a star-forming galaxy at $z = 9$ ($\log[M_*/M_\odot] = 9.9$; $E(B-V)=0.2$; $SFR=90 M_\odot \text{ yr}^{-1}$), compared to a number of potentially contaminating objects, including a passive and dusty star-forming galaxy, both at $z = 2.2$ ($\log[M_*/M_\odot] = 9.3$, to roughly match the flux of the high-redshift model in the WFC3 bands), and example M, L and T brown dwarfs (Burgasser 2014). The background gray shading denotes the filters used common in all fields (the shallower F140W is not shown), and the gray bars show the 5σ limiting magnitudes for the CANDELS Wide (top) and deep (bottom) surveys. All objects look roughly similar in the WFC3/IR bands, but diverge rapidly by *Spitzer*/IRAC wavelengths. This highlights the utility of using these longer-wavelength data when selecting high-redshift galaxies. *Right*) Stamp images ($3''$ in *HST*, $10''$ in IRAC) of three example galaxies in the *HST* and IRAC filters (the optical is a stack of F606W+F814W). In *HST* only, all objects show no optical flux, and a red $J-H$ color, consistent with a $z > 8$ solution, indicated by the blue $P(z)$ curve in the right panel. The inclusion of IRAC data either solidifies the high-redshift solution (top and bottom rows), or shows the low-redshift solution to be more likely (middle row). The inclusion of IRAC imaging, even with a faint or no detection, can thus significantly increase the fidelity of photometric redshift measurements.

molecular absorption bands near the peak of their thermal emission.

In the right panel of Figure 4, we illustrate the utility of this IRAC imaging using three examples. All three rows show objects which have a significant probability of being at $z > 8$ when measuring photometric redshifts with only *HST* imaging. When adding IRAC imaging to the first object, the photometric-redshift solution peaks up tightly at $z \sim 9$, as the IRAC flux is comparable to the *HST* flux (e.g., a roughly flat SED), and the IRAC $[3.6]-[4.5]$ color is red, indicative of either a Balmer break, or, more likely, strong [O III] emission in the redder band. The third row has a similar result, though in this case the IRAC detection is very low signal-to-noise, illustrating that even the lack of an IRAC detection is highly useful. The middle row shows an object which is now more likely at $z \sim 2$, due to the very bright IRAC fluxes. Importantly, this source did have a $z \sim 2$ potential solution even with *HST*-only data, but the inclusion of IRAC makes this the dominant redshift solution.

In this work, we are thus motivated to use photometric redshifts as our primary sample selection tool (as opposed to first applying color-cuts, and then a photometric redshift analysis) to make full use of the available *Spitzer*/IRAC data in these fields. We note that these fields also contain an abundance of ground-based imaging. We first select our galaxy sample using space-based

data alone, but in §4 we vet this sample using the available ground-based imaging.

3.1. Photometric Redshift Measurements

We use photometric redshifts to select our galaxy sample, following techniques similar to our previous work (e.g. Finkelstein et al. 2015c). While photometric redshift calculations at these high-redshifts primarily key off of the Lyman break, and are in principle similar to color-color selection (e.g., Steidel & Hamilton 1993; Giavalisco et al. 2004b; Bouwens et al. 2015b; Bridge et al. 2019), this method has the advantage that it simultaneously uses all available photometric information. This simplifies the selection process and results in a more inclusive sample, including objects lying just outside color-selection windows (e.g., McLure et al. 2009; Finkelstein et al. 2010, 2015c; Bowler et al. 2012, 2014, 2015; Atek et al. 2015; Livermore et al. 2017; Bouwens et al. 2019). Additionally, these codes typically provide a redshift probability distribution function (PDF), which we will denote $\mathcal{P}(z)$, which provides more information on the redshift than the binary in/out of color-selection.

We use the photometric-redshift (photo- z) code EAZY (Brammer et al. 2008) to perform our redshift estimation, assuming a flat luminosity prior as the epoch we are probing has not been well characterized. Use uses all available photometry and compares it to a series of templates, allowing non-linear combinations of any number

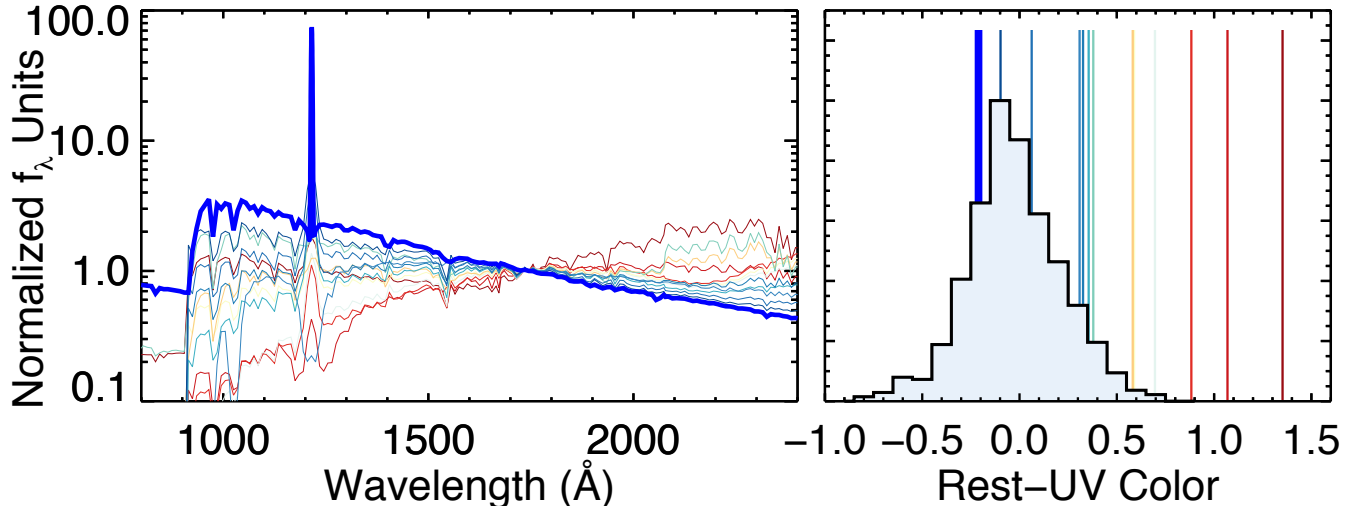


Figure 5. *Left*) The rest-frame ultraviolet region of the EAZY template set used in our analysis to measure photometric redshifts. The thin lines show the latest standard template set (tweak_fsp_QSF_v12.v3), while the thick line shows an additional template we added from the low-mass, star-forming galaxy BX418 (Erb et al. 2010), which is very blue, and has high nebular-line EWs. All templates are normalized to their flux density at 1750 Å. *Right*) The histogram shows the distribution of $J-H$ colors for $z=6-8$ galaxies from the catalog of Finkelstein et al. (2015c). The solid lines show the rest-UV color of the templates in the left panel, using the ratio of the 2000/1500 Å flux to calculate the color, which is approximately the rest-frame wavelength probed by $J-H$ at $z \sim 7$. The bluest EAZY template only reaches a rest-UV color of -0.1 , while roughly half of the comparison high-redshift sample has bluer colors (and we expect $z > 8$ galaxies to be at least as blue). The BX418 model extends our template set another ~ 0.1 mag bluer in color. This full template set can reproduce the colors of $\sim 85\%$ of the Finkelstein et al. (2015c) $z=6-8$ high-redshift sample.

of provided templates. We make use of the latest EAZY template set, known as “tweak_fsp_QSF_v12.v3”, which is based on the Flexible Stellar Population Synthesis code (FSPS, Conroy & Gunn 2010), including a more representative set of templates (inclusive of emission lines) than the original EAZY v1.0 templates. This template set has further been corrected (or “tweaked”) for systematic offsets observed between data and the models².

Figure 5 shows the full slate of EAZY templates from this set. In the right-hand panel, we compare the rest-UV color of these templates (measured from the ratio of the 1500-to-2000 Å flux density in f_ν units) to the distribution of similar rest-wavelength colors from $z > 6$ galaxies in the CANDELS fields (these are the $J-H$ colors for all galaxies with $z_{phot} > 6$ from Finkelstein et al. 2015c). Most of the standard templates are much redder than typical high-redshift galaxies, and the bluest template is only as blue as the median high-redshift galaxy. For this reason, similar to our previous work we add as an additional template the $z=2.3$ galaxy BX418, which is young, low-mass and blue (Erb et al. 2010). This galaxy’s color is 0.12 mag bluer than the bluest standard template, and has a color bluer than 85% of

the known high-redshift galaxies. We add two versions of this template; one with the observed Ly α emission as shown in Figure 5, and one where we remove the Ly α emission, to account for blue galaxies whose Ly α has been absorbed from a potentially neutral IGM (e.g., Miralda-Escudé & Rees 1998; Malhotra & Rhoads 2006; Dijkstra 2014).

For each field, we perform two runs of EAZY; one with all photometric bands, and a second excluding the IRAC bands. This second run is included to allow true high-redshift galaxies which have unreliable IRAC photometry due to poor deblending to still potentially be selected based on their *HST* photometry only (see also §3.3.4).

3.2. Sample Selection Criteria

We use the results from EAZY in tandem with our photometric catalogs to select our sample of $z \sim 9-11$ galaxy candidates. Following our previous work (Finkelstein et al. 2015c), we elect to use information present in the $\mathcal{P}(z)$ to select our sample, rather than using the best-fitting photometric redshift alone. Our sample selection criteria are (where \wedge and \vee represent the logical and and or operators, respectively):

$$[1] S/N_H > 7 \vee S/N_J > 7$$

This requires a significant detection in either the J_{125} or H_{160} bands in a $0.4''$ diameter photomet-

² Further information on EAZY and these templates can be found at <https://github.com/gbrammer/eazy-photoz/>

ric aperture. We allow objects satisfying this significance level in either band to make our sample, as blue galaxies at the lower edge of our desired redshift range ($z \sim 8.5$) may have a higher significance in the J_{125} -band. We also note that our requirement of a 7σ detection is more conservative than the typically used 5σ . However, with the limited photometric information available, we wanted to ensure our sample was free from spurious sources. Finally, we use a $0.4''$ diameter aperture for all sources to consistently measure the significance of the peak of an object's emission, as the occasionally larger Kron aperture would result in a lower S/N.

- [2] RMS value in V_{606} , I_{814} , J_{125} , $H_{160} < 10^3$ [counts/sec]

This requires photometric coverage in all key *HST* filters, as in our reduced mosaics pixels with no exposure time have a flag value of $RMS = 10^4$.

In the GOODS fields, we add the B -band to this requirement (and use i_{775} rather than I_{814} , as it covers more area).

- [3] $(S/N_V < 2 \vee S/N_I < 2) \wedge \min(S/N_V, S/N_I) < 1.4$

This allows a maximum 2σ significance detection in either of the V_{606} and I_{814} optical bands, and also requires $< 1.4\sigma$ significance in the weaker of the two bands.

In the GOODS fields, we also require less than 2σ significance detections in i_{775} , z_{850} and Y_{105} , and we add B_{435} , i_{775} and z_{850} to the $< 1.4\sigma$ significance criterion.

In principle these requirements are superfluous given the photometric redshift requirements below, but we employ them to keep our sample selection conservative.

- [4] $\int \mathcal{P}(z > 8) > 0.6 \wedge \Delta\chi^2 = \chi_{low-z}^2 - \chi_{high-z}^2 > 3.5$

The first criterion requires $> 60\%$ of probability to reside at $z > 8$ (integrated out to the maximum redshift considered by EAZY of 15), allowing $< 40\%$ to be present in a low-redshift solution. The second criterion requires the goodness-of-fit of any secondary low-redshift solution to be significantly worse than that of the high-redshift solution; we chose a threshold just less than a 95% confidence requirement

(which would be $\Delta\chi^2 > 4$) to ensure we explore objects which fall just below this threshold. We note that only one object has $3.5 < \Delta\chi^2 < 4$ (EGS_z910_26890, with $\Delta\chi^2 = 3.51$), and that this increases to 12.9 with the inclusion of additional *HST* imaging (§4.3).

- [5] $\chi_{EAZY}^2 < 60$

This requires EAZY to have found a reasonably good fit, rejecting objects where even the best-fitting solution is not a good match to the observed photometry.

- [6] $\int \mathcal{P}(z \sim 9 \vee 10 \vee 11) > \int \mathcal{P}(z \sim 5 \vee 6 \vee 7 \vee 8)$

This requires the integral of $\mathcal{P}(z)$ in $\Delta z = 1$ bins centered at $z = 9, 10$ or 11 to be greater than those centered at $z = 5, 6, 7$ or 8 .

- [7] $r_h > 1.1$ pixels \vee Stellarity < 0.9

These criteria are designed to remove potentially lingering image artifacts such as hot pixels or cosmic rays. As objects in our redshift range of interest may be single H_{160} -band detections, these artifacts can satisfy the sample selection. We thus require a half-light radius of greater than 1.1 pixels (following the analysis done in Rojas-Ruiz et al. 2020), or a Source Extractor stellerity value of < 0.9 .

- [8] $22 < H_{160}$ -band magnitude < 26.6

The brighter cut corresponds to $M_{UV} \sim -25$ at $z = 9$, and thus is much brighter than any source we expect to find in our sample, but imposing this cut removes interlopers such as bright stars which can contaminate the sample. The fainter cut is approximately the 7σ limit for our shallowest field (Table 2), reflecting our goal of studying the brighter galaxy population in this epoch. True candidates certainly exist in these data fainter than this limit, but as our goal here is to study bright galaxies, imposing this limit reduces the number of faint contaminants needing to be analyzed.

Together, these criteria select sources which are photometrically robust, modestly bright, have high photometric redshift likelihoods of residing at $z > 8.5$, and rely minimally on human intervention, limiting potential biases in our final sample.

3.3. Contaminant Rejection

Our initial sample as described in the previous subsection consists of 140 sources: 19 in EGS, 20 in COSMOS, 67 in UDS, 28 in GOODS-N and 6 in GOODS-S. This is significantly larger than any reasonable expectation of the number density of such distant galaxies, thus we expect this initial sample to be dominated by contaminant objects. In this subsection, we detail the several types of contaminants we screen for and remove. During this screening we rely on automated quantitative cuts whenever possible. We implement these steps in this order to remove the most obvious contaminants (e.g., persistence, diffraction spikes) first, prior to more subjective removal. We provide images in the appendix for any objects removed based on a subjective visual inspection.

3.3.1. Persistence

Persistence from previously observed bright targets could masquerade as high-redshift galaxies. This problem is exacerbated as CANDELS observed the H_{160} -band before the J_{125} -band, and, as persistence fades with time, the resulting photometric color could mimic a J_{125} -band dropout. For each of our initial candidates, we searched the MAST archive for observations done in the 24 hours previous to each of the individual images (FLTs) which went into the CANDELS mosaics, recording the maximum value in a 10×10 pixel box around the position of our object. We did this for both the CANDELS J_{125} and H_{160} images, as well as the 3D-HST JH_{140} imaging. The latter were taken at a different time, and so give an independent measure of whether a source which is detected in multiple bands is a real source, or persistence.

If all of the images which went into the H_{160} mosaic had a fluence $< 100,000 e^-$ at the same position as a given candidate measured in an image from the preceding 24 hours, we consider the object to be not significantly affected by persistence. This threshold was devised empirically, to ensure all potentially spurious sources were removed. For objects with a H_{160} -band fluence $> 100,000 e^-$, if they have significant detections in the J_{125} and/or JH_{140} bands *and* those bands have a measured fluence $< 100,000 e^-$, then we consider them to be real objects and keep them in our sample. However, in the more common case, objects are undetected in JH_{140} , and have a fluence $> 100,000 e^-$ in both J_{125} and H_{160} ; these objects are removed from the sample.

This process removed 53 galaxies from our sample, 42 of which were from the heavily affected UDS field as the previous observations in that resulted in a large number of persistence artifacts of varying brightness levels. Our sample at this stage thus consisted of 87 galaxies.

3.3.2. HST Visual Inspection

We performed a detailed visual inspection of every object in this initial sample to remove image artifacts, examining each source in each band to determine whether a source is a diffraction spike, an oversplit region of a nearby (usually) bright galaxy, near an image edge, or any other obvious image artifact. Through this process, we identified 21 objects as being diffraction spikes, 11 as being oversplit regions of nearby galaxies, and 13 objects as other artifacts. As this process is unavoidably subjective, we include Figure 24 in the Appendix showing H_{160} -band image cutouts of objects removed in this process. Our sample size following this step was 42 galaxies.

3.3.3. Local Noise Measurement

While our noise calculation takes into account the difference in rms map value at the position of our source compared to the median of the image, it is still possible that the region surrounding an object of interest has higher noise properties, rendering an object which formally passes our S/N cuts in truth less significant. To explore if this affected any of our objects, we calculated the local noise in the H_{160} -band in a region around each of our sources. We did this by randomly placing $0.4''$ diameter apertures over a region 450 pixels wide around a given source of interest. The random positions were constrained to be non-overlapping and also to avoid real objects (using the Source Extractor segmentation map). The local noise was then taken as a sigma-clipped standard deviation of the measured values. We used this noise in tandem with the measured $0.4''$ diameter flux values of the source to create a measure of the local signal to noise. We removed any object in our catalog which had a local S/N < 5.0 in the H_{160} -band. This resulted in the removal of two objects total, both in the GOODS-S field.

3.3.4. Poor IRAC Deblending

Inspection of the remaining 40 galaxies showed that several sources were crowded in the IRAC bands. While our use of the TPHOT photometry deblending software was done to mitigate inaccurate photometry due to crowding, these methods can fail when bright sources are sufficiently close. For this reason, we did another round of visual inspection on the remaining sources, exploring whether the TPHOT residuals in the vicinity of our objects of interest were sufficiently small. For any source where the residuals were large, we then considered the results of our EAZY run without the IRAC photometry. If a given source satisfied our sample selection criteria when the IRAC photometry was not used with EAZY,

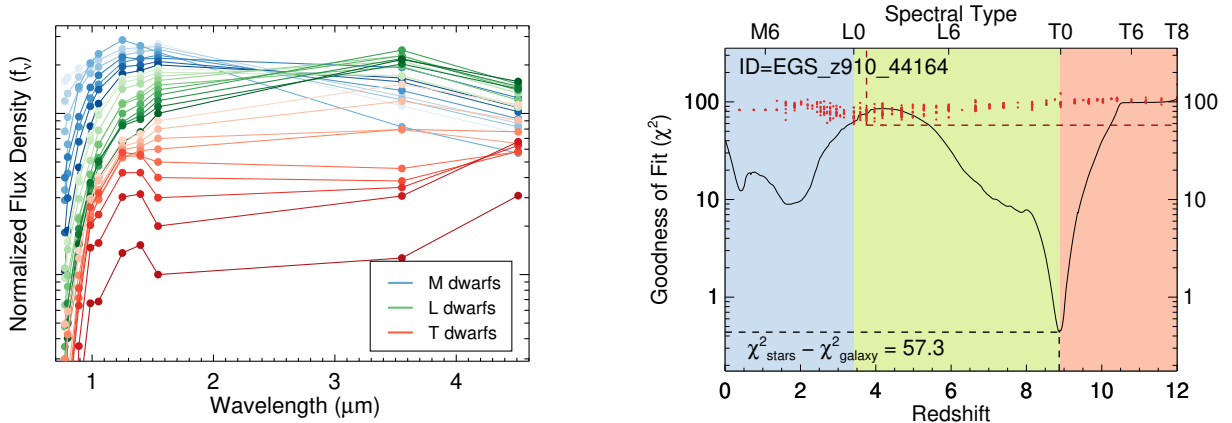


Figure 6. *Left*) The stellar SEDs derived for MLT dwarf stars. The near-IR photometry was obtained by integrating the SpeX prism library spectra through the HST bandpasses, while the IRAC photometry was obtained by matching SpeX stars to IRAC-observed stars from Patten et al. (2006) at the same spectral type, normalizing by 2MASS K -band magnitude. The full set of stellar SEDs we derived numbered 570; we show here a subset of 27 spanning the full spectral range used, of M3.5 – T8. *Right*) The results of the stellar template fitting for one candidate galaxy in the EGS field. Each red dot denotes the χ^2 value for a given stellar template when compared to our observed photometry for this galaxy, while the black line shows the χ^2 for the galaxy templates from EAZY. The blue, green and red shaded regions correspond to the top-axis M, L and T spectral types, respectively. The dashed lines show the best-fitting values, corresponding to $z = 8.9$ for the best-fitting galaxy template, and a spectral type of L1 for the best-fitting stellar template. As the galaxy solution is a significantly better fit ($\Delta\chi^2 \gg 4$), we conclude this source is not a stellar contaminant. We find similar results ($\Delta\chi^2 > 4$) for all 14 candidates in the initial galaxy sample.

then it remained in our sample, else it was removed. This process removed 26 objects from our sample, all of which are shown in Figure 25 in the Appendix. We note that ID 44740 in GOODS-S formally did satisfy the selection criteria without IRAC. However, upon inspection of the IRAC image, it was clear that significant source flux is coming from this object, leading to a very red SED. We thus concluded that it is not likely to be a high-redshift galaxy, removed it at this stage, and also show it in Figure 25. Following this step, our sample consisted of 14 galaxies: 7, 3, 3, 1 and 0 in the EGS, COSMOS, UDS, GOODS-N and GOODS-S fields, respectively.

3.3.5. Stellar Contamination Screening

As shown in Figure 4, low-mass stars and brown dwarfs can have colors similar to very high redshift galaxies, and models of the Milky Way stellar distribution predict that our observed fields may have a few such objects at similar magnitudes as our target galaxies, though the majority will have $J_{125} < 25$ as they are primarily in the Galactic disk (Ryan & Reid 2016). To explore whether any of our candidates are likely to be a stellar contaminant, we calculate the goodness-of-fit (χ^2) of each object compared to synthetic photometry created from a suite of stellar spectra, considering an object for removal if it had $\chi_{Stellar}^2 < \chi_{EAZY}^2$, where the latter is the value from the best-fitting EAZY galaxy template.

We use the IRTF SpeX stellar library (Burgasser 2014), which has empirical spectra for 165 M-dwarfs, 272 L-dwarfs, and 133 T-dwarfs, spanning 0.6–2.5 μm in wavelength, and the full temperature range for each spectral type. We integrated each of these 570 spectra through the HST filter set used in our study to derive bandpass-averaged fluxes. However, as these spectra only extend to 2.5 μm , we cannot use them directly to derive the photometry in the IRAC bands. To do this, we make use of the tabulated 2MASS and IRAC photometry for 84 MLT stellar dwarfs (spanning M3.5 – T8) from Patten et al. (2006). For each of the SpeX stars, we find all stars in the Patten et al. (2006) sample with a similar spectral type ($\Delta\text{type} < 1$). In two cases, there were not at least three stars within a unit spectral type; in these cases we extended the search to $\Delta\text{type} < 3$, which yielded three stars in both cases.

We estimate the IRAC photometry for the SpeX stars from these stars of matched spectral type as

$$[3.6]_{\text{SpeX}} = K_{\text{SpeX}} - \langle K_{\text{Patten}} - [3.6]_{\text{Patten}} \rangle \quad (2)$$

$$[4.5]_{\text{SpeX}} = [3.6]_{\text{SpeX}} - \langle [3.6]_{\text{Patten}} - [4.5]_{\text{Patten}} \rangle \quad (3)$$

where the K -band magnitudes come from 2MASS, and all magnitudes are converted from Vega to AB ($m_{AB} = m_{Vega} + 0.91, 1.39, 1.85, 2.79$ and 3.26 for $J, H, K, [3.6]$ and $[4.5]$, respectively). Combining these IRAC fluxes with our calculated HST-filter fluxes provides us with

photometry for these 570 MLT dwarfs in the same filter set as our observed galaxy candidates.

The left panel of Figure 6 shows the range of stellar SEDs we derived from this process, highlighting that these stellar objects have a range of SED shapes and features. To explore whether these objects could be contaminating our galaxy sample, we calculated the goodness-of-fit χ^2 statistic between our candidate galaxies and each of these 570 stellar templates, where the stars were normalized to the galaxy fluxes using a weighted mean of the flux ratios in all bands. We give an example of this process in the right panel of Figure 6, showing the EAZY $\chi^2(z)$ alongside the stellar χ^2 as a function of spectral type. For this object, which has a best-fitting $z_{phot}=8.9$ with $\chi_{EAZY}^2=0.4$, the best-fitting stellar model has a spectral type of L1, with $\chi_{stars}^2=57.7$, with $\Delta\chi^2 = \chi_{stars}^2 - \chi_{EAZY}^2 = 57.3$. We consider an object to be a potential stellar contaminant if $\Delta\chi^2 < 4$, such that the stellar SED cannot be ruled out at $>95\%$ confidence. We find that none of our 14 candidate galaxies have $\Delta\chi^2 < 4$ (only EGS_z910_26890 has $\Delta\chi^2 < 15$, with $\Delta\chi^2 < 5.3$). We thus conclude that none of the 14 objects in this initial sample are likely to be stellar in nature.

3.3.6. Active Galactic Nuclei

Although unlikely to be found in our relatively small area at such extreme redshifts, we still consider whether our sources could be dominated by emission from an accreting supermassive black hole. The easiest way to diagnose the presence of a dominant active galactic nucleus (AGN) is via X-ray emission. We searched the published X-ray catalogs in these fields (Kocevski et al. 2018; Xue et al. 2016; Nandra et al. 2015; Elvis et al. 2009) to see if there was a detection coincident with our candidates, finding no such matches (the closest X-ray source in the catalogs was at 6–30'' from our candidates). This unsurprisingly rules out bright unobscured AGNs as the power source for our objects. This does not however rule out fainter AGN contribution to our source luminosities, which should be easily discernable via emission-line ratios *JWST* spectroscopy.

3.4. Summary of Initial *HST*+*Spitzer*-Selected Sample

Through the processes described above, we have selected a sample of 14 candidate galaxies at $z \sim 8.5-11$ across all CANDELS fields at $H < 26.6$: 7, 3, 3, 1 and 0 in the EGS, COSMOS, UDS, GOODS-N and GOODS-S fields, respectively. We list properties of this sample in Table 3, and summarize these properties in Figure 7. By construction, this sample is well constrained to have $z > 8$, with 11/14 objects having $\int \mathcal{P}(z > 8) \geq 0.85$, and best-fitting photometric redshifts from $8.8 < z <$

10.4. Also by construction these sources are bright, with one exceptionally bright source at $H = 24.5$, which we consider further below. Image cutouts of these candidates are shown in Figure 8, highlighting the optical non-detection, and robust F160W detection.

3.5. Comparison to Color-Color Selection Methods

We show the colors spanned by these 14 candidates in Figure 9, color-coded by their field. We compare the color selection originally employed by Bouwens et al. (2016b), of $J - H > 0.5$ and $H - [3.6] < 1.4$. We find that our candidates all lie either in this selection box, or within 1σ of a given color. We note that had we employed this color selection to our sample in addition to our photometric redshift selection, we would have excluded six galaxies, a significant fraction of our total sample size. The majority of those candidates outside the box have slightly bluer $J - H$ colors than the Bouwens et al. (2016b) threshold, which likely indicates that they reside in the low side of our redshift bin. Indeed, of the five candidates, all in the EGS field, with $J - H < 0.5$, four have $z_{best} < 9.0$, indicating a potential overdensity of sources at $z \sim 8.7$ in this field, which we discuss further in §7.

3.6. Spectroscopic Confirmation

Three of our 14 candidates are already spectroscopically confirmed to lie at $z > 8.5$. Zitrin et al. (2015) measured Ly α emission at $z = 8.68$ from the second brightest source in our initial sample, EGS_z910_6811 at $H = 25.2$ (known as EGSY8p7 in Zitrin et al. 2015), consistent with our measured photometric redshift of $8.84_{-0.18}^{+0.07}$. Mainali et al. (2018) also present a 4.6σ detection of N V $\lambda 1243$ for this source, indicating it may be powered in part by an active galactic nucleus (AGN), perhaps explaining its high rest-UV luminosity. Our source EGS_z910_44164, the next brightest source in the EGS field with $H = 25.4$, has a 7σ detection of Ly α at $z = 8.665 \pm 0.001$, also from MOSFIRE (Larson et al. 2021). Our source GOODS_N_z910_35589 with $H_{160}=25.8$ has a measured redshift of $z = 11.09_{-0.12}^{+0.08}$ from low-resolution *HST* grism spectroscopy (Oesch et al. 2016, also known as GNz11), and recently C III] was detected from this source at $z = 10.957$ (Jiang et al. 2021), with the C III] strength also implying a potential AGN contribution. This redshift is $\sim 2\sigma$ higher than our photometric redshift of $10.41_{-0.07}^{+0.30}$, though our measurement is consistent with the photometric redshift of $z = 10.2$ from Oesch et al. (2016). Larson et al. (2021) has spectroscopically observed many of the remaining 11 candidate galaxies with no significant line detections, thus *JWST* (or perhaps ALMA) will be required to spectroscopically confirm these candidates.

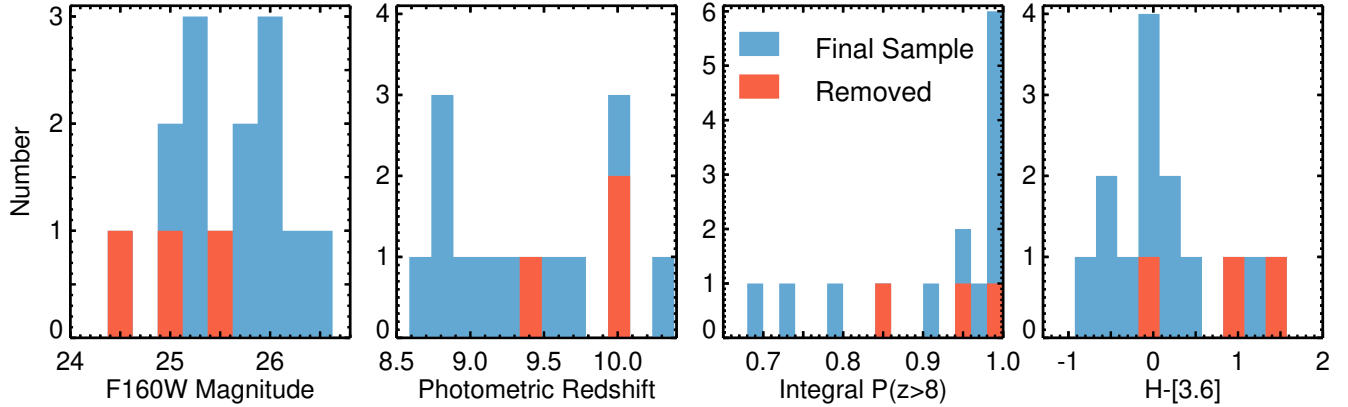


Figure 7. The distribution of properties from our *HST*+*Spitzer*-selected sample. Objects which are removed via further analysis in §4 are shown in red, while those which remain in our final sample are shown in blue. From left-to-right, the plots are: the total H_{160} -band apparent magnitude, the best-fitting photometric redshift, $\int \mathcal{O}(z > 8)$, and the H_{160} -[3.6] color.

Table 3. Initial Candidate Bright ($H < 26.6$) Galaxies at $z > 8.5$

| ID | RA | Dec | F160W Mag | $\int \mathcal{O}(z > 8)$ | z_{best} | Half-light radius |
|--------------------------------|------------|-----------|------------------|---------------------------|-------------------------|-------------------|
| | J2000 | J2000 | | | | |
| EGS_z910_6811 | 215.035385 | 52.890666 | 25.16 ± 0.05 | 1.00 | $8.84^{+0.12}_{-0.25}$ | 0.138 |
| EGS_z910_44164 | 215.218737 | 53.069859 | 25.41 ± 0.07 | 0.96 | $8.87^{+0.17}_{-0.32}$ | 0.174 |
| EGS_z910_68560 | 214.809021 | 52.838405 | 25.76 ± 0.08 | 1.00 | $9.16^{+0.17}_{-0.36}$ | 0.111 |
| EGS_z910_20381 | 215.188415 | 53.033644 | 26.05 ± 0.10 | 0.74 | $8.83^{+0.15}_{-1.20}$ | 0.125 |
| EGS_z910_26890 | 214.967536 | 52.932966 | 26.09 ± 0.07 | 0.80 | $8.99^{+0.19}_{-6.84}$ | 0.099 |
| EGS_z910_26816 | 215.097775 | 53.025095 | 26.11 ± 0.10 | 0.92 | $9.40^{+0.24}_{-0.55}$ | 0.102 |
| EGS_z910_40898 | 214.882993 | 52.840414 | 26.50 ± 0.11 | 0.69 | $8.76^{+0.23}_{-1.33}$ | 0.103 |
| COSMOS_z910_14822 [†] | 150.145769 | 2.233625 | 24.51 ± 0.04 | 1.00 | $9.44^{+0.04}_{-0.34}$ | 0.140 |
| COSMOS_z910_20646 | 150.081846 | 2.262751 | 25.42 ± 0.08 | 1.00 | $9.82^{+0.19}_{-0.59}$ | 0.108 |
| COSMOS_z910_47074 | 150.126386 | 2.383777 | 26.32 ± 0.10 | 0.99 | $9.59^{+0.12}_{-0.60}$ | 0.103 |
| UDS_z910_731 [†] | 34.317089 | -5.275935 | 25.02 ± 0.12 | 0.85 | $10.10^{+1.72}_{-0.65}$ | 0.252 |
| UDS_z910_18697 | 34.255636 | -5.166606 | 25.32 ± 0.09 | 1.00 | $10.04^{+0.38}_{-0.22}$ | 0.174 |
| UDS_z910_7815 [†] | 34.392823 | -5.259911 | 25.82 ± 0.15 | 0.95 | $10.03^{+0.98}_{-0.55}$ | 0.174 |
| GOODSN_z910_35589 | 189.106061 | 62.242040 | 25.82 ± 0.05 | 1.00 | $10.41^{+0.30}_{-0.07}$ | 0.121 |

NOTE—The full list of candidate $z > 8.5$ galaxies selected with *HST*+*Spitzer* data. [†] These three objects were later removed from the sample based on ground-based and additional *HST* photometry, which implied they likely reside at $z < 8$. The positions have been corrected from the original CANDELS astrometry to PAN-STARRS DR1, which was tied to *Gaia* DR1. The reported half-light radii are measured by Source Extractor on the F160W image.

4. VETTING THE SAMPLE WITH ADDITIONAL IMAGING

4.1. The Brightest Source: COSMOS_z910_14822

Of our 14 candidates, only COSMOS_z910_14822 has $H < 25.0$, with $H = 24.51 \pm 0.04$ and $z_{best} = 9.44^{+0.04}_{-0.34}$. In Figure 10, we show our initial photometric redshift PDF for this source. Our photometric redshift with our default photometry, either with (in blue) our without (in

purple) the deblended TPHOT IRAC photometry, overwhelmingly prefers a $z > 9$ solution, although a small probability exists of a $z \sim 2$ solution.

However, as shown in Figure 8, this source is the only candidate in our sample which has a bright neighbor visible within the 3'' *HST* image cutout. While the IRAC residual image shows that this neighbor seems to be well subtracted, here we consider how reliant the photometric redshift is on the IRAC photometry deblend-

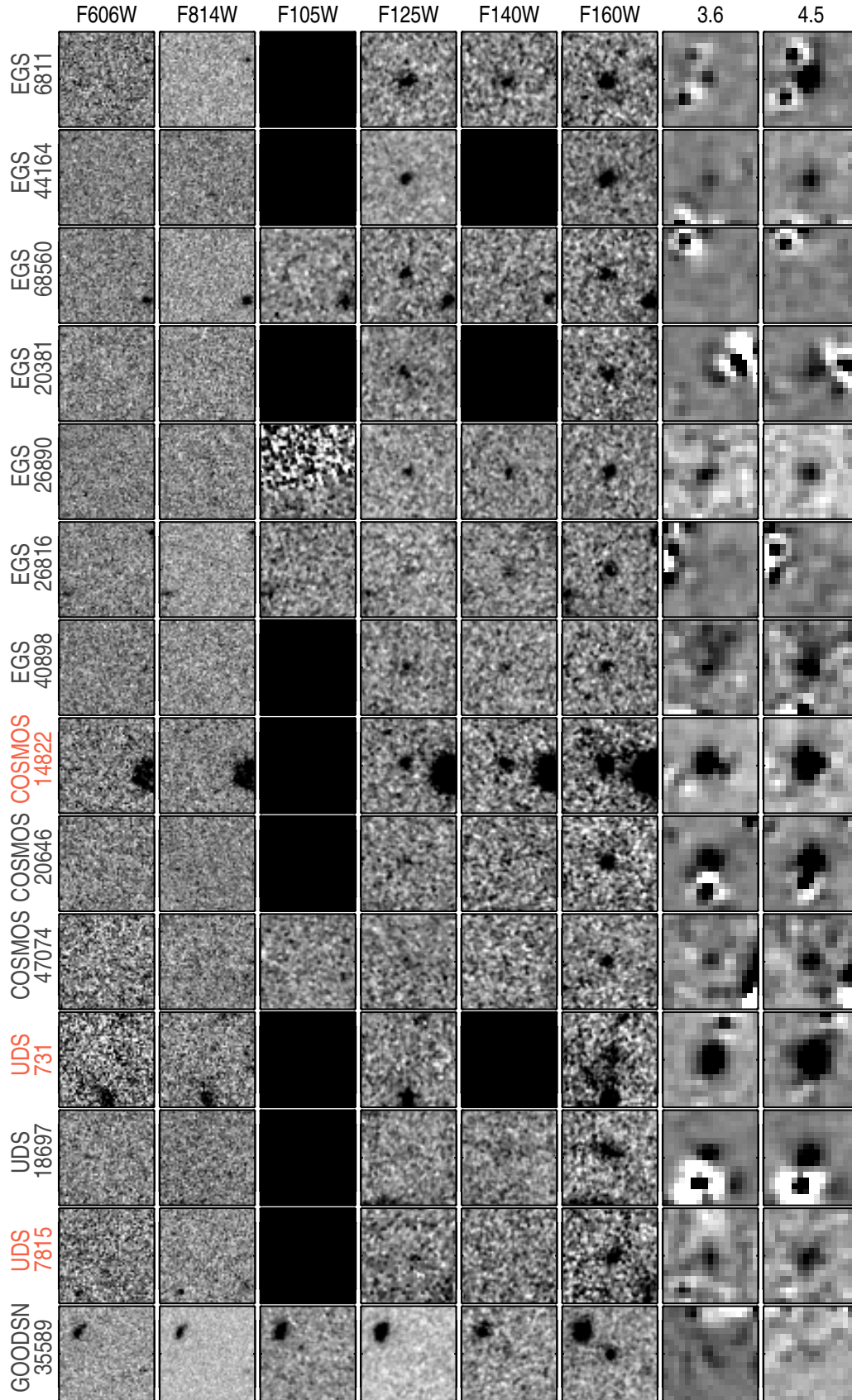


Figure 8. Cutout images of our *HST*+*Spitzer*-selected sample, centered on the candidates. The IRAC cutouts have the nearby neighbors subtracted with TPHOT. The *HST* cutouts are $3'' \times 3''$, while the IRAC cutouts are $10'' \times 10''$. The three sources removed during our vetting process have their labels in red.

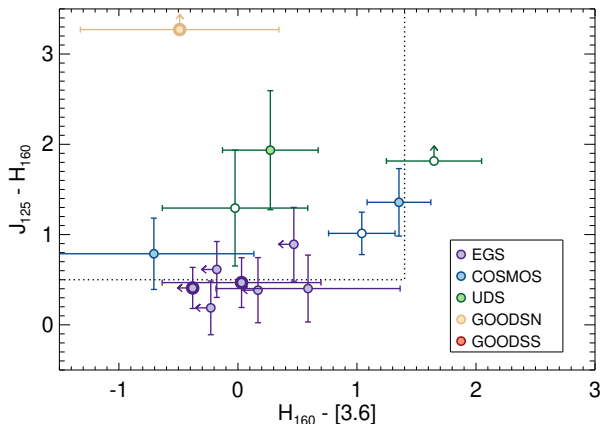


Figure 9. A color-color diagram showing the colors of our *HST*+*Spitzer*-selected sample. Objects which are removed via further analysis in the next section are shown as white-filled circles. Objects where a given band is detected at $<1.5\sigma$ significance are replaced by 1.5σ limits. The dotted lines show the color-selection criteria employed by Bouwens et al. (2016b). This color selection would have excluded six galaxies from this initial sample, five which have slightly bluer $J - H$ colors, indicating $z \sim 8.5-9$. The two sources with known spectroscopic confirmations are denoted by thicker circles.

ing method. With our original TPHOT photometry, we measure $m_{3.6} = 23.47 \pm 0.08$, and $m_{4.5} = 22.98 \pm 0.05$, giving $[3.6] - [4.5] = 0.49$. This red IRAC color is consistent with a high-redshift solution, where the red color is caused by either strong rest-optical emission lines, or (perhaps less likely) a strong 4000 \AA break.

To explore the dependence of the preferred redshift on the IRAC photometry, we calculate an independent set of deblended photometry using the methodology of Finkelstein et al. (2015a). This uses GALFIT (Peng et al. 2002) to model and subtract all neighboring sources, and to measure the photometry of our source of interest. With this method we measure $m_{3.6} = 23.22 \pm 0.11$ and $m_{4.5} = 23.28 \pm 0.14$, giving $[3.6] - [4.5] = -0.06$. A flat color is more consistent with spanning the peak of the stellar SED at $\lambda_{rest} \sim 1.6\mu\text{m}$, thus when combining our *HST* photometry with the GALFIT-based IRAC photometry, the $z \sim 2$ solution is preferred. We also perform a run of EAZY including both the TPHOT and GALFIT IRAC constraints. As shown in Figure 10, this result tacks closer to the TPHOT-only result, though now a small $z \sim 2$ solution is present. However, given the uncertainty about the IRAC fluxes, the redshift of this source remains uncertain from space-based data alone.

To investigate this further, we explore whether any additional constraints can be gained from the abundant, although often shallower, ground-based photometry in this field. We make use of the opti-

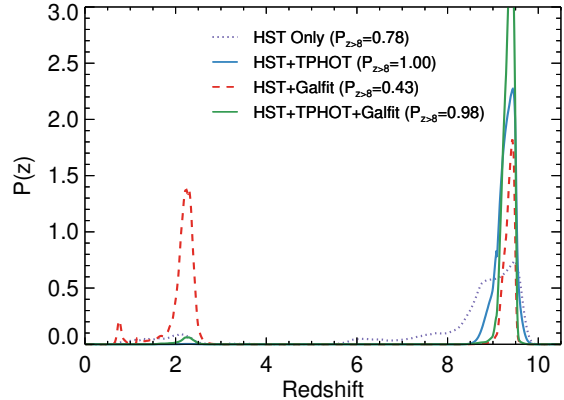


Figure 10. The photometric redshift probability distribution function (PDF) for the brightest source in our *HST*+IRAC sample, COSMOS_z910_14822. The blue solid line shows our fiducial photometric redshift, combining *HST* photometry with TPHOT-deblended *Spitzer*/IRAC photometry, which has 100% of the PDF at $z > 8$. However, due to a nearby bright neighbor, the IRAC photometry for this source is the most affected by deblending uncertainties. Fitting the *HST* photometry only (purple dotted) still prefers a high-redshift solution, although with less (78%) of its PDF at $z > 8$. Photometric redshift results with an independent deblending technique using GALFIT (red dashed) change the IRAC color enough to result in the low-redshift solution being nearly equally preferred. Combining the *HST* photometry with both IRAC measures (green solid) still prefers the high-redshift solution. Due to the uncertainty in the IRAC fluxes the nature of this source is thus uncertain with space-based data alone.

cal CFHT/MegaPrime u^* , g^* , r^* , i^* , z^* and Subaru/SuprimeCam B , g^+ , V , r^+ , z^+ photometry as published in the catalog of Nayyeri et al. (2017). As this catalog also includes *HST* photometry, we scale all measured fluxes by the ratio of our measured *HST* H_{160} -band to that measured by Nayyeri et al. (2017). For this source this ratio is nearly unity (0.992), lending credence to our aperture correction methods. We find no $>1.5\sigma$ significance detections in these optical bands. There are 1.49σ , 1.2σ and 1.28σ measurements in the CFHT z^* , Subaru V and Subaru z^+ bands, respectively. Cutout images of this source in these bands are shown in Figure 11. The Subaru V band shows a positive low-significance peak, but it is offset from the position of this source. While the CFHT z^* -band image shows nothing above the noise, the Subaru z^+ image shows some positive flux close to the position of this source, though it is weak, and visually appears consistent with our $\sim 1.3\sigma$ significance measurement. This is thus consistent with just being random noise, though it could also represent weak flux from a source at $z < 7$.

Table 4. COSMOS_z910.14822 Photometry

| ID | Flux (nJy) | Error (nJy) | S/N |
|----------------|------------|-------------|-------|
| CANDELS F606W | -5.2 | 13.8 | -0.38 |
| CANDELS F814W | -0.8 | 20.6 | -0.04 |
| CANDELS F125W | 223.4 | 23.5 | 9.52 |
| CANDELS F140W | 498.2 | 37.6 | 13.25 |
| CANDELS F160W | 568.0 | 22.0 | 25.84 |
| TPHOT 3.6 | 1481.2 | 104.0 | 14.24 |
| TPHOT 4.5 | 2326.8 | 104.9 | 22.18 |
| Galfit 3.6 | 1870.7 | 182.8 | 10.23 |
| Galfit 4.5 | 1770.1 | 230.7 | 7.67 |
| Cycle 26 F098M | 57.7 | 26.7 | 2.16 |
| CFHT u^* | 9.7 | 12.0 | 0.81 |
| CFHT g^* | -3.3 | 8.0 | -0.42 |
| CFHT r^* | 4.8 | 10.0 | 0.48 |
| CFHT i^* | 3.8 | 15.2 | 0.25 |
| CFHT z^* | 51.4 | 34.6 | 1.49 |
| Subaru B | 0.9 | 4.6 | 0.19 |
| Subaru g^+ | 13.0 | 15.9 | 0.82 |
| Subaru V | 14.6 | 12.2 | 1.20 |
| Subaru r^+ | 2.9 | 10.9 | 0.26 |
| Subaru z^+ | 57.5 | 45.0 | 1.28 |
| UVISTA Y | 141.1 | 46.5 | 3.04 |
| UVISTA J | 253.7 | 46.4 | 5.46 |
| UVISTA H | 519.0 | 53.2 | 9.75 |
| UVISTA K | 855.9 | 72.0 | 11.89 |
| zFourGE $J1$ | 32.8 | 48.9 | 0.67 |
| zFourGE $J2$ | 152.2 | 57.1 | 2.66 |
| zFourGE $J3$ | 293.0 | 58.0 | 5.05 |
| zFourGE H_s | 516.5 | 107.9 | 4.79 |
| zFourGE H_l | 618.4 | 112.4 | 5.50 |
| zFourGE K_s | 888.0 | 75.7 | 11.73 |

NOTE—Measured photometry for the brightest source in our sample, COSMOS_z910.14822. The optical ground-based photometry is taken from Nayyeri et al. (2017), while we measure photometry in all other filters (see §2.6 and §3.5.1 for details).

As this catalog does not include the latest UltraVISTA (McCracken et al. 2012) data release, nor the photometry from the ZFOURGE medium-band survey (Spitler et al. 2012; Straatman et al. 2014), we perform our own near-infrared ground-based photometry. We obtained the public UltraVISTA DR4 imaging in the Y , J , H and K bands (these images have a prefix of “UVISTA_X_19.11.18_allpaw_skysub_015_dr4_rc_v2”, where “X” denotes the filter name). For ZFOURGE, we

downloaded the latest public version of the data, which was v0.9.3, in the $J1$, $J2$, $J3$, H_s , H_l , and K_s bands. As these images are seeing limited, we do not expect our sources to be resolved. We thus devised a custom point-source photometry code, which executes the following steps.

1. Taking the position of the source of interest, cuts out a region of the image around this source $5'$ on a side, with the source of interest at the center. If this source is $<5'$ from the edge, it offsets the center of the cutout to keep it $5'$ in size.
2. Runs Source Extractor with this image as both the detection and measurement image to map the background, as well as create an initial catalog sufficient to identify stars in the image. As our source may not be detected in all bands, this does not provide our needed photometry. We visually inspect the Source Extractor results, to ensure the detection parameters are identifying all robust sources. We subtract this Source Extractor background map from the science image to create a background-subtracted image we use to perform our object photometry.
3. We use the initial Source Extractor catalog to identify stars by identifying their position in a plot of source magnitude versus spatial full-width at half-maximum (FWHM). We measure a histogram of the FWHM of sources brighter than $m < 20$ (with some variation allowed for the depth of the image), and take the default stellar (e.g. unresolved) FWHM to be the peak of this histogram. We then identify stars as those objects with $17 < m < 24$ and a FWHM of ± 0.5 pixels of this stellar FWHM. Finally, we select a fiducial sample of stars as the 6th–26th brightest objects in this list (skipping the first five to ensure we do not use any saturated objects, which should be omitted in any case due to the $m > 17$ limit). We then measure the curves-of-growth of these stars, to identify the median radius which encloses 70% of the total flux. We use this radius below to calculate aperture photometry, and then apply an aperture correction of $1/0.7$ to correct both the flux and noise to total (again assuming a point source).
4. We correct for any astrometric offset between a given image and the HST CANDELS images by matching sources between this Source Extractor catalog and our HST catalog for a given field, and calculating the median offset in right ascension and declination. We then apply these offsets to

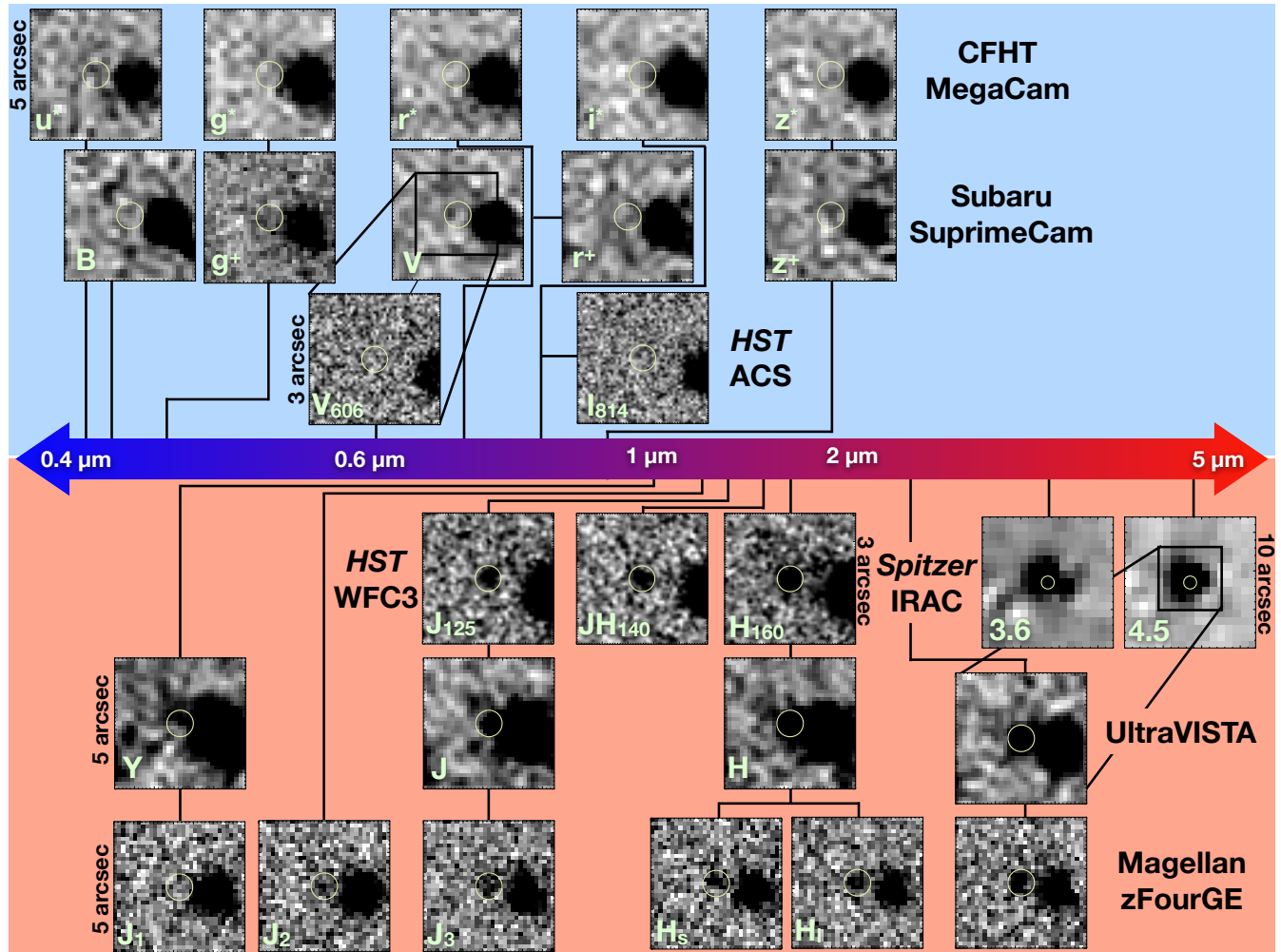


Figure 11. Cutout images of COSMOS_z910_14822 in all space and ground-based bands used in this study. Images are $3''$, $5''$ and $10''$ in size for *HST*, ground-based, and *Spitzer* images, respectively. Most bands are as expected for a $z > 9$ galaxy, except the UltraVISTA Y band. However, the significant emission in this band appears offset spatially to the North, thus the nature of the source remained unclear even after the inclusion of all ground-based data.

the position of our source of interest to calculate their corrected position in this ground-based image.

5. We measure the noise in our 70% flux-enclosed aperture using the same local noise routine discussed in §2.5.2 above (correcting to total).
6. We measure aperture photometry in this 70% flux-enclosed aperture at the corrected position of our source on the background-subtracted image using the IDL routine *aper* (correcting to total).

We used this routine to measure photometry at the position of COSMOS_z910_14822 on all ZFOURGE and UltraVISTA images. The values of our measured fluxes and flux uncertainties in all bands are given in Table 4, and cutout images of this source in all bands are shown in Figure 11. If this source was truly at $z > 8.5$, we would expect to see no flux blueward of $1.155 \mu\text{m}$, thus

we should see no flux in the VISTA Y-band and the ZFOURGE J1 filters, which have red edges of 1.066 and $1.104 \mu\text{m}$, respectively (ZFOURGE J2 has a red edge of $1.212 \mu\text{m}$, thus can contain flux for sources up to $z = 8.97$). While the ZFOURGE J1 band has no significant flux, there is a 3.0σ significance detection in the UltraVISTA Y-band. Investigating this image in Figure 11, the apparent significant flux is offset from the position of this source in the UltraVISTA JHK bands. It is thus unclear if the flux causing the Y-band “detection” is truly from this source, is noise, or is flux from the near neighbor, which is heavily blended in this seeing-limited data. Thus, even with the addition of ground-based data, the nature of this source is still uncertain.

We thus proposed for and were awarded two orbits of Cycle 26 mid-cycle *HST*/WFC3 F098M imaging (PID 15697; PI Finkelstein). This probes similar wavelengths as the UltraVISTA Y-band, but at a deeper depth and

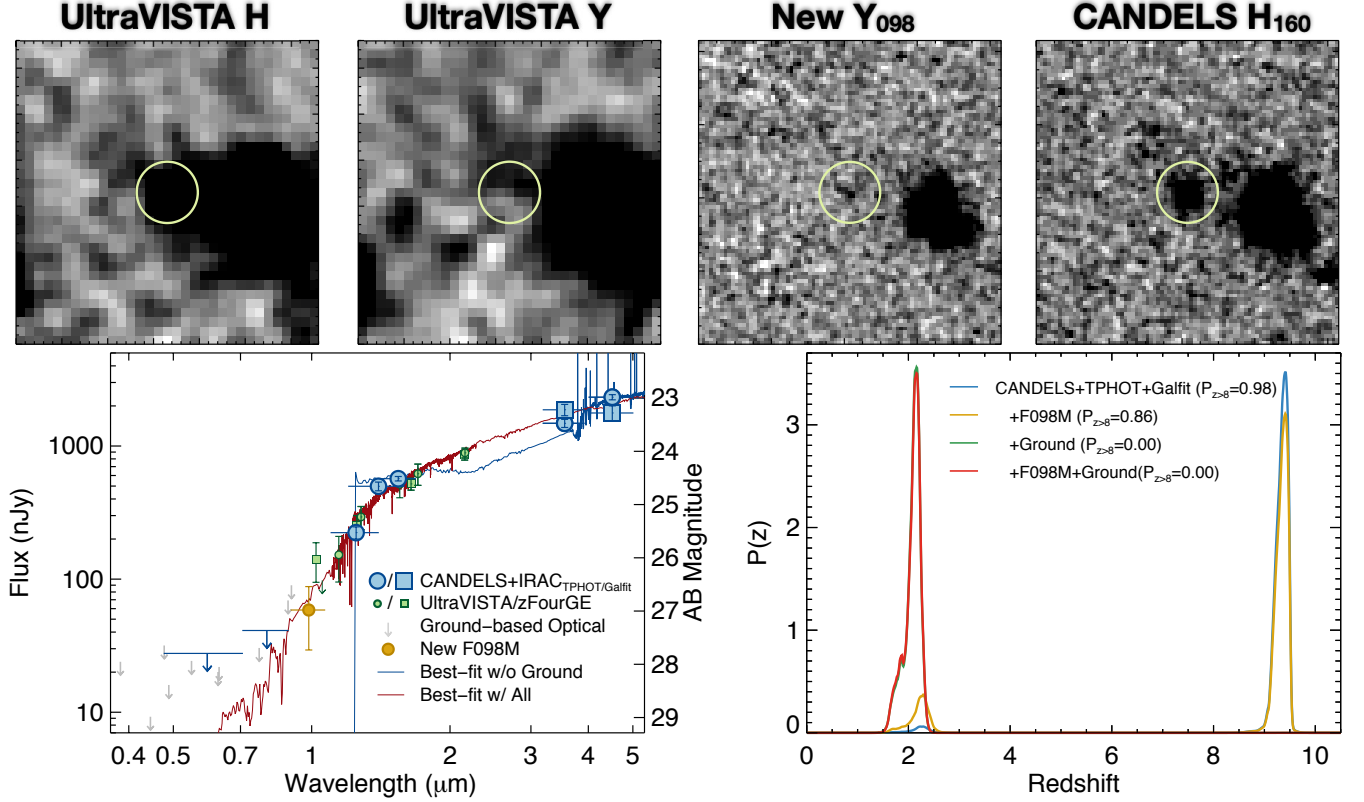


Figure 12. Top: $5'' \times 5''$ images of COSMOS_z910_14822 in the UltraVISTA H and Y bands, and the *HST* Y_{098} and H_{160} bands. While the significant flux measured in the UltraVISTA Y-band image is not coincident with the H band source, in our new F098M imaging we do see a 2.0σ detection coincident with the position of the H_{160} source. Bottom: The SED of this source is shown on the left, and EAZY $\mathcal{P}(z)$ results on the right. The addition of the Y_{098} photometry to our fiducial *HST*+IRAC fit does not change the preference for a high redshift solution (blue and yellow lines), due to the marginal nature of the Y_{098} measurement. However, adding in the ground-based photometry (green and red lines) results in a strong preference for a low-redshift solution, predominantly due to the high-significance K -band measurements showing a red $H - K$ and $K - [3.6]$ color. We thus remove this object from our sample for the remainder of our analysis.

much higher resolution. This filter probes $0.90 - 1.07 \mu\text{m}$, and a significant detection would restrict the Lyman break to be at $z < 7.8$. These data were obtained in May 2019, using a 4-point dither pattern within each orbit ("WFC3-IR-DITHER-BOX-MIN", adopting the default parameters for half-pixel sub-sampling), with a larger 2-point dither pattern across the two orbits ("WFC3-IR-DITHER-BLOB", adopting the default parameters for moving across detector defects), and specifying the SPARS25 read-out pattern with NSAMP=13, designed to provide robust up-the-ramp cosmic ray rejection. These exposures were processed beyond default calibration, following the methods outlined in Koekemoer et al. (2011), including improved background sky correction and removal of bad pixels along with other detector-level defects, as well as absolute astrometric alignment to the existing 60mas/pixel CANDELS F160W mosaics in this field.

We re-ran Source Extractor following the methodology used in §2 for our fiducial catalog, adding F098M

as a measurement image (including PSF-matching this image to the H_{160} -band, correcting for Galactic extinction, and applying an aperture correction to estimate the total flux). In our fiducial corrected Kron aperture, we measure a F098M flux of 58.6 ± 29.3 nJy, for a detection significance of 2.0σ (there is a more significant 2.7σ detection [28.0 ± 10.3 nJy] in a $0.4''$ -diameter aperture). We show a cutout of this low-significance detection in Figure 12. A faint, but likely real, source is visible in the F098M image coincident with the position of the H_{160} source. The morphology is odd in that it is streak-like, but that may be expected at such low signal-to-noise. Interestingly, as shown in this figure this flux does not line up spatially with the faint flux visible in the UltraVISTA Y-band.

To explore what constraints on the redshift these new data play, we re-ran EAZY adding this new datapoint to our fiducial set of space-based data (including both the TPHOT and GALFIT IRAC measurements in the fit). These results are shown in the lower-panel of Figure 12.

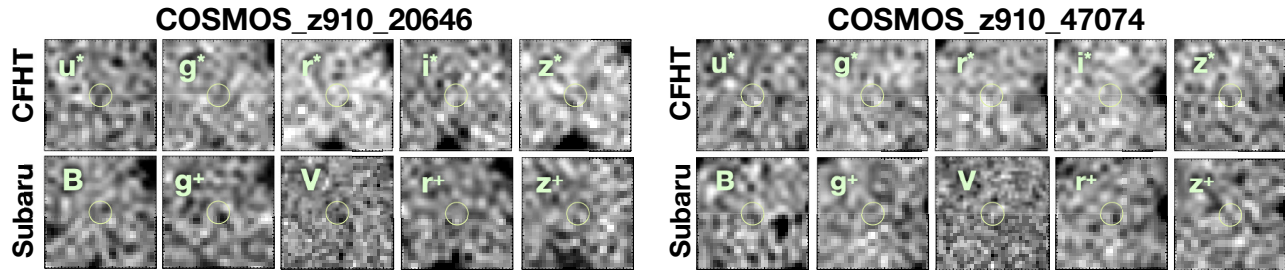


Figure 13. $5'' \times 5''$ images of the two remaining COSMOS sources (20646 on the left, and 47074 on the right) in the ground-based optical bands. Very weak detections are visible in a few bands, but offset from the position of the source. When including these fluxes in the photometric redshift modeling, the preference is still for a high-redshift solution, although a low redshift probability is present for both sources at a low ($\sim 10\%$) level.

With these space-based data alone, a high-redshift fit is still preferred, with $\int \mathcal{P}(z > 8) = 0.86$. We then ran EAZY including the ground-based photometry discussed above. Regardless of whether the new F098M data is included, the fits with the ground-based imaging strongly prefer a low-redshift solution. Since this doesn't change when the F098M imaging is removed, this implies that the ground-based photometry is driving the change in redshift. Since, as described above, the positive flux driving this shift is spatially offset from the source of interest, it is unclear whether these photometry points should be allowed to drive the fit. However, inspecting the SED in the bottom-left of Figure 12, one can see that both the UltraVISTA and ZFOURGE K_s -band photometry are more consistent with the red continuum slope expected for the lower-redshift solution. As these data have much higher S/N values than the optical points, it is likely that they drive the fits (and this is confirmed when running EAZY excluding the UltraVISTA Y-band, which does not change the result).

This analysis, including the new F098M imaging slight detection, places enough doubt on the high redshift nature of this object that we remove it from our sample for the analysis below (similar conclusions were reached in Bouwens et al. 2019 for this object [COS910-8]). Future observations of the COSMOS field with the *James Webb Space Telescope* (expected from COSMOS-Webb [PID 1727, PIs Kartaltepe and Casey] and PRIMER [PID 1837, PI Dunlop]) should better elucidate the nature of this enigmatic source.

4.2. Ground-based Photometry for All Sources

While we elected to use space-based imaging to select our sources due to the high sensitivity and small *HST* PSF, the preceding subsection highlighted how the abundance of ground-based imaging in these fields can further constrain our photometric redshifts. Here we explore how, if at all, our photometric redshift results change when we include available ground-based photometry for the remainder of our sample. The bulk of

our ground-based photometry comes from the published CANDELS-team catalogs in these fields, always scaled by H_{160} magnitude to match our catalog as discussed above. Details on the catalog measurements, and citations for specific datasets, can be found in the catalog papers cited below. Where appropriate, we measure our own photometry in more recent datasets.

EGS: In the EGS field, we make use of the ground-based photometry available in the CANDELS catalog, published in Stefanon et al. (2017b). This includes optical imaging (u', g', r', i' and z') from CFHT/MegaCam as part of the CFHT Legacy Survey, as well as two K -band photometric measurements, from KPNO/NEWMIR and CFHT/WIRCAM. All optical measurements have $S/N < 1.5$, except for the z -band for object EGS_z910.26890, which has $S/N_z = 1.79$. Five of the seven objects have $1-2\sigma$ significance detections in the CFHT K -band imaging. We re-ran EAZY including all ground-based photometry and found no significant change in the photometric redshift results for these seven objects. The marginal K -band detections are consistent with the fiducial SEDs, and the single z -band measurement is low enough significance that EAZY still strongly prefers a high-redshift solution (due to the very strong $I_{814} - J_{125}$ break, and red $[3.6] - [4.5]$ color).

GOODS-N: The single object in our GOODS-N sample, GOODSN_z910.35589, has a previously published emission-line redshift of $z = 10.957$ from Jiang et al. (2021). Nonetheless, we explore the existing ground-based photometry, to see how it affects the photometric redshift, though as this object benefits from the 11 bands of *HST* imaging available in the GOODS-N field, the photometric redshift is already fairly secure. We make use of the CANDELS catalog of Barro et al. (2019), where this object has measured non-detections in the KPNO/MOSAIC and LBT/LBC u -bands, and a detection in Subaru/MOIRCS K -band imaging. We reran EAZY, and found that these additional photometric data points did not change the previous results, which

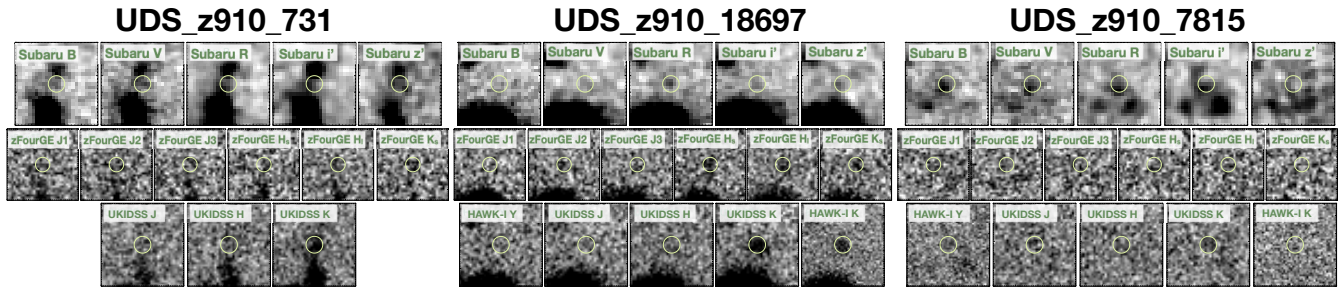


Figure 14. $5'' \times 5''$ images of the three candidate galaxies in the UDS fields in all available ground-based images. Weak optical flux is seen in many of the optical images; as discussed in the text, we attribute this flux to nearby neighbors in UDS_z910_18697 and UDS_z910_7815, removing those data from the updated photometric redshift fit. With the inclusion of the ground-based data, the updated results give $\int \mathcal{P}(z > 8) = 0.0, 1.00$ and 0.92 , for sources 731, 18697, and 7815, respectively. We thus remove object UDS_z910_731 from our final sample at this stage.

prefer $z \sim 10.4$ (the spectroscopic redshift of 10.957 is contained within the 99.5%/3 σ confidence range of the $\mathcal{P}[z]$).

COSMOS: In the COSMOS field we make use of the same ground-based data in the preceding subsection, including measuring fluxes in the ZFOURGE and UltraVISTA DR4 data. Neither of the two remaining objects in this field have detections in the UltraVISTA Y or ZFOURGE $J1$ or $J2$ bands. The object COSMOS_z910_20646 does have a measured $>2\sigma$ significance detection in two optical bands: CFHT i^* (33.3 ± 11.0 nJy; 3.0σ), and Subaru g^+ (34.8 ± 14.3 nJy; 2.4σ). inspecting these images, there is barely visible positive flux, but it is shifted relative to the expected position of the source ($\sim 0.5''$ to the SE in the CFHT i^* image, and $\sim 0.5''$ S in the Subaru g^+ image). Correspondingly, adding these ground-based data to EAZY does not significantly change the best-fit redshift, though it does introduce a small secondary peak at $z \sim 2.5$. This is consistent with the fact that there is no significant detection at the position of this object in the HST V and I bands (with 1σ upper limits at the position of this object of 8.6 and 10.5 nJy, respectively), nor in the other ground-based optical bands. Optical measurements for the object COSMOS_z910_47074 exceed 2σ only in the CFHT r^* band, at 2.4σ . Visually inspecting this image shows positive flux at this position, albeit visually consistent with the noise level. The photometric redshift continues to prefer the high-redshift solution even when including these data, dominated by the stringent non-detections in the HST V , I and Y bands (and flat $H-[3.6]$ color and non-detection in the ground-based K -bands), though the weak optical r^* flux does again lead to a small low-redshift solution. Including this ground-based photometry and re-running EAZY yields photometric redshifts which still satisfy our sample selection, with $\int \mathcal{P}(z > 8) = 0.96$ and 0.87 , and $\Delta\chi^2 = 5.2$ and 3.9 for COSMOS_z910_20646 and COSMOS_z910_47074, re-

spectively. The ground-based optical cutout images for these two sources are shown in Figure 13.

UDS: In the UDS field, we initially make use of the ground-based photometry available in the CANDELS catalog, published in Galametz et al. (2013). These include u -band imaging from CFHT/MegaCam, B , V , R_c , i' and z' imaging from Subaru/Suprime-Cam, Y and K -band imaging from VLT/HAWK-I from the HUGS survey (Fontana et al. 2014), and J , H , and K -band imaging from UKIRT/WFCAM from the UKIDSS Ultra Deep Survey (Lawrence et al. 2007). We find matches to all three of our UDS candidates within a matching radius of $0.4''$.

Exploring the optical photometry, we find that the CANDELS catalog has significant detections for all three objects in multiple Subaru filters ($>2\sigma$; up to 10σ in one case). This is surprising as these images in most cases have similar sensitivities to the CANDELS HST optical imaging used in the selection of these objects, where there was no significant flux measured. We thus investigated the position of these candidates directly in the Subaru imaging, and found that all three have nearby neighbors which may affect their measured ground-based photometry. We thus performed our own photometry at the position of these sources, following the methodology laid out in §3.5.1. In addition to the Subaru bands, we also measured photometry in the UKIDSS DR11 images, the HUGS (natural seeing) images, and the ZFOURGE near-infrared images in this field.

Starting with object UDS_z910_731, and with the filters in common between Subaru and HST /ACS, we find a Subaru V -band flux density of 48.0 ± 10.6 nJy and R -band flux density of 68.9 ± 11.5 nJy, compared to 4.6 ± 37 nJy in the HST /ACS V_{606} band. In the I -band, we find 58.6 ± 13.7 nJy with Subaru, and 37.7 ± 42.0 nJy with ACS. These values are consistent with what is seen in the images, shown in Figures 8 and 14, where

faint flux is visible in the Subaru bands, with no significant flux visible in the *HST* bands. However, this candidate is in a somewhat noisier than average region of the ACS imaging, thus the measured Subaru flux would only be detected at the $\sim 1\text{--}2\sigma$ level in the ACS imaging. Therefore the absence of flux in the ACS imaging is not completely inconsistent with the weak measured flux in the ground-based bands. A limiting factor here is the nearby galaxy $\sim 1''$ away which does not affect the *HST* photometry, but may be contributing the measured flux visible in the Subaru imaging. Nonetheless, as we cannot be sure this flux belongs to the neighbor, we conservatively include all manually measured photometry in our updated photometric redshift fitting for this source below.

Object UDS_z910.18697 has measured flux densities in the Subaru *V*, *R* and *i'* bands of 41.9 ± 8.1 nJy, 64.5 ± 10.8 nJy and 102.3 ± 13.2 nJy, respectively. In the *HST* imaging, this source has measured flux densities of -9.5 ± 14.5 nJy and 1.3 ± 15.4 nJy in the V_{606} and I_{814} bands, respectively. The *HST* measurements for this object are more sensitive than 731 discussed above, thus the *HST* non-detections are inconsistent with the Subaru measurements, at the 5σ level in the *I*-band. Inspecting Figures 8 and 14 around this position, the reason for this discrepancy is apparent – there is a very bright large spiral galaxy nearby, again $\sim 1''$ away. In the *HST* imaging, even the faintest isophote from this object is significantly far from the position of the high-redshift candidate, while in the Subaru imaging, the candidate’s position is on the wings of this source. We therefore conclude that the measured flux in the Subaru bands belongs to the bright neighbor, and we exclude the five Subaru bands from our updated photometric redshift analysis. In the ground-based near-infrared imaging, significant flux is seen in some bands at the position of this source, but as the seeing in these images is much better than the Subaru images, this flux is well-separated from the neighboring galaxy, thus we conclude it belongs to our candidate.

Object UDS_z910.7815 has measured flux densities in the Subaru *V*, *R* and *i'* bands of 34.5 ± 10.6 , 43.8 ± 11.5 and 41.6 ± 13.7 nJy, respectively. In the *HST* imaging, this source has measured flux densities of 18.5 ± 14.1 and 4.6 ± 15.8 nJy in the V_{606} and I_{814} bands, respectively. Similar to the previous object, the *HST* and Subaru photometry are seemingly inconsistent, although less so, at the 2σ level in the *I*-band. Inspecting the images in Figures 8 and 14, this discrepancy is explained as the source of the flux is offset by $\sim 0.5''$ to the SE from the candidate galaxy’s position. There is low-level positive flux at this offset position in the *HST*

images, thus we conclude that this is a nearby neighbor, and we exclude these Subaru bands from the updated photometric redshift fitting. Weak flux, at the $1.3\text{--}1.8\sigma$ level is recorded in the ZFOURGE *J1–3* bands, and is also visible at this offset position, thus we also do not include the ZFOURGE data in the updated fit for this object.

We re-ran EAZY for these objects to obtain an updated photometric redshift fit using these ground based data (omitting data where discussed above). Unsurprisingly, candidate UDS_z910.731 is now much better fit by a lower redshift ($z \sim 4$) solution, due to its likely detections in the ground-based imaging. This object is removed from our sample. Candidate UDS_z910.18697 still firmly satisfies our sample selection criteria with $\int \mathcal{P}(z > 8) = 1.00$ and $\Delta\chi^2 = 84.4$. UDS_z910.7815 does have $\int \mathcal{P}(z > 8) = 0.92$, however it now has $\Delta\chi^2 = 3.3$, just below our threshold of 3.5 for our initial sample selection. We revisit this object in §4.3.

In summary, adding the ground-based photometry removed two sources from our sample: COSMOS_z910.14822 (with further evidence provided by the weak F098M detection) and UDS_z910.731, leaving us with 12 candidate bright $z = 9\text{--}10$ galaxies. This highlights the utility of examining *all* available data when building a sample of such difficult to identify galaxies.

4.3. Cycle 27 *HST* Imaging

Although the sample of 12 candidate $z = 9\text{--}10$ galaxies still satisfies our sample selection criteria even after the inclusion of all available ground-based imaging, there are still often low-redshift solutions present in their $\mathcal{P}(z)$ ’s. We can increase the fidelity of this sample in two ways. The first is with deeper *Y*-band imaging, which falls just below the Lyman- α break at $z > 8$. Because 11/12 candidates are in the CANDELS wide fields which lack this imaging (with the exception of a few objects which were included in previous followup programs), additional *Y*-band imaging can provide higher confidence in their high-redshift nature. Secondly, while most of our objects contain some F140W imaging, it is extremely shallow. Deeper F140W imaging can both provide a second detection band at these redshifts for $z > 10$ galaxies, and can also better separate $z \sim 9$ from $z \sim 10$ galaxies.

We thus obtained additional *HST* imaging for the nine of our candidates which lacked any *Y*-band imaging from a 14-orbit Cycle 27 proposal (PID 15862; PI Finkelstein). Similar to the Cycle 26 mid-cycle observations of COSMOS_z910.14822, we elected to use F098M rather than F105W because photometric redshift simulations found that F098M is more con-

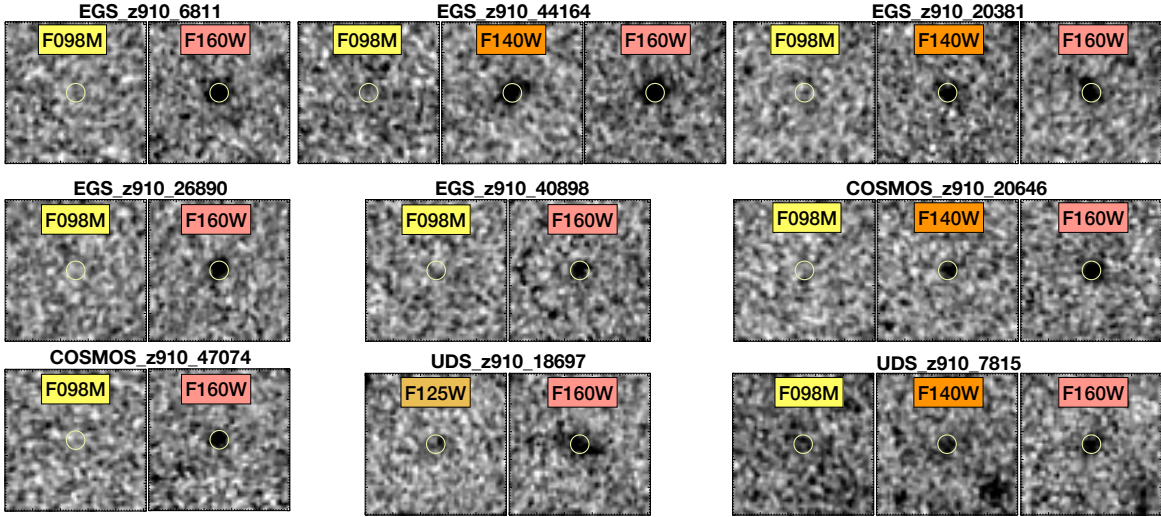


Figure 15. $3'' \times 3''$ images of the candidates which were observed with Cycle 27 *HST* imaging (F098M, F125W, and/or F160W). There is no significant ($<1.5\sigma$) detection in F098M for all sources, except UDS_z910.7815 (2.0σ). UDS_z910.18697 shows a weak (3.8σ) detection in the new deeper F125W image, which due to its low significance is not inconsistent with $z > 10$. With the exception of UDS_z910.7815, which is now equally likely to be a low-redshift interloper as a high-redshift galaxy, these new data increase the likelihood of the remaining candidates being true $z = 9-10$ galaxies.

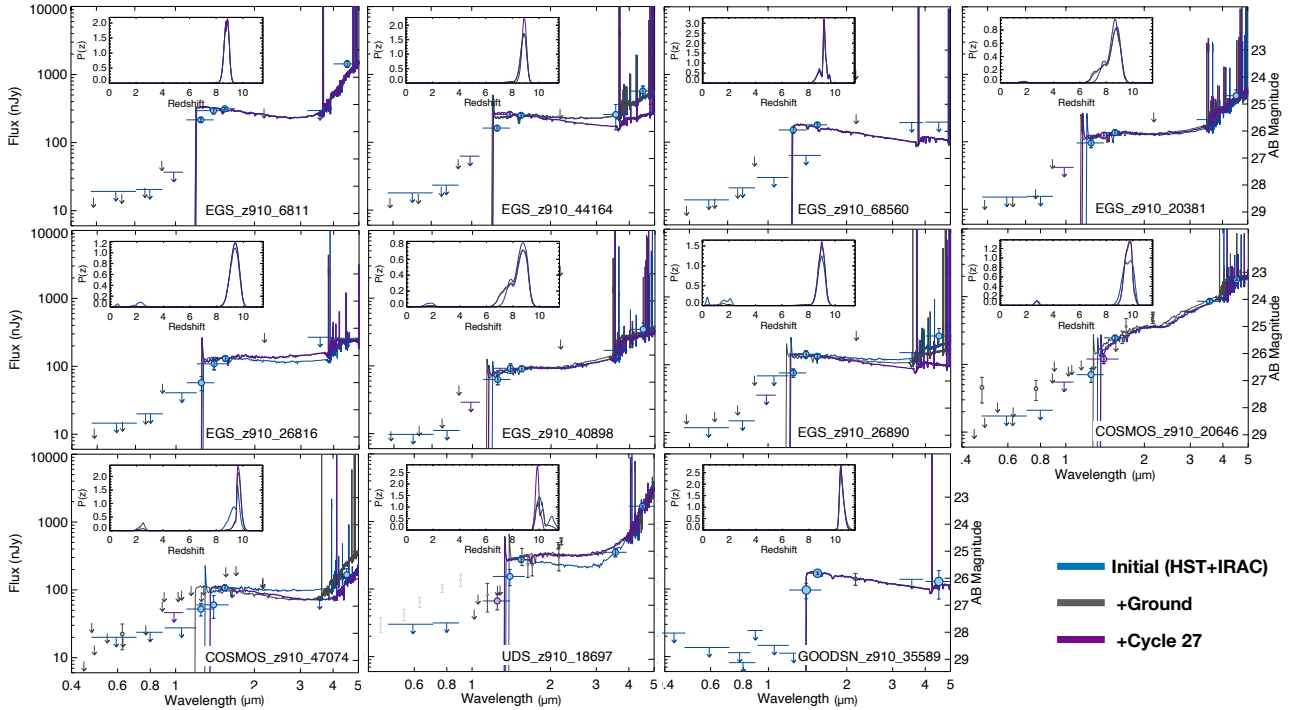


Figure 16. The observed spectral energy distributions for the 11 $z = 9-10$ galaxy candidates in our final vetted sample. Blue symbols show the initial *HST* and *Spitzer*/IRAC photometry, while gray symbols show ground-based photometry. Purple symbols denote additional photometry obtained from Cycle 27 followup programs. The best-fitting EAZY model is shown by the blue, black and purple lines for the initial, initial+ground, and initial+ground+Cycle 27 (=final) cases. The final photometric redshift PDF shows nearly no low-redshift probability in all sources.

straining. Although F098M is slightly shallower in a fixed exposure time, a faint detection in F098M would rule out a $z > 8$ solution, while the Lyman- α break is within the FWHM of the F105W filter at $z \sim 8.7$. Sources targeted in F098M were: EGS_z910.6811,

44164, 20381, 26890 and 40898, both sources in the COSMOS field, and source UDS_z910.7815. For source UDS_z910.18697 the lack of significant flux in the CANDELS F125W image points to a potential $z > 10.5$ solution, so rather than F098M we obtained additional

Table 5. Photometric Redshift Constraints with Additional Data

| ID | $\int \mathcal{P}(z > 8)$ | | | $\Delta\chi_{lowz-highz}^2$ | | |
|-------------------|---------------------------|---------|-----------|-----------------------------|---------|-----------|
| | Initial | +Ground | +Cycle 27 | Initial | +Ground | +Cycle 27 |
| EGS_z910_6811 | 0.99 | 0.99 | 1.00 | 26.5 | 40.9 | 52.5 |
| EGS_z910_44164 | 0.95 | 0.97 | 0.99 | 8.5 | 18.2 | 23.5 |
| EGS_z910_68560 | 1.00 | 1.00 | — | 24.5 | 37.8 | — |
| EGS_z910_20381 | 0.74 | 0.74 | 0.82 | 7.1 | 8.3 | 9.3 |
| EGS_z910_26890 | 0.80 | 0.94 | 0.99 | 3.5 | 6.5 | 12.9 |
| EGS_z910_26816 | 0.92 | 0.99 | — | 5.0 | 9.0 | — |
| EGS_z910_40898 | 0.69 | 0.71 | 0.80 | 5.4 | 8.0 | 8.3 |
| COSMOS_z910_20646 | 1.00 | 0.96 | 0.97 | 14.3 | 5.2 | 5.4 |
| COSMOS_z910_47074 | 0.99 | 0.87 | 0.96 | 9.2 | 3.9 | 6.7 |
| UDS_z910_18697 | 1.00 | 1.00 | 1.00 | 103.1 | 84.4 | 84.1 |
| GOODSN_z910_35589 | 1.00 | 1.00 | — | 84.1 | 84.5 | — |
| COSMOS_z910_14822 | 1.00 | 0.06 | 0.01 | 13.3 | 0.0 | 0.0 |
| UDS_z910_731 | 0.85 | 0.00 | — | 4.5 | 0.0 | — |
| UDS_z910_7815 | 0.95 | 0.92 | 0.79 | 5.1 | 3.3 | 0.9 |

NOTE—This table shows how the two key photometric redshift constraints (the integral of the PDF at $z > 8$, and the difference in χ^2 between the low and high-redshift solutions) change as additional data is added. The first column is based on the initial *HST*+IRAC selection. The second column adds ground-based data, while the third column adds additional *HST* imaging from Cycles 26 and 27. The three objects removed from our sample following this process are listed below the horizontal lines.

data in F125W. Our two additional orbits increased the F125W exposure time by a factor of four over CANDLES alone. Finally, we obtained F140W imaging for sources which either had no previous F140W coverage, or had a *HST* detection in only F160W. This was the case for objects EGS_z910_44164, EGS_z910_20381, COSMOS_z910_20646 and UDS_z910_7815.

These data were obtained between Oct 2019 and Oct 2020. The images were obtained with a similar exposure pattern and reduced in the same way as our Cycle 26 data (described in §4.1); any existing images in these filters were included in our newly reduced data. We show 3'' cutout images of our candidates in these new images (alongside the existing F160W images) in Figure 15. For the EGS and COSMOS objects, we see no significant flux in F098M, providing even stronger evidence for a $z > 8$ solution for these objects. We also see strong detections in F140W for the three galaxies in those two fields, implying these galaxies lie closer to $z \sim 9$ than 10. In object UDS_z910_18697 we elected to observe in F125W rather than F098M, and we see a very faint signal coincident with this object, with a significant detection in F140W. This near non-detection in F125W implies $z > 9.5$, and is consistent with $z \sim 10.5$ as the F125W filter has $\sim 4\%$ throughput at $1.398 \mu\text{m}$

(the observed wavelength of a $z = 10.5$ Lyman- α break). Finally, for object UDS_z910_7815, there does appear to be faint flux in the F098M image at the position of this object.

To obtain robust photometry from these new images, we first PSF-matched these images to the F160W image using the same procedures as our full catalog. As these single-WFC3-field images lack sufficient numbers of stars to create a robust PSF, we use the PSF kernels derived in the GOODS-S field (which has a large area covered by all three filters we obtained new data in). We then performed photometry with Source Extractor in an identical way as our initial cataloging, using the F160W image as the detection image, measuring and applying the empirical noise function, and applying a F160W-based aperture correction. Our photometric measurements validate what we observed in Figure 15. We measure $< 1.5\sigma$ significance detections in F098M for all objects except UDS_z910_7815, where we measure a 2.0σ significance detection (2.9σ significance when measured in a smaller $0.4''$ -diameter aperture). The three objects observed in F140W have measured flux at 5– 10σ significance. UDS_z910_18697 has a 3.8σ detection in the F125W filter.

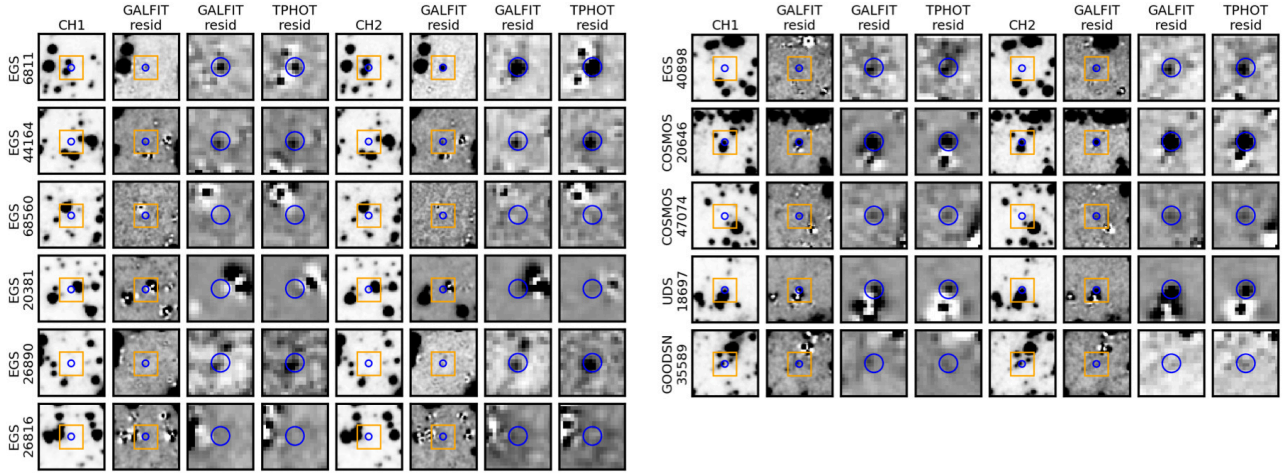


Figure 17. A comparison of IRAC deblending results between TPHOT and GALFIT. Each row contains one object. The first four columns are for the $3.6\mu\text{m}$ band. The first two columns show the IRAC image and the GALFIT residual image (the source of interest is left behind in all residual images; only neighbors have been subtracted) and are $30.6''$ on a side. The third and fourth columns show $10.2''$ zoom-ins on the GALFIT and TPHOT residual images. Columns 5-8 are the same for the $4.5\mu\text{m}$ band. Isolated sources yield similar results between GALFIT and TPHOT. Unsurprisingly, heavily crowded sources have differences in the measured photometry which can affect the photometric redshift. Two of our sample of 11 sources have best-fit solutions at $z < 8$ when combining these two photometric measurements. Due to the deblending uncertainty we ultimately keep these sources in our fiducial sample.

Table 6. IRAC Photometry Comparison

| ID | Galfit | | | | TPHOT | | | |
|-------------------|------------------|--------|------------------|-------|------------------|-------|------------------|-------|
| | $3.6\mu\text{m}$ | | $4.5\mu\text{m}$ | | $3.6\mu\text{m}$ | | $4.5\mu\text{m}$ | |
| | Flux | Error | Flux | Error | Flux | Error | Flux | Error |
| EGS_z910_6811 | 260.8 | 39.1 | 1153.5 | 3.5 | 201.1 | 147.7 | 1433.0 | 161.7 |
| EGS_z910_44164 | 125.2 | 61.6 | 238.9 | 72.3 | 256.3 | 104.0 | 568.0 | 105.5 |
| EGS_z910_68560 | 259.0 | 84.8 | 287.9 | 13.9 | -97.1 | 97.4 | -83.8 | 99.0 |
| EGS_z910_20381 | 2032.4 | 371.7 | 848.1 | 151.3 | 157.6 | 106.6 | 482.2 | 107.5 |
| EGS_z910_26890 | 239.3 | 94.0 | 36.0 | 38.0 | 107.8 | 75.5 | 265.7 | 77.5 |
| EGS_z910_26816 | 121.8 | 146.4 | 121.3 | 84.2 | 158.3 | 133.9 | 231.2 | 129.6 |
| EGS_z910_40898 | 121.4 | 34.4 | 196.5 | 37.2 | 156.7 | 84.8 | 347.0 | 85.4 |
| COSMOS_z910_20646 | 1177.2 | 1.7 | 1557.7 | 45.6 | 855.4 | 51.7 | 1782.8 | 50.7 |
| COSMOS_z910_47074 | 74.9 | 3.5 | 180.7 | 38.4 | 56.2 | 36.0 | 167.4 | 37.4 |
| UDS_z910_18697 | 1132.6 | 102.6 | 3026.1 | 93.8 | 349.7 | 49.5 | 1680.9 | 56.8 |
| GOODSN_z910_35589 | 116.7 | 2208.6 | 13.9 | 489.6 | 109.0 | 69.7 | 129.3 | 58.4 |

NOTE—All fluxes are in nJy.

To explore how these additional photometric constraints affect the photometric redshift fitting, we perform another run of EAZY, adding these new measurements to those used in the previous run (initial *HST*, IRAC and ground-based). We summarize the key results in Table 5, which broadly follow the interpretation gleaned from Figure 15, in that when there is no significant detection in F098M, the value of both $\int \mathcal{P}(z > 8)$ and $\Delta\chi^2$ increases. For the objects with

F140W imaging, the measured flux did not significantly alter the best-fitting redshift. Interestingly, in the case of UDS_z910_7815, which had the 2σ F098M detection, the EAZY analysis still prefers a high-redshift solution with $\int \mathcal{P}(z > 8) = 0.79$; lower than the fit without these new data, but still satisfying this sample selection criterion (>0.6). However, the best-fitting low-redshift solution is almost as good a match to the data as the high-redshift solution, giving $\Delta\chi^2 = 0.9$, below our threshold

of 3.5. We thus consider UDS_z910.7815 as at least a plausible low-redshift interloper, and remove it from our sample for the remainder of the analysis. Finally, for UDS_z910.18697 the addition of the deep F125W imaging, with its weak detection, did not give any further evidence against this object being a true $z \sim 10$ galaxy, as both $\int \mathcal{P}(z > 8)$ and $\Delta\chi^2$ had essentially no change with the addition of these data. Approved *JWST* Cycle 1 NIRSpec observations (PID 1758, PI Finkelstein) will soon provide a precise spectroscopic redshift for this source. We show the final SEDs and photometric-redshift PDFs for our final sample of 11 candidate $z = 9$ –10 galaxies in Figure 16.

4.4. Custom IRAC Deblending with GALFIT

In Section 4.1 we showed that different methods of IRAC deblending can result in modest changes to the photometry, which in the case of COSMOS_z910.14822, resulted in significant changes to the photometric redshift. As one final in-depth investigation into our sample of galaxies, we ran GALFIT in a similar manner on the 11 remaining sources (excluding also UDS_z910.731 and UDS_z910.7815 from the previous subsection). In Figure 17 we show the results of this additional deblending effort, showing both the original image, and the neighbor-subtracted images for both methods in both bands, and we compare photometry in Table 6. We recalculated the photometric redshifts using a combination of the TPHOT and GALFIT flux measurements, where we used the mean of the two measurements as the flux estimate, and the maximum of the two uncertainty measurements as the flux uncertainty. We found that for nine of the 11 sources, the photometric redshifts did not significantly change, with all nine continuing to satisfy our stringent selection criteria.

For two sources, the TPHOT+GALFIT photometric redshift preferred $z < 8$ solutions. For one source, EGS_z910.20381, this shift was mild, with EAZY now preferring $z = 7.4$ rather than 8.7, with $\int \mathcal{P}(z > 7) = 0.88$, albeit with $\int \mathcal{P}(z > 8) = 0.32$. Inspecting the deblending residuals in Figure 17 for this source, it does appear that TPHOT does a better job of removing the bright neighboring source, therefore we do not believe the GALFIT results nullify this object as a candidate $z = 9$ –10 galaxy.

However, the GALFIT IRAC measurements of COSMOS_z910.20646 strongly prefer a $z \sim 2.5$ solution, with no significant high-redshift peak. This object is also heavily crowded, with both TPHOT and GALFIT struggling to subtract its neighbor, thus the differences in measured fluxes represent differences in the failure to fully remove the nearby bright galaxy, rather than true

differences in the SEDs of the objects. Looking further at the photometry in Table 6, COSMOS_z910.20646 had a significant red [3.6]-[4.5] color measured with TPHOT, while the color is less red with GALFIT, explaining the shift in $\mathcal{P}(z)$ to lower redshift. These differences depending on which photometric method is used highlight a systematic uncertainty when making use of deblended photometry from low-resolution imaging, something which will be alleviated soon with *JWST*. Given the uncertainty regarding which method is more accurate, we keep this source in our sample, though we caution the reader that this nature of this galaxy is still somewhat uncertain.

4.5. Gravitational Lensing Magnification

Due to the bright nature of our sample of candidate $z = 9$ –10 galaxies, we must consider the possibility that their apparent brightness has been magnified by sources near to the line-of-sight. While sources along all lines of sight are subject to weak lensing by the total mass distribution along the line of sight, the correction for this is statistical in nature, and is likely small for blank fields such as the CANDELS fields our candidate galaxies reside in. Here we thus consider strong lensing, which we can estimate and correct for on a source-by-source basis. We follow the methodology of Mason et al. (2015b), who derive a relationship between the observed brightness of $z < 3$ bright ($m < 23$) galaxies and their velocity dispersions. Using our observed fluxes and derived photometric redshifts, we use the Mason et al. (2015b) relations to estimate the velocity dispersions for galaxies within $10''$ of our high-redshift candidates, restricting potential lenses to those with best-fit photometric redshifts of $z < 3$.

This process provides an estimate of the lensing potential of any source near to an object of interest, which can be used with Equation 4 from Mason et al. (2015b) to calculate the size of the Einstein radius. Using the measured separation between our object of interest and the nearby potentially lensing galaxy, this radius can be used to calculate the magnification. This magnification is dependent on the photometric redshift of both the source and the lens object, and the observed flux of the lens object, all of which are measured at varying levels of precision. Additionally, the Mason et al. (2015b) velocity dispersion – apparent magnitude relations also have sizable uncertainties. We account for these sources of error by sampling all uncertainties via Monte Carlo simulations, deriving the magnification for each nearby source 1000 times, sampling the photometric redshift PDF for both the source and lens, perturbing the H_{160} -band flux of the lens within its uncertainty, and perturb-

ing the velocity dispersion – magnitude relations within their fit uncertainties. The fiducial magnification and its uncertainty is the median and standard deviation of these 1000 values.

Considering all sources within $10''$ and taking the results at face value implied significant magnifications for all 11 objects, with a median magnification for each candidate of $\mu = 1.8$, obtained by combining all neighbors per candidate. This high magnification is surprising as even intermediate lenses should be somewhat rare. To explore whether this procedure results in a bias towards higher magnification factors, we ran the following test. For each of our 11 candidates, we simulated placing the candidate at 1000 different positions in its respective CANDELS field by randomly selecting similarly-bright sources (i.e., $m \sim 25-26.5$) and replacing the $\mathcal{P}(z)$ of the random source with that of our candidate. After repeating our magnification calculation as described above, we found that the median magnification for all 1000 positions was measured to be $\mu \approx 1.4$. As the physical expectation is unity, clearly considering all nearby sources results in the potential for an excess positive bias in the magnification. Additionally, this methodology was designed to determine magnifications for intermediate ($\mu > 1.4$) and strong ($\mu > 2$) lensing, whereas all of the magnifications for our candidates (when calculated individually for each close neighbor) are consistent with weak ($\mu < 1.4$) lensing. Based on these results, we consider only potential lenses which result in median magnifications of $\mu > 1.4$.

We found that none of our 11 candidates had a nearby source within $10''$ with a median magnification of $\mu > 1.4$, thus we do not apply any magnification correction to our sample. We note that two sources do have close companions which have estimated $1.3 < \mu < 1.4$. EGS_z910_20381 has a $V = 19.3$ galaxy at $z_{phot,lens} = 0.3$ at a separation of $3.6''$, with a median magnification of $\mu = 1.32$, while UDS_z910.18697 has a $H_{160} = 20.8$ galaxy at $z_{lens} = 1.1$ with a separation of $3.0''$, with a median magnification of $\mu = 1.35$. Both of these magnifications have sizable uncertainties, thus it is possible that both sources are being significantly magnified. While within our present uncertainties we cannot conclusively determine this magnification, should future work obtain spectroscopic redshifts for both source and lens, and perform more robust mass modeling of the lens, this magnification could be better determined.

4.6. Calculation of UV Absolute Magnitudes

Here we measure the rest-frame UV absolute magnitudes. We follow convention in this field and we use 1500 \AA rest-frame as our reference UV wavelength. While

at our redshifts of interest this is contained within the H_{160} -band, we can more accurately estimate the flux at this rest-frame wavelength by using all available photometry. We do this following the method of Finkelstein et al. (2015c), SED fitting the *HST+Spitzer* photometry for an object, measuring the bandpass-averaged flux through a 100 \AA -wide top-hat filter centered at rest-frame 1500 \AA . We then use the photometric redshifts to convert this flux to a rest-frame UV absolute magnitude (M_{UV}). We calculate uncertainties on these derived magnitudes via Monte Carlo simulations (see Finkelstein et al. 2015c for more details), perturbing both the photometry and the photometric redshifts within their uncertainties. For the purposes of this calculation we assume that all candidates are truly at $z > 8$, thus we remove any low-redshift solution from the $\mathcal{P}(z)$ such that it does not contribute to the M_{UV} uncertainty budget. Our inferred values of M_{UV} are listed in Table 7.

4.7. Final Sample Summary

As described in the above section, our additional vetting including all available ground-based data reduces our sample size from 14 to 11 candidate bright $z > 8.5$ galaxies. This final sample is summarized by the blue-shaded histograms in Figure 7. Interestingly, two of the candidates which were removed were the two brightest in our sample ($H = 24.5$ and 25.0). These two sources also both have red H_{160} -[3.6] colors of > 1 mag, implying that red H_{160} -[3.6] colors may be a good discriminator against contaminants (see also discussion in Bouwens et al. 2019). The H_{160} -[3.6] color distribution for our initial sample is shown in the right-hand panel of Figure 7. There is one remaining object in our sample with $H - [3.6] > 1$, COSMOS_z910_20646. As discussed above, this object does present a potential low-redshift solution which becomes dominant if the GALFIT-based IRAC photometry is used; with the TPHOT-based IRAC photometry it still satisfies our sample selection criteria with $\int \mathcal{P}(z > 8) = 0.96$. We also explored the sizes of our sources to see whether a combination of half-light radius and H_{160} -[3.6] color could help discern contaminants. However, we found that 13/14 initial candidates had half-light radii of 1–3 pixels ($< 0.2''$), with the size not correlated with H_{160} -[3.6] color. The exception is UDS_z910_731, which has the largest size ($r_h = 4.2$ pixels) and the reddest H_{160} -[3.6] color (1.6 mag). Thus outliers with both red H_{160} -[3.6] color and large sizes may identify potential contaminants in future samples.

For the remainder of this work, we use the photometric redshift results when including all available data (ground-based and Cycle 26 and 27 *HST*), with the final

Table 7. Final Sample Summary

| ID | $\int \mathcal{P}(z > 8)$ | z_{best} | z_{spec} | $\int \mathcal{P}(z \approx 9)$ | $\int \mathcal{P}(z \approx 10)$ | Sample | M_{UV} |
|-------------------|---------------------------|-------------------------|-------------------------------------|---------------------------------|----------------------------------|--------|--------------------------|
| EGS_z910_6811 | 1.00 | $8.84^{+0.12}_{-0.25}$ | $8.683^{+0.001\dagger}_{-0.004}$ | 0.92 | 0.00 | 9 | $-22.13^{+0.05}_{-0.03}$ |
| EGS_z910_44164 | 0.99 | $8.87^{+0.19}_{-0.17}$ | $8.665 \pm 0.001^\ddagger$ | 0.97 | 0.00 | 9 | $-21.87^{+0.05}_{-0.05}$ |
| EGS_z910_68560 | 1.00 | $9.15^{+0.17}_{-0.34}$ | | 0.92 | 0.05 | 9 | $-21.49^{+0.11}_{-0.09}$ |
| EGS_z910_20381 | 0.82 | $8.67^{+0.32}_{-0.74}$ | | 0.56 | 0.01 | 9 | $-21.20^{+0.14}_{-0.12}$ |
| EGS_z910_26890 | 0.99 | $8.99^{+0.22}_{-0.29}$ | | 0.94 | 0.01 | 9 | $-21.26^{+0.11}_{-0.09}$ |
| EGS_z910_26816 | 0.99 | $9.38^{+0.28}_{-0.39}$ | | 0.66 | 0.32 | 9 | $-21.28^{+0.14}_{-0.12}$ |
| EGS_z910_40898 | 0.80 | $8.77^{+0.25}_{-0.90}$ | | 0.55 | 0.01 | 9 | $-20.80^{+0.18}_{-0.13}$ |
| COSMOS_z910_20646 | 0.97 | $9.80^{+0.10}_{-0.46}$ | | 0.29 | 0.68 | 10 | $-22.26^{+0.29}_{-0.04}$ |
| COSMOS_z910_47074 | 0.96 | $9.64^{+0.22}_{-0.13}$ | | 0.11 | 0.85 | 10 | $-21.11^{+0.10}_{-0.11}$ |
| UDS_z910_18697 | 1.00 | $9.89^{+0.16}_{-0.15}$ | | 0.00 | 0.99 | 10 | $-22.25^{+0.12}_{-0.10}$ |
| GOODSN_z910_35589 | 1.00 | $10.41^{+0.24}_{-0.08}$ | $10.957 \pm 0.001^{\dagger\dagger}$ | 0.00 | 0.58 | 10 | $-21.91^{+0.03}_{-0.11}$ |

NOTE—A summary of the final sample of candidate $z > 8.5$ galaxies. The photometric redshift quantities shown include photometry from ground-based data and Cycle 27 *HST* imaging, as discussed in §4. The fifth and sixth columns show the integral of the redshift $\mathcal{P}(z)$ in $\Delta z = 1$ bins centered at $z = 9$ and 10 , respectively. The higher of these two quantities sets whether the galaxy is placed in the $z = 9$ or $z = 10$ sample. The UV absolute magnitude is derived via SED fitting, with the uncertainty inclusive of both photometric and photometric redshift uncertainties. † Spectroscopic redshift measurement from Zitrin et al. (2015) based on Ly α emission. ‡ Spectroscopic redshift measurement from Larson et al. (2021) based on Ly α emission. †† Spectroscopic redshift measurement from Jiang et al. (2021) based on rest-UV metal lines, consistent with the Oesch et al. (2016) grism redshift from the Ly α break.

Table 8. Final Sample Photometry

| ID | F606W | F814W | F098M | F105W | F125W | F140W | F160W | 3.6 μ m | 4.5 μ m |
|-------------------|-----------------|-----------------|------------------|------------------|------------------|------------------|------------------|-------------------|--------------------|
| EGS_z910_6811 | 2.3 ± 9.6 | 4.3 ± 10.3 | -11.0 ± 18.4 | — | 215.8 ± 15.1 | 294.9 ± 30.9 | 314.5 ± 13.3 | 201.1 ± 147.7 | 1433.0 ± 161.7 |
| EGS_z910_44164 | -3.6 ± 9.0 | 1.2 ± 11.7 | 41.7 ± 31.2 | — | 161.9 ± 14.0 | 257.7 ± 19.2 | 249.2 ± 15.5 | 256.3 ± 104.0 | 568.0 ± 105.5 |
| EGS_z910_68560 | -4.0 ± 7.0 | -3.7 ± 10.6 | — | -30.0 ± 15.0 | 151.5 ± 15.3 | 8.1 ± 31.9 | 180.2 ± 12.7 | -97.1 ± 97.4 | -83.8 ± 99.0 |
| EGS_z910_20381 | -9.4 ± 7.6 | -2.7 ± 7.8 | 8.1 ± 20.9 | — | 96.2 ± 14.3 | 124.7 ± 13.3 | 137.0 ± 13.1 | 157.6 ± 106.6 | 482.2 ± 107.5 |
| EGS_z910_26890 | -3.3 ± 5.9 | 5.8 ± 7.4 | -18.5 ± 17.8 | 62.6 ± 34.3 | 75.8 ± 10.7 | 143.1 ± 17.3 | 133.3 ± 8.9 | 107.8 ± 75.5 | 265.7 ± 77.5 |
| EGS_z910_26816 | -4.0 ± 7.3 | 1.4 ± 10.0 | — | -4.5 ± 20.4 | 57.3 ± 13.6 | 108.8 ± 20.2 | 130.3 ± 12.1 | 158.3 ± 133.9 | 231.2 ± 129.6 |
| EGS_z910_40898 | -1.3 ± 4.9 | -2.2 ± 5.6 | 3.8 ± 14.5 | — | 62.9 ± 10.2 | 92.2 ± 14.8 | 91.1 ± 8.9 | 156.7 ± 84.8 | 347.0 ± 85.4 |
| COSMOS_z910_20646 | 3.9 ± 8.6 | 2.6 ± 10.5 | 21.3 ± 26.9 | — | 70.5 ± 16.1 | 119.8 ± 16.9 | 246.0 ± 17.6 | 855.4 ± 51.7 | 1782.8 ± 50.7 |
| COSMOS_z910_47074 | -5.2 ± 10.0 | -3.6 ± 11.9 | -22.6 ± 23.3 | 4.6 ± 13.8 | 52.2 ± 11.0 | 60.1 ± 22.1 | 107.7 ± 10.3 | 56.2 ± 36.0 | 167.4 ± 37.4 |
| UDS_z910_18697 | -9.5 ± 14.5 | 1.3 ± 15.4 | — | — | 66.5 ± 17.4 | 152.2 ± 41.4 | 270.1 ± 22.2 | 349.7 ± 49.5 | 1680.9 ± 56.8 |
| GOODSN_z910_35589 | -1.8 ± 6.8 | 1.6 ± 4.1 | — | -2.8 ± 7.3 | 3.6 ± 5.6 | 96.6 ± 24.8 | 171.2 ± 7.8 | 109.0 ± 69.7 | 129.3 ± 58.4 |

NOTE—All fluxes are in nJy.

values listed in Table 7. In this table we split our sample into two redshift bins, $z \sim 9$ and $z \sim 10$. To decide which bin a galaxy is in, we use the integrated redshift probability distribution functions, where galaxies with $\int_{8.5}^{9.5} \mathcal{P}(z) > \int_{9.5}^{10.5} \mathcal{P}(z)$ are in the $z \sim 9$ sample, and vice versa. As seen in Table 7, seven of our sources fall in the $z \sim 9$ bin, and four in the $z \sim 10$ bin. Finally, we list the full *HST*+IRAC photometry for all sources in our final sample in Table 8.

5. COMPARISON TO PREVIOUS CANDELS SAMPLES

Previously, Oesch et al. (2014), Bouwens et al. (2015b), Bouwens et al. (2016a) and Bouwens et al. (2019) have selected bright $z > 8.5$ candidate galaxies in the CANDELS fields. We restrict our comparison primarily to Bouwens et al. (2019), as it is inclusive of the previous work listed and it has a larger number

of candidates than Bouwens et al. (2016a) due to the adoption of photometric redshift selection in Bouwens et al. (2019), rather than strict color-color selection as was adopted in Bouwens et al. (2016a). Here we discuss each of our candidates and provide a discussion of whether or not they were previously published.

5.1. Previously Published Candidates in Our Sample

- Candidate EGS_z910.6811 – This candidate galaxy was originally published in Roberts-Borsani et al. (2016) as $z = 8.6$ candidate galaxy in particular due to its very red [3.6]–[4.5] color. It was then spectroscopically confirmed via Ly α emission by Zitrin et al. (2015) to have $z_{spec} = 8.683$, in excellent agreement with our photometric redshift of $8.84_{-0.25}^{+0.12}$. We also see a red IRAC color, though note that this source is heavily crowded in IRAC, so the true IRAC color is difficult to discern. This object was not selected in the color-selection employed by Bouwens et al. (2016a), but is included (as EGS910-10) in the photometric-redshift selection of Bouwens et al. (2019), who find a similar brightness and photometric redshift as we do ($m_H = 25.3$ and $z_{phot} = 8.6$).
- Candidate EGS_z910.44164 – This candidate galaxy was not published in original work in this field (Bouwens et al. 2016a), but was included (as EGS910-8) in the selection of Bouwens et al. (2019). We find $m_H = 25.4 \pm 0.1$, which is somewhat brighter than the Bouwens et al. (2019) value of 25.7 ± 0.1 . Our photometric redshift of $z_{phot} = 8.87_{-0.17}^{+0.19}$ is consistent with the value of $z_{phot} = 9.1$ from Bouwens et al. (2019).
- Candidate EGS_z910.20381 – This candidate galaxy was also not published originally, but was included (as EGS910-9) in the recent selection of Bouwens et al. (2019). Our redshift estimates are consistent ($8.67_{-0.74}^{+0.32}$ for this work, and 9.1 for Bouwens et al. 2019), and our H_{160} -band magnitudes are identical ($H = 26.1$). In the appendix of Bouwens et al. (2019) this candidate is also listed as EGS910-13, with identical coordinates as their EGS910-9, but a brighter magnitude (25.9) and a lower photometric redshift (8.5).
- Candidate EGS_z910.26890 – This candidate galaxy was not included in the fiducial sample of $z \sim 9$ candidates by Bouwens et al. (2019), but it was listed as a possible $z \sim 9$ candidate (as EGS910-15) as they measured $z_{phot} = 8.3$ with $\int \mathcal{P}(z > 8) = 0.38$ (including our F098M

data presented here, Bouwens et al. 2021 find $\int \mathcal{P}(z > 8) = 0.56$). Our photometric redshift is significantly higher at $8.99_{-0.29}^{+0.22}$, and correspondingly $\int \mathcal{P}(z > 8)$ is shifted higher as well to 0.99. Their slightly lower redshift may be driven by the weakly significant positive flux in the Y_{105} -band at the position of this galaxy (62.6 ± 34.3 nJy; 1.8σ). However, this object falls on the edge of the F105W pointing (which was targeting another galaxy), with only 800 sec of integration, compared to the full depth of >3000 sec, and upon visual inspection is not distinguished from several other nearby bright noise peaks. Regardless, this object was stringently not detected in our Cycle 27 F098M imaging (-18.5 ± 17.8 nJy). We measure a strong red $J_{125} - JH_{140}$ break of 0.7 mag, with a blue $JH_{140} - H_{160}$ color of -0.1 mag (and $H_{160} - [3.6]$ of -0.2 mag). This implies that the galaxy is intrinsically blue, with the break in the J_{125} -band, but mostly out of the JH_{140} -band. This implies that the Ly α break must be near to the blue edge of the F140W filter; if it were any bluer, the $J_{125} - JH_{140}$ would not be as red as observed. Likewise, if it were any redder, the $JH_{140} - H_{160}$ would be redder than observed. The blue edge of the F140W filter is at $1.2\mu\text{m}$, and a Ly α break observed at that wavelength would have $z \approx 8.9$, similar to our inferred photometric redshift.

- Candidate EGS_z910.26816 – This candidate has been published in both Bouwens et al. (2016a) and Bouwens et al. (2019) as EGS910-0. Our brightness measures are similar (26.1–26.2), and their measurement of $z_{phot} = 9.1_{-0.4}^{+0.3}$ is consistent with our value of $z_{phot} = 9.38_{-0.39}^{+0.28}$.
- Candidate COSMOS_z910.47074 – This candidate has also been published in both Bouwens et al. (2016a) and Bouwens et al. (2019) as COS910-1. Our brightness measures are also similar (26.3–26.4). Their redshift measurement of $z_{phot} = 9.0_{-0.5}^{+0.4}$ is lower than ours of $9.64_{-0.13}^{+0.22}$, though the difference is not highly significant.
- Candidate UDS_z910.18697 – This candidate galaxy was not included in the fiducial sample of Bouwens et al. (2019), but it was listed as a possible $z \sim 9$ candidate (as UDS910-13). Without ground-based imaging, they find $z_{phot} = 9.7$, but with the inclusion of ground-based imaging, this drops to $z_{phot} = 2.3$, based on a 4σ detection in the ZFOURGE J2 band in their catalog (which would imply $z < 7.7$). In our examination of these

data, we also see positive flux in J2 (Figure 14). However, with our noise calculations we find this is less significant ($<2\sigma$). Combined with the non-detections in ZFOURGE J1 and J3 filters, EAZY still prefers a $z > 9$. As discussed above, the ground-based photometry may be affected by a nearby large bright galaxy, thus the nature of this source is still a bit unclear.

- Candidate GOODSN_z910_35589 – This object was first published in Oesch et al. (2014) as GN-z910-1 with $z_{phot} = 10.2 \pm 0.4$, and was further found by Oesch et al. (2016) to have a detectable continuum break in HST grism spectroscopy consistent with $z_{grism} = 11.1 \pm 0.1$. Recently, Jiang et al. (2021) have refined the redshift to $z = 10.957 \pm 0.001$ via weak rest-UV metal emission lines. Both spectroscopic measurements are consistent within $<2\sigma$ of our measurement of $z_{phot} = 10.41^{+0.30}_{-0.07}$. Our measured H_{160} -band magnitude is a little brighter at 25.82 ± 0.05 , versus 26.0 ± 0.1 (from Bouwens et al. 2019).

5.2. Candidates in Our Sample Published for the First Time

Three of our candidate galaxies are being published here for the first time.

- Candidate EGS_z910_68560 – This candidate galaxy has $m_H = 25.8 \pm 0.1$, and $z_{phot} = 9.15^{+0.17}_{-0.34}$, with $\int \mathcal{P}(z > 8) = 1.0$. This object may have been excluded by other studies due to its mild $J_{125} - H_{160}$ color of only 0.2 mag, yet the complete non-detection in Y_{105} strongly constrains $z > 8.5$. Interestingly, this source does not appear at a significant level in the JH_{140} imaging, which is unexpected given its brightness. This could imply that the J_{125} and H_{160} counts are due to persistence prior to the CANDELS observation. However, we examined this in §3.3.1, and found that the previous observations did not have a high fluence at this position, therefore this explanation is disfavored.
- Candidate EGS_z910_40898 – This candidate galaxy has $m_H = 26.5 \pm 0.1$, and $z_{phot} = 8.77^{+0.25}_{-0.90}$ with $\int \mathcal{P}(z > 8) = 0.80$. This galaxy has $J_{125} - H_{160} = 0.40$, which is slightly bluer than commonly used color-selection thresholds (~ 0.5). It has a red [3.6]–[4.5] color, consistent with strong [O III] emission at the derived photometric redshift.
- Candidate COSMOS_z910_20646 – This candidate galaxy has $m_H = 25.4 \pm 0.1$, and $z_{phot} = 9.80^{+0.10}_{-0.46}$

with $\int \mathcal{P}(z > 8) = 0.97$. Its red observed $J_{125} - H_{160}$ color of 1.4 mag is consistent with its high derived photometric redshift. As discussed above, this object does have a fairly red SED, with $H - [3.6] = 1.35$ mag, as red as the two sources removed as being low-redshift interlopers. Additionally, the IRAC fluxes of this source are uncertain due to nearby blended neighbors. However, even with ground-based imaging and a Cycle 27 F098M non-detection, this source still satisfies our selection criteria (though there is a small secondary redshift peak at $z \sim 2.5$).

5.3. Published Candidates Not in Our Sample

Here we discuss the 12 galaxy candidates previously published by Bouwens et al. (2019, hereafter B19) which are not in our final sample. Of their 12 galaxies which are not in our sample, they measure $H > 26.6$ for nine of them, fainter than we consider here. However, as noted above, our magnitudes sometimes differ, so we searched our catalog for all 12 of these galaxies, and here we describe our measurements for these candidates.

EGS910-2 (B19 $H_{160} = 26.70$): We measure $H_{160} = 26.99$, thus this object is too faint for our sample, though our measurement of $\int \mathcal{P}(z > 8) = 0.53$ is somewhat consistent with a $z > 8$ solution.

EGS910-3 (B19 $H_{160} = 26.40$): We measure $H_{160} = 26.58$ with a H_{160} -band SNR=4.9, thus this object's SNR is too low for our sample, though our measurement of $\int \mathcal{P}(z > 8) = 0.92$ is very consistent with a $z > 8$ solution.

UDS910-1 (B19 $H_{160} = 26.60$): We measure $H_{160} = 26.43$, thus this object is bright enough for our sample, and its $\mathcal{P}(z)$ distribution clears our cutoff with $\int \mathcal{P}(z > 8) = 0.64$. However, the secondary low-redshift solution we find for this source is nearly as good as the high-redshift solution, with $\Delta\chi^2 = 1.2$, thus this misses our $\Delta\chi^2 > 3.5$ cutoff for the difference in χ^2 between the low and high-redshift solutions, though it is still consistent with a $z > 8$ solution.

UDS910-5 (B19 $H_{160} = 25.80$): We measure $H_{160} = 25.3$, thus this object is bright enough for our sample. However, our photometric redshift has a best-fit solution at $z_{phot} = 1.16$, with $\int \mathcal{P}(z > 8) = 0.09$, failing our selection criteria. We explored this further, and found that this galaxy lies off the eastern edge of the CANDELS ACS mosaic, thus our catalog lacks the necessary optical photometry to constrain the redshift. B19 made use of ground-based optical imaging in this region to select this galaxy.

GS-z9-1 (B19 $H_{160} = 26.60$): We measure $H_{160} = 26.94$, thus this object is just too faint for our sample, though our measurement of $\int \mathcal{P}(z > 8) = 0.99$ is very consistent with a $z > 8$ solution.

GS-z9-2 (B19 $H_{160} = 26.90$): We measure $H_{160} = 27.21$, thus this object is just too faint for our sample. Our measurement of $\int \mathcal{P}(z > 8) = 0.31$ is not consistent with a $z > 8$ solution. This object does not exhibit significant flux in our optical bands, but we find a very red $H-[3.6]$ color, which makes for a very broad $\mathcal{P}(z)$. However, this object has a near neighbor crowding this source in the IRAC imaging, so the deblended IRAC flux may not be accurate.

GS-z9-3 (B19 $H_{160} = 26.90$): We measure $H_{160} = 27.08$, thus this object is too faint for our sample, though our measurement of $\int \mathcal{P}(z > 8) = 0.99$ is very consistent with a $z > 8$ solution.

GS-z9-4 (B19 $H_{160} = 26.8$): This object is not in our catalog as it is not in the CANDELS GOODS-S proper region. It is in the HUDF09-2 flanking field, which we did not include in our analysis. The B19 magnitude for this source was 26.8, so it likely would not have been bright enough for inclusion in our sample had we used these additional data.

GS-z9-5 (B19 $H_{160} = 26.4$): We measure $H_{160} = 26.04$, $\int \mathcal{P}(z > 8) = 0.72$, and $\Delta\chi^2 = 3.7$, satisfying those specific selection criteria. However, our photometric redshift distribution has $\int \mathcal{P}(z \sim 8) > \int \mathcal{P}(z \sim 9)$. Our results thus imply a redshift closer to $z \sim 8$, though a $z \sim 9$ solution is plausible.

GS-z10-1 (B19 $H_{160} = 26.90$): We measure $H_{160} = 27.12$, thus this object is just too faint for our sample. Our measurement of $\int \mathcal{P}(z > 8) = 0.67$ clears our sample selection threshold of 0.6, with a best-fitting redshift is $z_{phot} = 9.91$. The optical photometry may be affected by a very close neighbor just South of this source, leading to a larger secondary redshift peak at $z \sim 2.5$.

GN-z9-1 (B19 $H_{160} = 26.60$): We measure $H_{160} = 26.79$, thus this object is too faint for our sample, though our measurement of $\int \mathcal{P}(z > 8) = 1.00$ is very consistent with a $z > 8$ solution.

GN-z10-2 (B19 $H_{160} = 26.80$): We measure $H_{160} = 26.98$, thus this object is too faint for our sample. Our measurement of $\int \mathcal{P}(z > 8) = 0.32$ is also too low for our sample, though the best-fitting redshift is $z_{phot} = 9.95$. However, the $\mathcal{P}(z)$ is very broad, due to the faintness of this object, as well as a very bright nearby galaxy affecting the IRAC photometry.

GN-z10-3 (B19 $H_{160} = 26.80$): We measure $H_{160} = 26.90$, thus this object is too faint for our sample. Our measurement of $\int \mathcal{P}(z > 8) = 0.57$ is just a bit too low for our sample, though the best-fitting redshift is $z_{phot} = 9.77$. This object has a somewhat broad $\mathcal{P}(z)$, primarily due to its faint nature, as nothing in the imaging is inconsistent with a high redshift solution (although this object does not have F140W coverage).

In summary, the majority of the B19 sources which are not in our sample are fainter than we considered in this study, though our measurements for most are consistent with a high-redshift nature. Of the two sources that are bright enough for our sample, for only one (GS-z9-5) did we use similar data in the selection, and this one just narrowly misses our sample. We conclude that our sample selection is inclusive yet accurate, as we recover nearly all previously published sources which we should have, as well as adding a few sources not previously published.

6. LUMINOSITY FUNCTION ESTIMATION

In this section we measure the rest-UV luminosity function of our candidate sample of $z > 8.5$ galaxies. In order to do this, we need to estimate our completeness in each field, as a function of source brightness, which we describe in the following subsection.

6.1. Estimating the Completeness

To calculate our luminosity function, we use the effective volume method, where

$$V_{eff}(M) = \int \frac{dV}{dz} P(M, z) dz \quad (4)$$

where dV/dz is the comoving volume element, and $P(M, z)$ is the probability that an object at a given absolute magnitude and redshift satisfies our sample selection criteria. We estimate $P(M, z)$ using completeness simulations. Our method follows our previous work (e.g., Finkelstein et al. 2015c; Rojas-Ruiz et al. 2020).

We performed a more detailed set (compared to §2.2) of completeness simulations separately in each of the five CANDELS fields. In each field, we ran 50 iterations of our simulation, where in every iteration we place 10,000 mock galaxies across each of the images for each field, for a total sample of 500,000 mock galaxies per field. We build SEDs of the mock galaxies to derive their bandpass-averaged fluxes in each filter available in a given field. First, we draw a random redshift uniformly over the range $4.5 < z < 11.5$. Then for each object, we draw an H_{160} -band magnitude from a random distribution over $22 < H < 28.5$. We use a combination of two

log-normal distributions, a slowly-rising log-normal distribution from $H = 22$ to 25, and a steeper log-normal distribution from $H = 25$ to 28.5. This combination results in $\sim 50\%$ of the simulated objects having $H < 26.6$, where our sample lies. To ensure robust statistics at the bright end, every 10th simulation iteration simulated only $22 < H < 25$ galaxies with a flat distribution in magnitude.

We also draw stellar population ages (in log units), metallicities and dust attenuation values from log-normal distributions, with typical values of $\log(\text{age/yr}) \sim 7.4$, $Z = 0.2Z_{\odot}$, and $E(B-V) = 0.15$. The combination of these values produces a UV spectral slope $\beta = -2.0$, similar to those observed for bright $z > 9$ galaxies (e.g., Wilkins et al. 2016). We use these properties to generate colors from a Bruzual & Charlot (2003) model, normalizing the model to the H_{160} -band magnitude for a given mock object.

Mock galaxy images are generated via GALFIT (Peng et al. 2002), with Sersic indices drawn from a log-normal distribution of the form $n = e^{\mathcal{R}} + 0.8$ (restricted to $1 < n < 5$), which has a peak at $n = 1.2$, with 60% of the distribution at $n < 2$. The axis ratios are drawn from a log-normal distribution tilted towards high values (median $b/a = 0.75$), and position angles are drawn from a uniform random distribution. We draw galaxy half-light radii using observed relations between galaxy size and their absolute UV magnitudes, using a relation similar to that found by Kawamata et al. (2018) at $z = 6-7$, of the form

$$r_h(M_{UV}) = 0.94 \times 10^{-0.4(M_{UV}+21)\beta} [kpc] \quad (5)$$

where M_{UV} is the absolute UV magnitude of an object, and β is the slope of the size-luminosity relation. We assume $\beta = 0.25$ for bright ($M < -21$) galaxies, and 0.5 for fainter galaxies. We apply a scatter of 0.2 dex to these sizes to represent the intrinsic scatter at fixed magnitude. These GALFIT images are normalized to the magnitude for a given object in a given filter, and convolved with the measured point-spread function (PSF). As our images have all been PSF-matched to the H_{160} -band, we use the H_{160} -band PSF derived for each field (§ 2.4) as the PSF for all bands in a given field for these simulations. Finally, the galaxy images are added to a random position of the real image.

When we applied the half-light radius functional form from Equation 5 directly in our simulations, our completeness values were lower than (the near-unity) expected for very bright ($H < 25$) simulated sources. We inspected the results of the simulations to determine why bright sources were rejected, and found that it was primarily due to low S/N (failing the $S/N_H > 7$ criterion) due to somewhat large sizes. To determine if this

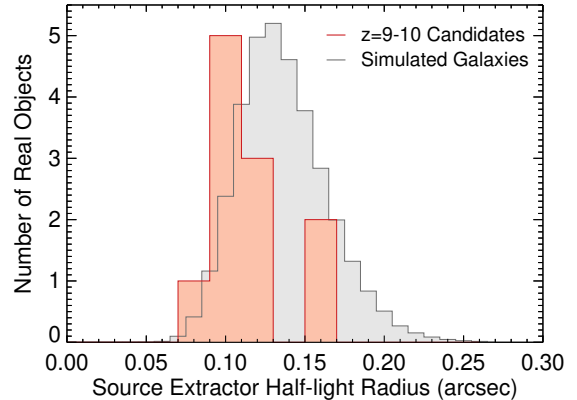


Figure 18. The half-light radius distribution measured by Source Extractor for our final list of candidates (red) compared to that for sources recovered from the completeness simulations (gray). We tuned the later to approximately match the former to ensure that we are not over-correcting our observations for a population of extended sources which are not known to exist. Should future surveys find such a population, it would increase the completeness corrections above what we have applied to our luminosity functions, increasing the derived number densities.

was appropriate, we compared the half-light radii of our sample of high-redshift galaxies to those recovered in our simulations, and found that the latter were too large by a factor of ~ 2 . Given that our largest source in our catalog has $r_h = 0.15''$, the volumes derived from completeness simulations where the bulk of simulated sources are larger than that would be artificially too small. We thus modified Equation 5 by a single scale factor to reduce the radii, such that the median of the recovered simulated galaxies approximately matched those we observe. Applying a scale factor of 0.25 results in a recovered simulated value of $r_h = 0.138 \pm 0.029''$, compared to $0.11 \pm 0.030''$ for our sample of candidate galaxies. We show these distributions in Figure 18. We thus applied this scale factor to our simulated galaxy images to ensure that we did not artificially reduce the effective volume. We note that this makes the explicit assumption that all bright $z = 9-10$ galaxies have similar sizes to those in our sample, which is a necessary assumption until significantly deeper wide-field imaging is available to test this hypothesis.

We then measured photometry and photometric redshifts using Source Extractor and EAZY, respectively, in an identical way as done on our real science images, including measuring empirical flux uncertainties based on the aperture sizes and positions of the sources in the images. For each simulation, we matched galaxies in the recovered photometric catalog to the input catalog, counting a source as a recovered match if it was

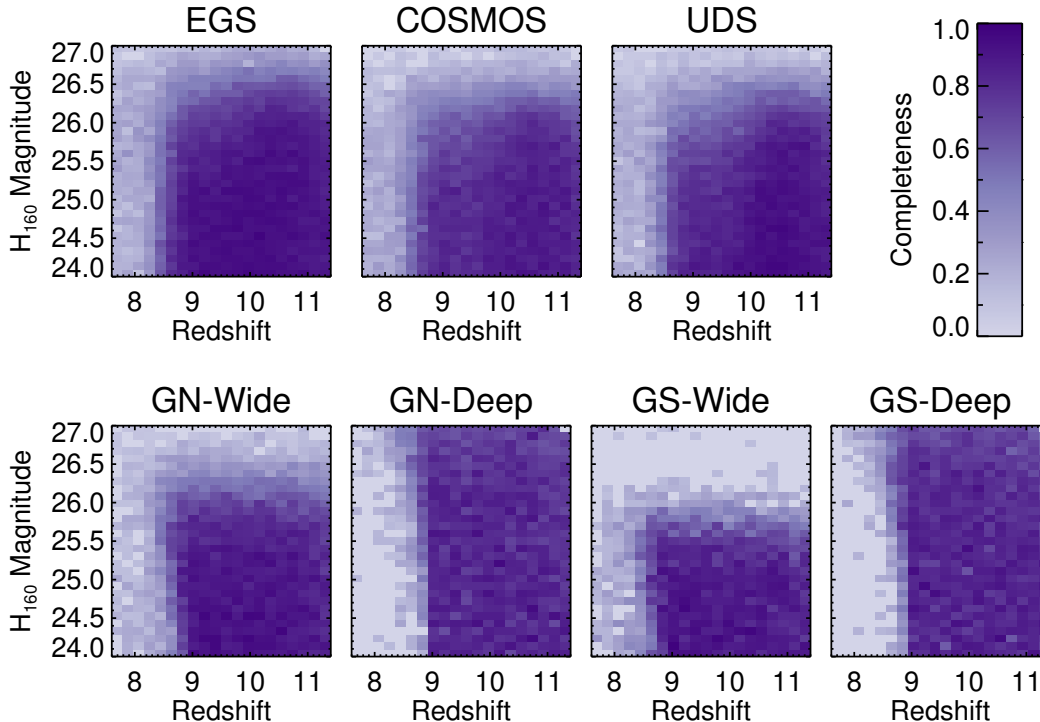


Figure 19. Each panel shows the results of completeness simulations from one of our five fields. The GOODS fields are split by their depth (the GOODS-S ERS field is not shown, but results are in between the Deep and Wide fields). The shading denotes the completeness as a function of H_{160} -band magnitude and redshift, as shown by the color bar. Our selection process results in a redshift selection function which peaks between $8.5 < z < 10.5$, as desired. We see that completeness falls off rapidly at $H > 26$ in the CANDELS wide fields, while the deep fields remain complete to fainter magnitudes as expected.

$< 0.2''$ from the input position (e.g., roughly within one PSF FWHM). Recovered objects were then subject to the same signal-to-noise and photometric redshift quality criteria as for our real sample. We calculated the completeness in bins of input magnitude and redshift as the number of fully recovered sources (e.g., found by Source Extractor, and passing all sample selection cuts) divided by the number of input sources per bin. We note that in our previous work (Finkelstein et al. 2015c) we calculated, at significantly increased computational cost, the completeness additionally as a function of half-light radius and UV slope β . As expected, we found that the completeness depends sensitively on size, and weakly on β . To account for these effects in this work, we have tuned the parameters of the simulated galaxies such that their sizes and colors roughly match the observed sample of galaxies (see also the preceding paragraph).

Figure 19 summarizes these completeness simulations. Each panel shows the completeness in bins of redshift and H_{160} -band magnitude for one of our five fields. The completeness peaks at $z \sim 8.5-10.5$, which is consistent with the filter set available. The redshift selection functions are shown in the left-hand panel of Figure 20. In the right-hand panel of Figure 20 we show the effective volume as a function of absolute magnitude, calculated

following Equation 4. We tabulate these volumes in Table 9.

We compared our volumes to those calculated by Bouwens et al. (2019), who used a similar dataset, though with differences in the sample selection and simulation methodology. While they do not list their volumes directly, they can be inferred from their published number densities and the number of galaxies in their sample in each magnitude bin. We found that our effective volume matches the sum of their $z \approx 9$ and $z \approx 10$ volumes.

6.2. Calculating Observed Number Densities

Due to the small number of galaxies in our sample, as well as the relative short time period between the $z \sim 9$ and 10 epochs, we elect to study our sample in a single redshift bin, spanning $z \sim 8.5-11$. To calculate the observed number densities, we follow the methodology of Finkelstein et al. (2015c) to calculate both these values and their associated uncertainties. We use a Markov Chain Monte Carlo (MCMC) method which employs a goodness-of-fit statistic (\mathcal{C}^2) which models the probability distribution as a Poissonian distribution, proper for these small numbers, with

$$\mathcal{C}^2(\phi) = -2 \ln \mathcal{L}(\phi) \quad (6)$$

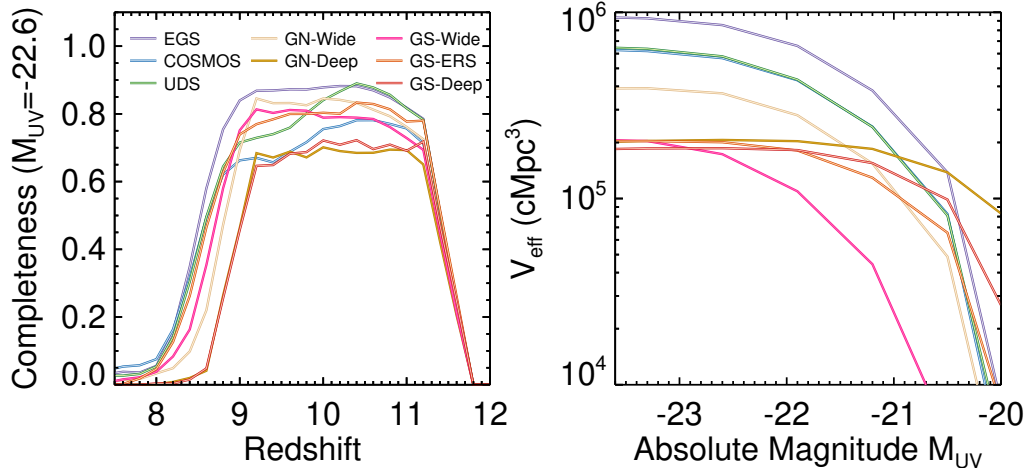


Figure 20. Left) The completeness as a function of redshift for simulated galaxies at $M_{UV} = -22.6$. The redshift distributions are peaked at $z \sim 9-11$, matching our selection criteria. Right) Effective volume versus absolute magnitude, with the same colors as in the left panel. The differences in effective volume between the fields depend on both the area per field (Table 9) and the completeness of a given field.

Table 9. Effective Volumes

| Field | Area (arcmin ²) | Effective Volume (10 ⁴ Mpc ³) | | | |
|-------------|-----------------------------|------------------------------------------------------|-----------|-----------|-----------|
| | | $M=-22.6$ | $M=-21.9$ | $M=-21.2$ | $M=-20.5$ |
| EGS | 205.9 | 89.43 | 72.86 | 35.76 | 5.42 |
| COSMOS | 159.8 | 59.09 | 48.28 | 22.07 | 2.59 |
| UDS | 153.5 | 60.62 | 48.51 | 21.38 | 2.75 |
| GOODSN–Wide | 101.3 | 39.11 | 31.73 | 13.19 | 1.34 |
| GOODSN–Deep | 67.7 | 20.57 | 20.72 | 19.67 | 15.01 |
| GOODSS–Wide | 53.2 | 19.52 | 11.68 | 1.59 | 0.05 |
| GOODSS–ERS | 49.2 | 20.52 | 19.44 | 14.38 | 4.95 |
| GOODSS–Deep | 60.2 | 18.75 | 18.45 | 17.40 | 10.63 |
| Total | 850.7 | 327.6 | 271.7 | 145.4 | 42.8 |

NOTE—The areas covered by each of our fields, and the effective volumes probed, calculated by our completeness simulations in four bins of absolute magnitude.

$$C^2(\phi) = -2 \sum_i \sum_j N_{j,\text{obs}} \ln(N_{j,\text{expected}}) - N_{j,\text{expected}} - \ln(N_{j,\text{obs}}!) \quad (7)$$

where $\mathcal{L}(\phi)$ is the likelihood that the expected number of galaxies (N_{expected}) matches that observed (N_{obs}) for a given differential number density ϕ (in units of number $\text{Mpc}^{-3} \text{mag}^{-1}$). The MCMC sampler used is described in Finkelstein et al. (2019). For this work, we run a burn-in consisting of 10^5 steps, which we found sufficient for the sampler to find a minimum, and we then measured our posterior from a subsequent 10^4 steps. The median of this posterior distribution in each redshift/magnitude bin is the fiducial number density value, while the uncertainty is taken as the 68% central width.

The differential luminosity function is typically calculated in magnitude bins. This can lead to a bias where the bin centers and width choices can significantly affect the derived number densities with such a small sample. While this can be avoided by assuming a specific functional form (Schmidt et al. 2014), the form of the bright end of the $z > 8$ luminosity function is not known, thus this choice also imparts a bias. In an effort to avoid these biases, we implement a novel “pseudo”-binning procedure within our MCMC. When we calculate the number density at a given value of M_{UV} , in each step of the MCMC chain, a random value of the binsize is chosen from 0.3 – 1.5 mag. We then draw an absolute magnitude for each source by sampling the absolute

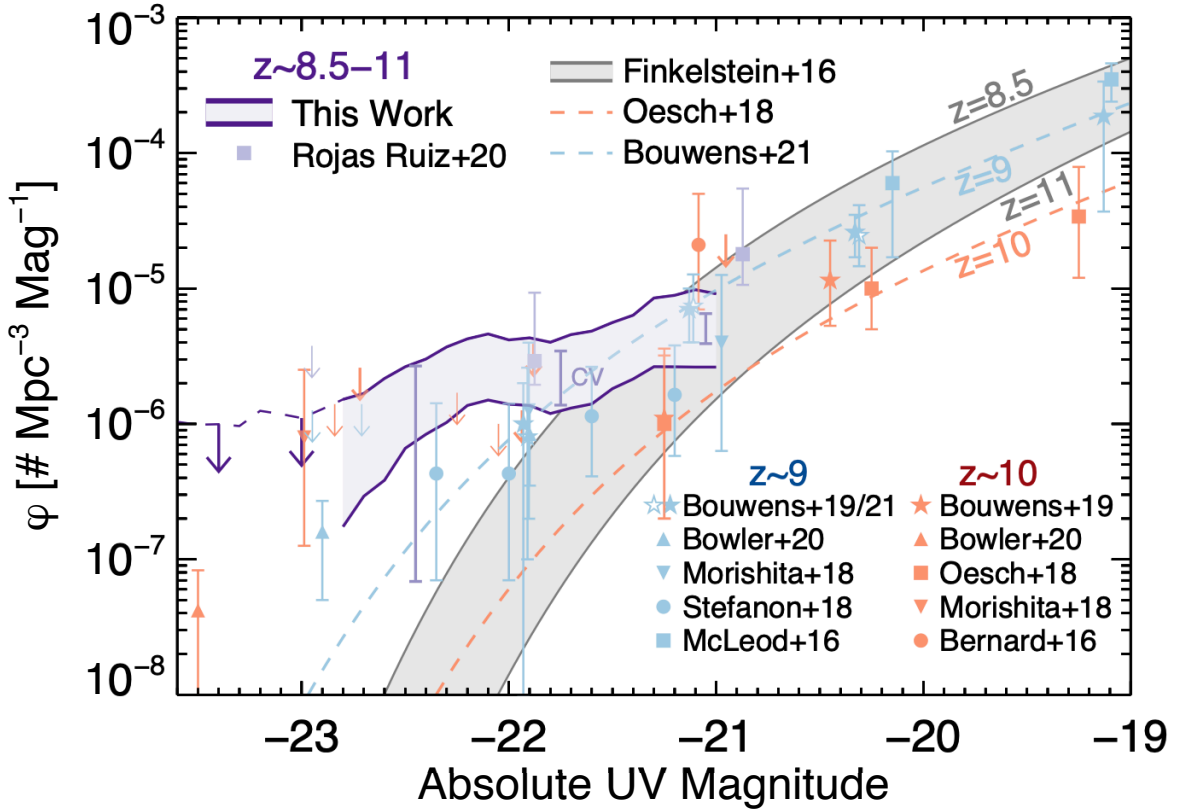


Figure 21. The measured number densities using our pseudo-binning technique on our candidate galaxy sample at $z \approx 8.5-11$ (purple shaded region; the dashed portion shows the 84% confidence upper limit brighter than the magnitude of our brightest observed source) compared to various recent literature results color-coded by redshift bin. We also show the smoothly evolving predicted Schechter function from [Finkelstein \(2016\)](#), with the shaded gray region denoting its evolution from $z = 8.5-11$, as well as the measured $z = 9$ and 10 Schechter functions from [Bouwens et al. \(2021\)](#) and [Oesch et al. \(2018\)](#), respectively. The three error bars at either end and in the middle of our results represent the estimated cosmic variance uncertainty, which is less than the measured Poisson uncertainty except at the brightest end. Our results are consistent with previously published luminosity functions at $M_{UV} \sim -21$, while at brighter luminosities our results lie at the upper end of some previous studies, possibly boosted by an apparent overdensity in the EGS field (§7). Our results are consistent with a scenario where the bright end evolves less rapidly than the faint-end of the luminosity function, similar to what was found by [Bowler et al. \(2020\)](#). Due to the large uncertainties on the number densities, we cannot conclusively distinguish between smooth or rapid evolution of the UV luminosity function at $z > 8$.

magnitude posterior distributions (see §4.6; this allows galaxies to effectively move bins), calculating N_{obs} for each bin. This procedure is repeated along each step of the MCMC chain, allowing the derived number density to encompass uncertainties in the absolute magnitudes and marginalizing over changes in the results due to the bin size. We perform this calculation in steps of 0.1 mag from $M_{UV} = -24$ to -20 . We checked that these results are in agreement with a standard binning scheme by comparing these results to those obtained with a bin-size of 0.7 mag, finding good agreement.

We report these number density values in [Table 10](#), and plot them in [Figure 21](#), where we also compare to a variety of recent results from the literature. We estimate the uncertainty due to cosmic variance via the estimator provided by [Bhowmick et al. \(2020\)](#) based on the BlueTides simulation. We calculate this independently

for each field using the appropriate field geometry, combining the results in quadrature. We find a fractional uncertainty on the linear number density due to cosmic variance of 0.95, 0.43, 0.25 in the -22.5 , -21.75 and -21.0 magnitude bins, respectively. We plot these uncertainties as secondary error bars next to the relevant data points in [Figure 21](#). With the exception of our brightest luminosities probed, these estimated cosmic variance uncertainties are lower than the Poisson uncertainties, implying that our results are Poisson-noise limited. This is not surprising given the small number of detected galaxies, though we also note that these cosmic variance uncertainties are dependent on this specific simulation.

6.3. Implications

6.3.1. Comparison to Previous Observational Results

Table 10. Measured Number Densities for $z=9-11$

| Magnitude Bin | Number Density (10^{-6} Mpc^{-3}) |
|---------------|-----------------------------------------------|
| -22.7 | <0.96 |
| -22.6 | $1.050^{+1.115}_{-0.666}$ |
| -22.5 | $1.373^{+1.270}_{-0.712}$ |
| -22.4 | $1.674^{+1.338}_{-0.835}$ |
| -22.3 | $1.985^{+1.715}_{-0.959}$ |
| -22.2 | $2.389^{+1.857}_{-1.020}$ |
| -22.1 | $2.681^{+1.936}_{-1.180}$ |
| -22.0 | $2.511^{+1.657}_{-1.113}$ |
| -21.9 | $2.617^{+1.700}_{-1.248}$ |
| -21.8 | $2.414^{+1.593}_{-1.220}$ |
| -21.7 | $2.827^{+1.738}_{-1.517}$ |
| -21.6 | $2.864^{+1.981}_{-1.459}$ |
| -21.5 | $3.306^{+2.300}_{-1.483}$ |
| -21.4 | $3.789^{+2.560}_{-1.641}$ |
| -21.3 | $4.798^{+3.705}_{-2.151}$ |
| -21.2 | $4.824^{+4.075}_{-2.181}$ |
| -21.1 | $5.125^{+4.664}_{-2.497}$ |
| -21.0 | $5.218^{+3.922}_{-2.590}$ |

NOTE—Number densities estimated via MCMC with Poisson uncertainties, estimated at each magnitude over a variety of potential bin sizes. We estimate the additional fractional uncertainty due to cosmic variance as 0.95, 0.43, 0.25 at $M_{UV} = -22.5$, -21.75 and -21.0 , respectively, using the estimator provided by Bhowmick et al. (2020).

Here we compare to previous results, which typically examined $z = 9$ and $z = 10$ separately. Examining Figure 21, the number density at our faintest luminosities is consistent with previous results at both $z = 9$ and 10 within our uncertainties. The middle of our probed range at $M_{UV} = -21.9$ is comparable to what was found by Rojas-Ruiz et al. (2020) over a similar wide-redshift bin, though it is somewhat higher than found by other studies at both $z \sim 9$ and 10. However, this tension is not significant due to the large (Poisson and cosmic variance) uncertainties. Finally, our brightest luminosities probed have a number density consistent with previous results by Stefanon et al. (2019) and Morishita et al. (2018). This number density is also broadly consistent with the very shallow bright-end decline suggested by Bowler et al. (2020). However, at these bright luminosities both the Poisson and cosmic variance uncertainties are significant. Additionally, as we describe in §7, our sample does appear to contain one overdense structure

which could bias our results high, though the galaxies in the EGS field are not the most luminous in our sample.

We also compare to the empirically predicted Schechter luminosity function from Finkelstein (2016), shown by the gray shaded region. This prediction is based on the assumption that the smooth decline in the luminosity function observed at $z = 4$ to 8 continues to higher redshift. This is in contrast to the accelerated decline in the luminosity function proposed by Oesch et al. (2018) and Bouwens et al. (2019); we show the $z = 9$ (10) luminosity function estimated by Bouwens et al. (2021) (Oesch et al. 2018) as the blue (red) dashed line. Our faintest results are consistent with both the smooth and accelerated decline, while our brightest results lie above both the smooth and accelerated decline-based luminosity functions (though these scenarios differ the most at the faint end, which we do not probe). This result agrees with recent ground-based observations by Bowler et al. (2020), who propose that the bright end of the luminosity function is evolving less rapidly than the faint-end at these redshifts. While our brightest measurement provides weak evidence against the accelerated decline scenario, given the uncertainties we conclude that down to our sample limit of $H_{160}=26.6$ we cannot prove or disprove this scenario at a significant confidence level with the existing data.

6.3.2. Physical Interpretation

A number of physical properties can affect the bright end of the rest-frame UV luminosity function. It is well-known that the observed UV light from galaxies suffers from dust attenuation, with the specific amount of attenuation dependent on the galaxy mass or luminosity and redshift (e.g., Finkelstein et al. 2012b; Bouwens et al. 2014). The abundance of UV-bright galaxies can also depend on the amount of light coming from an accretion disk around a central supermassive black hole, though given the paucity of known bright AGNs at $z > 7$, this is likely unimportant at the epoch studied here (though some of the observed light may still be due to low-luminosity AGN within these galaxies). The efficiency of the conversion of gas into stars can also affect the bright end of the luminosity function, with a steeper relation between the surface density of SFR and gas mass leading to a shallower bright-end decline (e.g. Yung et al. 2019). An evolving initial mass function (IMF) could also affect the UV luminosity function; in a scenario where higher redshift galaxies have more progressively top-heavy IMFs (presumably due to decreasing metallicity), one would expect the shape of the UV luminosity function to change as the mass-to-(UV)light ratio decreases. Finally, the evolution of the bright end

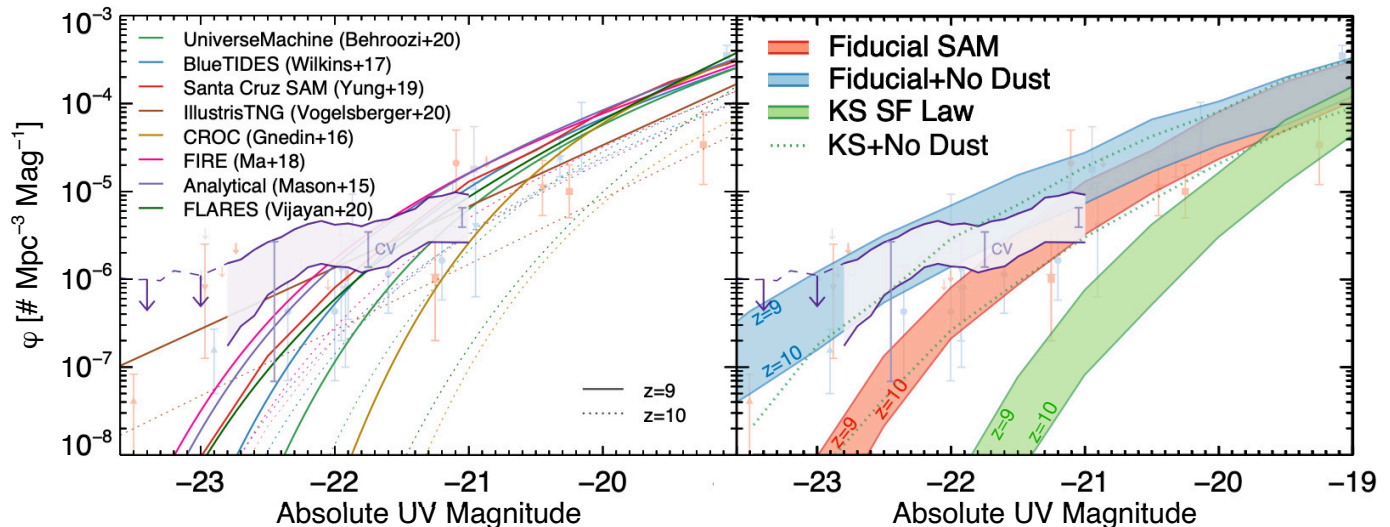


Figure 22. A comparison of luminosity functions from observations (with the same symbols as in Figure 21) to recent theoretical predictions. Our results are shown by the purple shaded region. Left) Predictions from hydrodynamical models (BlueTIDES, Wilkins et al. 2017; IllustrisTNG, Vogelsberger et al. 2020; CROC, Gnedin 2016; FIRE, Ma et al. 2018; FLARES, Vijayan et al. 2020), an analytical calculation (Mason et al. 2015a), an empirical model (UniverseMachine, Behroozi et al. 2020), and a semi-analytic model (Santa Cruz SAM, Yung et al. 2019). Solid (dotted) lines denote predictions at $z = 9$ (10). Predictions are generally consistent with observations within the uncertainties, except that the CROC and Universe Machine models under-predict the number density of our brightest bin. Right) Predictions solely from the Santa Cruz SAM, with their fiducial model in red, a model with no dust attenuation in blue, and a model with a shallower dependence of the SFR on gas density in green (shaded is with dust; the dotted green lines are with no dust). Changing the dust attenuation and the SF scaling dependence both significantly affect the bright end. Our observations are consistent with a SF with a steeper dependence on gas density than the classic Kennicutt-Schmidt relation, though the exact dependence is degenerate with the normalization of this relation and the amount of dust attenuation in bright galaxies.

will also trace the rate at which negative feedback effects on star formation (e.g., AGN feedback, stellar feedback) first manifest. If these effects are not significant in massive galaxies in this epoch, the bright end could be out of equilibrium and show an excess of star-forming galaxies compared to later times (e.g., Peng et al. 2010).

Theoretical predictions in this epoch are rapidly maturing given the imminent launch of *JWST*. However, many of the above physical properties require subgrid assumptions, thus by comparing these predictions to our observations we can begin to bound the assumptions in these models. In the left-hand panel of Figure 22 we compare our observations and those from the literature to the predicted luminosity functions from simulations. This comparison includes hydrodynamic simulations (BlueTIDES, Wilkins et al. 2017; IllustrisTNG, Vogelsberger et al. 2020; CROC, Gnedin 2016; FIRE, Ma et al. 2018; FLARES, Vijayan et al. 2020), analytical calculations (Mason et al. 2015a), empirical models (UniverseMachine, Behroozi et al. 2020), and semi-analytic models (Santa Cruz SAM, Yung et al. 2019). As our sample spans $z \sim 9-10$ we plot both epochs, though the $z = 9$ lines are more relevant for comparison

as the median of the stacked $\mathcal{L}(z)$ for our entire sample is 9.1 (Figure 23).

Starting at our faintest observed end, we note that some models over-predict our observed number densities at $z = 9$. These same models at $z = 10$ are fairly consistent with our observations, but as our median redshift is closer to $z = 9$ it does appear that our observations imply a somewhat lower number density than some models. This tension is most noticeable in the FIRE and analytic models shown, though even those models are consistent within $\sim 2\sigma$ confidence. There are more interesting differences between the predictions and our observations in our brighter probed luminosities. Here, the aforementioned three models are very consistent with our data, but both the CROC and UniverseMachine models significantly under-predict the observed number density.

This implies that some of the various physical assumptions (e.g., dust attenuation, star-formation recipes) in these models need revising to match observations, unsurprising as observations in this epoch are nascent with large uncertainties. Nonetheless, in the right panel of Figure 22 we show how the Yung et al. (2019) SAM predictions change if we alter two specific properties likely to significantly change the bright end. The red shaded

region shows the fiducial luminosity function from the SAM (where the shading denotes the evolution from $z = 9$ to 10), which does a reasonable job at our faintest observed luminosities, though it does under-predict our brightest observations.

In blue we show the SAM predictions when no dust attenuation is applied, which matches the brightest luminosities we probed fairly well, though somewhat over-predicts the fainter luminosities. This implies that a modification to the dust attenuation which results in a decreased attenuation for brighter galaxies relative to fainter galaxies could improve the agreement of these predictions with our observations. However, Finkelstein et al. (2012b) found that bright galaxies from $z = 4$ –8 have seemingly uniform rest-UV colors implying the presence of some dust, thus this scenario seems less likely. The colors of our sample of galaxies are further explored by Tacchella et al. (2021), are consistent with a similar amount of dust attenuation as similarly massive galaxies at $z = 4$ –8. This implies that differences in dust attenuation at the bright end are not a favored explanation by observations for the lack of bright-end evolution; we refer the reader to Tacchella et al. (2021) for further discussion.

The fiducial model of Yung et al. (2019) adopts a broken power law relation between molecular gas surface density and star formation rate density, with a slope of unity below a critical H_2 surface density ($70M_{\odot}pc^{-2}$) and a slope of 2 above that critical density. In green, we show the SAM predictions for an alternative model in which a classical Kennicutt-Schmidt (KS) relation (Schmidt 1959; Kennicutt 1989) is adopted, where $\Sigma_{SFR} \propto \Sigma_{gas}^N$ with $N = 1.5$ (where here Σ_{gas} includes both molecular and atomic gas). This model does equally well as the fiducial one at reproducing the properties of lower redshift galaxies (Somerville et al. 2015), but one can see that the predictions for the number density of high redshift galaxies are starkly different — a shallower SFR law index lowers the entire predicted luminosity function, with the difference most notable at the bright end. Even given the sizable observational uncertainties, and the modeling uncertainties especially with regard to the amount of dust extinction in these galaxies, our measured luminosity function is strongly inconsistent with a SF law with a slope of $N = 1.5$ assuming the model’s parameterization of dust attenuation (e.g., the $N = 1.5$ SF law with no dust [dotted green lines] also does well to represent the data, but as discussed above a dust-free nature is extremely unlikely, especially for bright galaxies). We note that the SF law adopted in the fiducial model of Yung et al. (2019) is consistent with the observationally derived

SF law in nearby and intermediate redshift ($z \sim 1$ –2) galaxies (Narayanan et al. 2012; Kennicutt & De Los Reyes 2021). However, uncertainties in the conversion factor between CO and molecular gas and how it depends on galaxy properties make it unclear whether the slope of the SF law steepens at high gas density, or whether instead starburst galaxies have a SF law with a higher normalization (Kennicutt & De Los Reyes 2021). Regardless, it is clear that these distant galaxies have much shorter gas depletion times, implying higher SF efficiencies, than nearby typical spiral galaxies. The star-formation law in the early universe can be better characterized with *JWST*, which will independently constrain the dust attenuation in individual galaxies with improved photometry (and, for the first time in this epoch, spectroscopy).

7. EGS OVERDENSITY AT $Z \sim 9$

One of the most striking properties of our sample is that although we included five (roughly) equivalently sized fields, the distribution of sources is very non-uniform, with seven of our 11 candidates coming from a single field, the EGS field. This was also observed by Bouwens et al. (2019), who found that the relative normalization of the luminosity function in the EGS-field alone was $\sim 2.5 (\pm 1.1)$ \times higher than that derived from all five CANDELS fields. While our small sample is dominated by uncertainties (primarily Poisson, but also cosmic variance), it is worth considering this potential overdensity in more detail.

We first estimate the significance of this potential $z \sim 9$ structure by drawing random samples of galaxies from a 2 deg² mock catalog (Yang et al. 2021; Somerville et al. 2021) based on the Santa-Cruz semi-analytic model of Yung et al. (2019). We extracted the number of galaxies in unit redshift bins from $z = 8.5$ –9.5 (encompassing the likely redshifts of the seven EGS sources) down to our magnitude limit of $H = 26.6$ in non-overlapping CANDELS-sized fields. While the five CANDELS fields are all rectangular, the aspect ratios range from 4.8:1 (EGS) to 1.6:1 (GOODS-N). For this exercise we chose to use a single field geometry with an area of 170 arcmin² and an aspect ratio of 3.1:1, which is the mean of the five fields. We were able to extract 39 non-overlapping fields of this size. The distribution of $z \sim 9$ galaxies per CANDELS field is shown in the left panel of Figure 23.

We find a median expectation of $2 \pm 2 z \approx 9$ galaxies per CANDELS field, highlighting that our discovery of seven such galaxies in the EGS field is an outlier. We find that in only two of these extracted SAM fields does the number of bright $z \sim 9$ galaxies match or exceed our detected value (one field with 7, and one with 8), with

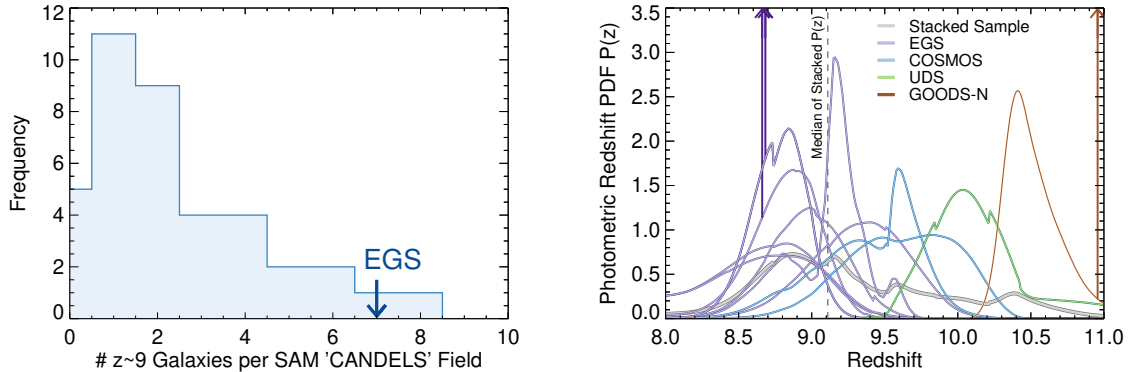


Figure 23. Left) The number of $z \approx 9$ galaxies per 170 arcmin^2 CANDELS-sized field extracted from a 2 deg^2 SAM mock catalog. Our observed value of seven such galaxies in the EGS field is more than 37 of the 39 extracted fields, implying that we are observing a true overdense structure at 95% confidence (encompassing both Poisson and cosmic variance uncertainties). Right) The photometric redshift probability distribution functions from our 11 candidates, with the EGS, COSMOS, UDS and GOODS-N objects shown in purple, blue, green and brown, respectively. We indicate the known spectroscopic redshift of EGS_z910.6811 ($z = 8.683$), EGS_z910.44164 ($z = 8.665$) and GOODS_N_z910.35589 ($z = 10.957$) with arrows. Five of the seven EGS candidates have photometric redshift PDFs which peak near to this spectroscopic redshift (with the other two EGS candidates still consistent with this redshift). This implies the large number of $z \sim 9$ candidates in the EGS field are part of a single overdense structure. The gray line in the background shows the normalized stacked PDF of the entire sample, highlighting the median redshift is 9.1.

37/39 fields having ≤ 6 galaxies. Thus, this simulation implies that observing a field with 7 bright $z \sim 9$ galaxies is a 95% (or 2σ) outlier, implying that it is fairly likely that we are witnessing a real structure in formation.

In the right panel of Figure 23 we show the photometric redshift distribution of galaxies in our sample, highlighting those in the EGS field in purple. While galaxies in our full sample have photometric redshift PDFs which span $z \sim 8.5-11$, five of the seven EGS candidates have PDFs which peak at $z \sim 8.5-9$ (with the other two candidates still having significant probability of a redshift in this range). Interestingly, two of these sources are EGS_z910.6811 which has a Ly α -based spectroscopic redshift of $z = 8.683$, and EGS_z910.44164 with a Ly α -based redshift of $z = 8.665$ (Larson et al. 2021). Detecting Ly α from such distant sources is suggestive that the source resides in a predominantly ionized bubble (e.g. Castellano et al. 2018; Tilvi et al. 2020), which are predicted to exist around over-densities throughout the epoch of reionization (e.g., Malhotra & Rhoads 2006; Dijkstra 2014). This apparent overdensity could be powering such an ionized bubble, which is considered further in Larson et al. (2021). If future spectroscopic followup finds that these sources are part of an overdense structure at $z \sim 8.7$, it explains why the EGS candidates are clustered at similar $J-H$ colors in Figure 8.

8. CONCLUSIONS

We have presented the results of a systematic search through the five CANDELS fields for galaxy candidates at $z > 8.5$. Due to the limited depth of many of these

fields, we limit our search to $H < 26.6$, which corresponds approximately to $S/N \sim 7$ for the shallowest regions of the CANDELS fields. We created new photometric catalogs in these fields, with an emphasis on color accuracy and minimizing spurious sources, and a detailed empirical estimation of the photometric noise. Each *HST* source had its *Spitzer*/IRAC photometry modeled with TPHOT, and we presented a discussion of the utility of IRAC data for the selection of such distant sources. We measured photometric redshifts for all sources in these catalogs with EAZY, justifying the inclusion of additional blue templates based on the measured colors of known $z > 6$ galaxies.

We selected candidate $z > 8.5$ galaxies with a customized set of selection criteria. We used source photometric redshift probability distribution functions to select sources likely at $z > 8.5$, sorting them into unity redshift bins based on where they had the majority of their redshift probability density. This led to an initial sample size of 140 candidates, which we thoroughly vetted in multiple ways.

As persistence from previous observations could leave a signature similar to a $z > 8.5$, we did a detailed screening for persistence, examining the pixel positions of our candidates in observations taken 24 hours prior to all of our exposures, and removing sources with high counts at these positions in previous images. We did an additional S/N check using noise measured in a local region to each source, ensuring that we included no spurious sources due to noisier-than-average regions. We then did a comprehensive visual inspection, exploring

both artifacts in *HST* imaging, and also removing candidates with poorly deblended IRAC photometry (unless the photometric redshift from *HST*-only satisfied our selection criteria). Finally, we explored the potential for stellar contamination fitting our candidates to low-mass star and brown dwarf spectral models. Our final sample after these screening steps was composed of 14 candidate galaxies.

We further vetted these candidates by including additional *HST* imaging in F098M and F140W, as well as including all available ground-based photometry. This step removed three sources. COSMOS_z910_14822 was the brightest source in our sample, but a combination of a weak detection in F098M and a red $H - K$ slope makes $z < 2.5$ more likely. After the inclusion of ground-based imaging, UDS_z910_731 was also removed as a likely low-redshift galaxy. Finally, UDS_z910_7815 was removed following a 2σ detection in the F098M image; while a high-redshift solution was still preferred for this galaxy, the difference between the goodness-of-fit for this solution and the best-fitting lower-redshift solution was only $\Delta\chi^2 = 0.9$, so this source was removed. As one final check, for our final sample of 11 sources, we remeasured the IRAC photometry using GALFIT to deblend and subtract neighbors, finding that in most cases objects were consistent with $z > 8.5$ regardless of which IRAC photometry was used. The exception was COSMOS_z910_20646, where the GALFIT photometry preferred a low-redshift solution. However given that it is unknown whether GALFIT or TPHOT are closer to the truth, we kept this source in our sample, noting this potential uncertainty on its redshift.

We presented a detailed comparison of our search to those in the literature. We find significant agreement amongst those studies which use photometric redshifts (e.g., Bouwens et al. 2019), noting that color-selection only would miss six of our 11 candidates, as shown in Figure 9 (e.g., Bouwens et al. 2016a). Most published sources not in our sample were simply fainter than our detection or S/N limits, though broadly our photometric redshifts for these sources are in agreement with those published.

We used the observed photometry to estimate the UV absolute magnitudes for our sources, calculating line-of-sight lensing due to any nearby neighbors in the imaging (finding no significant intermediate or strong lensing magnification). We then calculated the rest-frame UV luminosity function, using simulation-based values of the effective volume to correct for incompleteness. We pay particular attention to the sizes of simulated sources, ensuring that the recovered simulated sources match what little information we have about true bright $z > 8.5$

galaxies. Due to the small number of galaxies in our sample, we measure this luminosity function in a single redshift bin from $8.5 < z < 11$. We developed a novel method for calculating the observed number densities, minimizing any potential bias from choosing a specific set of magnitude bins.

Comparing to results in the literature over these same redshifts, we find general agreement with previous results within the large Poisson and cosmic variance uncertainties, though our brightest measurements are at the higher end of some previous results. Our observations support a seeming lack of evolution in the bright end of the UV luminosity function at $z > 8$, previously proposed by Bowler et al. (2020), where the decline in number density towards brighter luminosities appears shallower than the typical Schechter exponential decline. We compared our observed luminosity function to several recent theoretical models, finding that some under-predict the observed abundance in our brightest bin, though we find that a combination of either more efficient star formation in galaxies at this epoch and/or reduced dust in bright galaxies in this epoch can explain our observations.

Finally, we explored the distribution of our 11 candidates across the five CANDELS fields, noting that 7/11 were in a single field – the EGS. We used a SAM mock catalog to explore the expected distribution of such bright $z > 8.5$ galaxies in CANDELS-sized fields, and found that our detection of seven in a single field is a 2σ outlier (encompassing both Poisson and cosmic variance uncertainties). This implies that this overdensity is real, and we are witnessing the formation of one of the earliest cosmic structures. This is supported by the detection of Ly α emission from two of these galaxies at $z = 8.683$ (Zitrin et al. 2015) and $z = 8.665$ (Larson et al. 2021), which is consistent with the presence of an ionized bubble formed by this overdensity deep in the epoch of reionization.

We caution the reader that in spite of our extreme vetting process, 8/11 galaxies still lack spectroscopic confirmation and remain candidates, thus our conclusions should be weighed alongside the confidence in these candidates. Likewise, as discussed in detail in this paper, the selection of these sources with current telescopes is highly complex, with significant effort required to obtain a pure sample, which could lead to additional systematic uncertainties in the luminosity function calculation. Our ability to study this early epoch will soon receive a tremendous boost with the imminent launch of *JWST*. While its larger aperture will allow deeper surveys, the key advance is its ability to probe 1–5 μ m all at *HST* (or better) resolution, removing the hurdle of uncer-

tain IRAC deblending. All five CANDELS fields will receive significant imaging from approved Cycle 1 programs including JADES (PI Rieke), PRIMER (PI Dunlop), COSMOS-Webb (PIs Kartaltepe and Casey) and CEERS (PI Finkelstein). Early in Cycle 1 the CEERS program will observe the EGS field, probing the potential $z \sim 9$ overdensity by spectroscopically observing many of the known sources, and photometrically searching for fainter companions. While we and others have pushed *HST* to its limits to give us a first glimpse of the $z > 9$ universe, *JWST* observations will soon unlock the cosmic secrets hidden in this era.

We acknowledge that the location where most of this work took place, the University of Texas at Austin, that sits on indigenous land. The Tonkawa lived in central Texas and the Comanche and Apache moved through this area. We pay our respects to all the American Indian and Indigenous Peoples and communities who have been or have become a part of these lands and territories in Texas, on this piece of Turtle Island. We thank Adam Kraus, Karl Gebhardt, Stephen

Wilkins, Rebecca Bowler, Charlotte Mason, Jim Dunlop, and Gabe Brammer for helpful conversations. We thank the anonymous referee for their detailed and useful comments. SLF and MB acknowledge support from NASA through ADAP award 80NSSC18K0954. Support for *Hubble Space Telescope* programs #15697 and #15862 was provided by NASA through a grant from the Space Telescope Science Institute, which is operated by the Associations of Universities for Research in Astronomy, Incorporated, under NASA contract NAS5-26555. S.R.R. acknowledges financial support from the International Max Planck Research School for Astronomy and Cosmic Physics at the University of Heidelberg (IMPRS-HD). This research has benefitted from the SpeX Prism Library (and/or SpeX Prism Library Analysis Toolkit), maintained by Adam Burgasser at <http://www.browndwarfs.org/spexprism>

Software: EAZY (Brammer et al. 2008), SourceExtractor (v2.19.5; (Bertin & Arnouts 1996)), T-PHOT (Merlin et al. 2015, 2016), Galfit package (Peng et al. 2002), pypher (Boucaud et al. 2016)

REFERENCES

- Ashby, M. L. N., Willner, S. P., Fazio, G. G., et al. 2015, *ApJS*, 218, 33
- Atek, H., Richard, J., Jauzac, M., et al. 2015, *ApJ*, 814, 69
- Barro, G., Pérez-González, P. G., Cava, A., et al. 2019, *ApJS*, 243, 22
- Becker, G. D., Bolton, J. S., Madau, P., et al. 2015, *MNRAS*, 447, 3402
- Becker, G. D., D’Aloisio, A., Christenson, H. M., et al. 2021, arXiv e-prints, arXiv:2103.16610
- Beckwith, S. V. W., Stiavelli, M., Koekemoer, A. M., et al. 2006, *AJ*, 132, 1729
- Behroozi, P., Conroy, C., Wechsler, R. H., et al. 2020, *MNRAS*
- Behroozi, P. S., & Silk, J. 2015, *ApJ*, 799, 32
- Bernard, S. R., Carrasco, D., Trenti, M., et al. 2016, *ApJ*, 827, 76
- Bertin, E., & Arnouts, S. 1996, *A&AS*, 117, 393
- Bhowmick, A. K., Somerville, R. S., Di Matteo, T., et al. 2020, *MNRAS*, 496, 754
- Boucaud, A., Bocchio, M., Abergel, A., et al. 2016, PyPHER: Python-based PSF Homogenization kERnels
- Bouwens, R. J., Illingworth, G. D., Franx, M., & Ford, H. 2007, *ApJ*, 670, 928
- Bouwens, R. J., Illingworth, G. D., Oesch, P. A., et al. 2015a, *ApJ*, 811, 140
- Bouwens, R. J., Stefanon, M., Oesch, P. A., et al. 2019, arXiv e-prints, arXiv:1905.05202
- Bouwens, R. J., Illingworth, G. D., Oesch, P. A., et al. 2014, *ApJ*, 793, 115
- . 2015b, *ApJ*, 803, 34
- Bouwens, R. J., Oesch, P. A., Labbé, I., et al. 2016a, *ApJ*, 830, 67
- . 2016b, *ApJ*, 830, 67
- Bouwens, R. J., Oesch, P. A., Stefanon, M., et al. 2021, arXiv e-prints, arXiv:2102.07775
- Bowler, R. A. A., Jarvis, M. J., Dunlop, J. S., et al. 2020, *MNRAS*, 493, 2059
- Bowler, R. A. A., Dunlop, J. S., McLure, R. J., et al. 2012, *MNRAS*, 426, 2772
- . 2014, *MNRAS*, 440, 2810
- . 2015, ArXiv e-prints
- Brammer, G. B., van Dokkum, P. G., & Coppi, P. 2008, *ApJ*, 686, 1503
- Bridge, J. S., Holwerda, B. W., Stefanon, M., et al. 2019, *ApJ*, 882, 42
- Bruzual, G., & Charlot, S. 2003, *MNRAS*, 344, 1000
- Burgasser, A. J. 2014, in *Astronomical Society of India Conference Series*, Vol. 11, *Astronomical Society of India Conference Series*, 7–16
- Calvi, V., Trenti, M., Stiavelli, M., et al. 2016, *ApJ*, 817, 120

- Cardelli, J. A., Clayton, G. C., & Mathis, J. S. 1989, *ApJ*, 345, 245
- Casey, C. M., Narayanan, D., & Cooray, A. 2014, *PhR*, 541, 45
- Castellano, M., Pentericci, L., Vanzella, E., et al. 2018, *ApJL*, 863, L3
- Conroy, C., & Gunn, J. E. 2010, *FSPS: Flexible Stellar Population Synthesis*
- DeSantis, Z. J., Thurman, S. T., Hix, T. T., & Ogden, C. E. 2017, in *Advanced Maui Optical and Space Surveillance (AMOS) Technologies Conference*, ed. S. Ryan, 26
- Dijkstra, M. 2014, *PASA*, 31, 40
- Ellis, R. S., McLure, R. J., Dunlop, J. S., et al. 2013, *ApJL*, 763, L7
- Elvis, M., Civano, F., Vignali, C., et al. 2009, *ApJS*, 184, 158
- Erb, D. K., Pettini, M., Shapley, A. E., et al. 2010, *ApJ*, 719, 1168
- Fan, X., Strauss, M. A., Becker, R. H., et al. 2006, *AJ*, 132, 117
- Finkelstein, K. D., Finkelstein, S. L., Tilvi, V., et al. 2015a, *ApJ*, 813, 78
- Finkelstein, S., Dickinson, M., Ferguson, H., et al. 2017, *The Cosmic Evolution Early Release Science (CEERS) Survey, JWST Proposal ID 1345. Cycle 0 Early Release Science*
- Finkelstein, S. L. 2016, *PASA*, 33, e037
- Finkelstein, S. L., Papovich, C., Giavalisco, M., et al. 2010, *ApJ*, 719, 1250
- Finkelstein, S. L., Papovich, C., Ryan, R. E., et al. 2012a, *ApJ*, 758, 93
- Finkelstein, S. L., Papovich, C., Salmon, B., et al. 2012b, *ApJ*, 756, 164
- Finkelstein, S. L., Song, M., Behroozi, P., et al. 2015b, *ApJ*, 814, 95
- Finkelstein, S. L., Ryan, Jr., R. E., Papovich, C., et al. 2015c, *ApJ*, 810, 71
- Finkelstein, S. L., D'Aloisio, A., Paardekooper, J.-P., et al. 2019, *ApJ*, 879, 36
- Fontana, A., Dunlop, J. S., Paris, D., et al. 2014, *A&A*, 570, A11
- Galametz, A., Grazian, A., Fontana, A., et al. 2013, *ApJS*, 206, 10
- Giavalisco, M., Ferguson, H. C., Koekemoer, A. M., et al. 2004a, *ApJL*, 600, L93
- Giavalisco, M., Dickinson, M., Ferguson, H. C., et al. 2004b, *ApJL*, 600, L103
- Gnedin, N. Y. 2016, *ApJL*, 825, L17
- Graham, A. W., Driver, S. P., Petrosian, V., et al. 2005, *AJ*, 130, 1535
- Grogin, N. A., Kocevski, D. D., Faber, S. M., et al. 2011, *ApJS*, 197, 35
- Guo, Y., Ferguson, H. C., Giavalisco, M., et al. 2013, *ApJS*, 207, 24
- Ishigaki, M., Kawamata, R., Ouchi, M., et al. 2018, *ApJ*, 854, 73
- Jiang, L., Kashikawa, N., Wang, S., et al. 2021, *Nature Astronomy*, 5, 256
- Kawamata, R., Ishigaki, M., Shimasaku, K., et al. 2018, *ApJ*, 855, 4
- Kennicutt, Robert C., J. 1989, *ApJ*, 344, 685
- Kennicutt, Robert C., J., & De Los Reyes, M. A. C. 2021, *ApJ*, 908, 61
- Kocevski, D. D., Hasinger, G., Brightman, M., et al. 2018, *ApJS*, 236, 48
- Koekemoer, A. M., Faber, S. M., Ferguson, H. C., et al. 2011, *ApJS*, 197, 36
- Kulkarni, G., Keating, L. C., Haehnelt, M. G., et al. 2018, *arXiv e-prints*
- Labbé, I., Franx, M., Rudnick, G., et al. 2007, *ApJ*, 665, 944
- Laporte, N., Meyer, R. A., Ellis, R. S., et al. 2021, *arXiv e-prints*, arXiv:2104.08168
- Larson, R., Finkelstein, S. L., Hutchison, T., et al. 2021, *ApJ Submitted*
- Lawrence, A., Warren, S. J., Almaini, O., et al. 2007, *MNRAS*, 379, 1599
- Livermore, R. C., Finkelstein, S. L., & Lotz, J. M. 2017, *ApJ*, 835, 113
- Lotz, J. M., Koekemoer, A., Coe, D., et al. 2017, *ApJ*, 837, 97
- Ma, X., Hopkins, P. F., Garrison-Kimmel, S., et al. 2018, *MNRAS*, 478, 1694
- Mainali, R., Zitrin, A., Stark, D. P., et al. 2018, *MNRAS*, 479, 1180
- Malhotra, S., & Rhoads, J. E. 2006, *ApJL*, 647, L95
- Mason, C. A., Trenti, M., & Treu, T. 2015a, *ApJ*, 813, 21
- Mason, C. A., Treu, T., Schmidt, K. B., et al. 2015b, *ArXiv e-prints*
- McCracken, H. J., Milvang-Jensen, B., Dunlop, J., et al. 2012, *A&A*, 544, A156
- McLeod, D. J., McLure, R. J., & Dunlop, J. S. 2016, *ArXiv e-prints*
- McLeod, D. J., McLure, R. J., Dunlop, J. S., et al. 2015, *MNRAS*, 450, 3032
- McLure, R. J., Cirasuolo, M., Dunlop, J. S., Foucaud, S., & Almaini, O. 2009, *MNRAS*, 395, 2196
- McLure, R. J., Dunlop, J. S., Cirasuolo, M., et al. 2010, *MNRAS*, 403, 960
- McLure, R. J., Dunlop, J. S., Bowler, R. A. A., et al. 2013, *MNRAS*, 432, 2696

- Merlin, E., Fontana, A., Ferguson, H. C., et al. 2015, ArXiv e-prints
- Merlin, E., Bourne, N., Castellano, M., et al. 2016, *A&A*, 595, A97
- Miralda-Escudé, J., & Rees, M. J. 1998, *ApJ*, 497, 21
- Momcheva, I. G., Brammer, G. B., van Dokkum, P. G., et al. 2016, *ApJS*, 225, 27
- Morishita, T., Trenti, M., Stiavelli, M., et al. 2018, *ApJ*, 867, 150
- Naidu, R. P., Tacchella, S., Mason, C. A., et al. 2020, *ApJ*, 892, 109
- Nandra, K., Laird, E. S., Aird, J. A., et al. 2015, *ApJS*, 220, 10
- Narayanan, D., Krumholz, M. R., Ostriker, E. C., & Hernquist, L. 2012, *MNRAS*, 421, 3127
- Nayyeri, H., Hemmati, S., Mobasher, B., et al. 2017, *ApJS*, 228, 7
- Oesch, P. A., Bouwens, R. J., Illingworth, G. D., Labbé, I., & Stefanon, M. 2018, *ApJ*, 855, 105
- Oesch, P. A., Bouwens, R. J., Illingworth, G. D., et al. 2013, *ApJ*, 773, 75
- . 2014, *ApJ*, 786, 108
- Oesch, P. A., Brammer, G., van Dokkum, P. G., et al. 2016, *ApJ*, 819, 129
- Paardekooper, J.-P., Khochfar, S., & Dalla Vecchia, C. 2015, *MNRAS*, 451, 2544
- Papovich, C., Shipley, H. V., Mehtens, N., et al. 2016, *ApJS*, 224, 28
- Patten, B. M., Stauffer, J. R., Burrows, A., et al. 2006, *ApJ*, 651, 502
- Peng, C. Y., Ho, L. C., Impey, C. D., & Rix, H.-W. 2002, *AJ*, 124, 266
- Peng, Y.-j., Lilly, S. J., Kovač, K., et al. 2010, *ApJ*, 721, 193
- Pentericci, L., Vanzella, E., Castellano, M., et al. 2018, ArXiv e-prints
- Planck Collaboration, Aghanim, N., Ashdown, M., et al. 2016, *A&A*, 596, A107
- Planck Collaboration, Aghanim, N., Akrami, Y., et al. 2020, *A&A*, 641, A6
- Roberts-Borsani, G., Morishita, T., Treu, T., Leethochawalit, N., & Trenti, M. 2021, arXiv e-prints, arXiv:2106.06544
- Roberts-Borsani, G. W., Ellis, R. S., & Laporte, N. 2020, *MNRAS*, 497, 3440
- Roberts-Borsani, G. W., Bouwens, R. J., Oesch, P. A., et al. 2016, *ApJ*, 823, 143
- Robertson, B. E., Ellis, R. S., Furlanetto, S. R., & Dunlop, J. S. 2015, *ApJL*, 802, L19
- Robertson, B. E., Furlanetto, S. R., Schneider, E., et al. 2013, *ApJ*, 768, 71
- Rojas-Ruiz, S., Finkelstein, S. L., Bagley, M. B., et al. 2020, *ApJ*, 891, 146
- Ryan, R. E., J., & Reid, I. N. 2016, *AJ*, 151, 92
- Schmidt, K. B., Treu, T., Trenti, M., et al. 2014, *ApJ*, 786, 57
- Schmidt, M. 1959, *ApJ*, 129, 243
- Shibuya, T., Ouchi, M., Kubo, M., & Harikane, Y. 2016, *ApJ*, 821, 72
- Somerville, R. S., Popping, G., & Trager, S. C. 2015, *MNRAS*, 453, 4337
- Somerville, R. S., Olsen, C., Yung, L. Y. A., et al. 2021, *MNRAS*, 502, 4858
- Song, M., Finkelstein, S. L., Ashby, M. L. N., et al. 2016, *ApJ*, 825, 5
- Spitler, L. R., Labbé, I., Glazebrook, K., et al. 2012, *ApJ*, 748, L21
- Stefanon, M., Bouwens, R. J., Labbé, I., et al. 2017a, *ApJ*, 843, 36
- Stefanon, M., Yan, H., Mobasher, B., et al. 2017b, *ApJS*, 229, 32
- Stefanon, M., Labbé, I., Bouwens, R. J., et al. 2019, *ApJ*, 883, 99
- Steidel, C. C., & Hamilton, D. 1993, *AJ*, 105, 2017
- Stevans, M. L., Finkelstein, S. L., Kawinwanichakij, L., et al. 2021, arXiv e-prints, arXiv:2103.14690
- Straatman, C. M. S., Labbé, I., Spitler, L. R., et al. 2014, *ApJL*, 783, L14
- Tacchella, S., Bose, S., Conroy, C., Eisenstein, D. J., & Johnson, B. D. 2018, *ApJ*, 868, 92
- Tacchella, S., Finkelstein, S. L., Finkelstein, S. L., et al. 2021, *ApJ* Submitted
- Tilvi, V., Malhotra, S., Rhoads, J. E., et al. 2020, *ApJL*, 891, L10
- Trenti, M., Bradley, L. D., Stiavelli, M., et al. 2011, *ApJL*, 727, L39
- Treu, T., Abramson, L., Bradac, M., et al. 2017, Through the Looking GLASS: A JWST Exploration of Galaxy Formation and Evolution from Cosmic Dawn to Present Day, JWST Proposal ID 1324. Cycle 0 Early Release Scienc
- Vijayan, A. P., Lovell, C. C., Wilkins, S. M., et al. 2020, *MNRAS*
- Vogelsberger, M., Nelson, D., Pillepich, A., et al. 2020, *MNRAS*, 492, 5167
- Whitaker, K. E., Labbé, I., van Dokkum, P. G., et al. 2011, *ApJ*, 735, 86
- Wilkins, S. M., Bouwens, R. J., Oesch, P. A., et al. 2016, *MNRAS*, 455, 659
- Wilkins, S. M., Feng, Y., Di Matteo, T., et al. 2017, *MNRAS*, 469, 2517

- Williams, C. C., Curtis-Lake, E., Hainline, K. N., et al. 2018, *ApJS*, 236, 33
- Windhorst, R. A., Cohen, S. H., Hathi, N. P., et al. 2011, *ApJS*, 193, 27
- Wold, I. G. B., Kawinwanichakij, L., Stevans, M. L., et al. 2019, *ApJS*, 240, 5
- Xu, H., Wise, J. H., Norman, M. L., Ahn, K., & O'Shea, B. W. 2016, *ApJ*, 833, 84
- Xue, Y. Q., Luo, B., Brandt, W. N., et al. 2016, *ApJS*, 224, 15
- Yang, S., Somerville, R. S., Pullen, A. R., et al. 2021, *ApJ*, 911, 132
- Yung, L. Y. A., Somerville, R. S., Finkelstein, S. L., Popping, G., & Davé, R. 2019, *MNRAS*, 483, 2983
- Yung, L. Y. A., Somerville, R. S., Finkelstein, S. L., et al. 2020, *MNRAS*, 496, 4574
- Zitrin, A., Labbé, I., Belli, S., et al. 2015, *ApJL*, 810, L12

Table 11. Sources Removed Due to Poor IRAC Deblending

| Field | ID | RA | Dec | $\int_8^{15} \mathcal{D}(z)$ | $\int_8^{15} \mathcal{D}(z)$ |
|--------|--------------------|------------|------------|------------------------------|------------------------------|
| | Limiting | J2000 | J2000 | with IRAC | without IRAC |
| EGS | 3509 | 214.790502 | 52.707862 | 0.77 | 0.03 |
| EGS | 35139 | 215.191622 | 53.071285 | 0.77 | 0.25 |
| EGS | 31599 | 214.809988 | 52.809716 | 0.68 | 0.43 |
| EGS | 61167 | 215.079527 | 53.047774 | 0.98 | 0.20 |
| EGS | 20183 | 215.252461 | 53.078172 | 0.99 | 0.37 |
| UDS | 20515 | 34.382023 | -5.170840 | 1.00 | 0.25 |
| UDS | 29638 | 34.371719 | -5.192273 | 0.97 | 0.17 |
| UDS | 51959 | 34.406923 | -5.128847 | 0.93 | 0.36 |
| UDS | 54956 | 34.479757 | -5.136519 | 0.76 | 0.06 |
| UDS | 11227 | 34.490247 | -5.251716 | 1.00 | 0.24 |
| UDS | 66769 | 34.400905 | -5.162690 | 0.98 | 0.02 |
| UDS | 34040 | 34.329161 | -5.200860 | 0.99 | 0.31 |
| COSMOS | 10736 | 150.074713 | 2.216529 | 1.00 | 0.00 |
| COSMOS | 14117 | 150.182930 | 2.230231 | 0.96 | 0.04 |
| COSMOS | 23915 | 150.068259 | 2.279747 | 1.00 | 0.13 |
| COSMOS | 21434 | 150.060263 | 2.267318 | 0.99 | 0.28 |
| COSMOS | 34603 | 150.153627 | 2.327952 | 1.00 | 0.30 |
| COSMOS | 48148 | 150.054342 | 2.389392 | 0.90 | 0.02 |
| COSMOS | 22810 | 150.063056 | 2.274242 | 1.00 | 0.25 |
| COSMOS | 22221 | 150.055009 | 2.271304 | 1.00 | 0.11 |
| COSMOS | 48048 | 150.075835 | 2.388783 | 0.98 | 0.30 |
| GOODSN | 32862 | 189.466464 | 62.236057 | 1.00 | 0.43 |
| GOODSN | 33625 | 189.464511 | 62.237533 | 0.89 | 0.00 |
| GOODSN | 36090 | 189.323657 | 62.377288 | 1.00 | 0.43 |
| GOODSS | 50435 | 53.171530 | -27.717057 | 1.00 | 0.38 |
| GOODSS | 44740 [†] | 53.094458 | -27.739336 | 0.00 | 0.90 |

NOTE—[†]This source formally satisfies the sample selection criteria without IRAC. However, it is obvious in the image that this source is extremely bright in IRAC (even with the poor deblending), thus we conclude it is very likely to reside at low redshift.

APPENDIX

A. VISUALLY REMOVED SOURCES

In this section of the appendix, we show cutout images of any sources removed from our sample following any kind of subjective visual inspection. Figure 24 shows sources visually identified as diffraction spikes, oversplit portions of nearby galaxies, or “Junk”, which denotes any other kind of non-real source, typically due to increased noise in the region around a given object. This process is discussed in §3.3. Figure 25 shows objects removed after visual inspection determined that the TPHOT IRAC deblending was unreliable, and the sources did not satisfy our photometric redshift selection criteria when excluding the IRAC photometry. Some of these may yet be real $z > 8.5$ sources, but for our conservative analysis, we remove them. These sources are listed in Table 11.

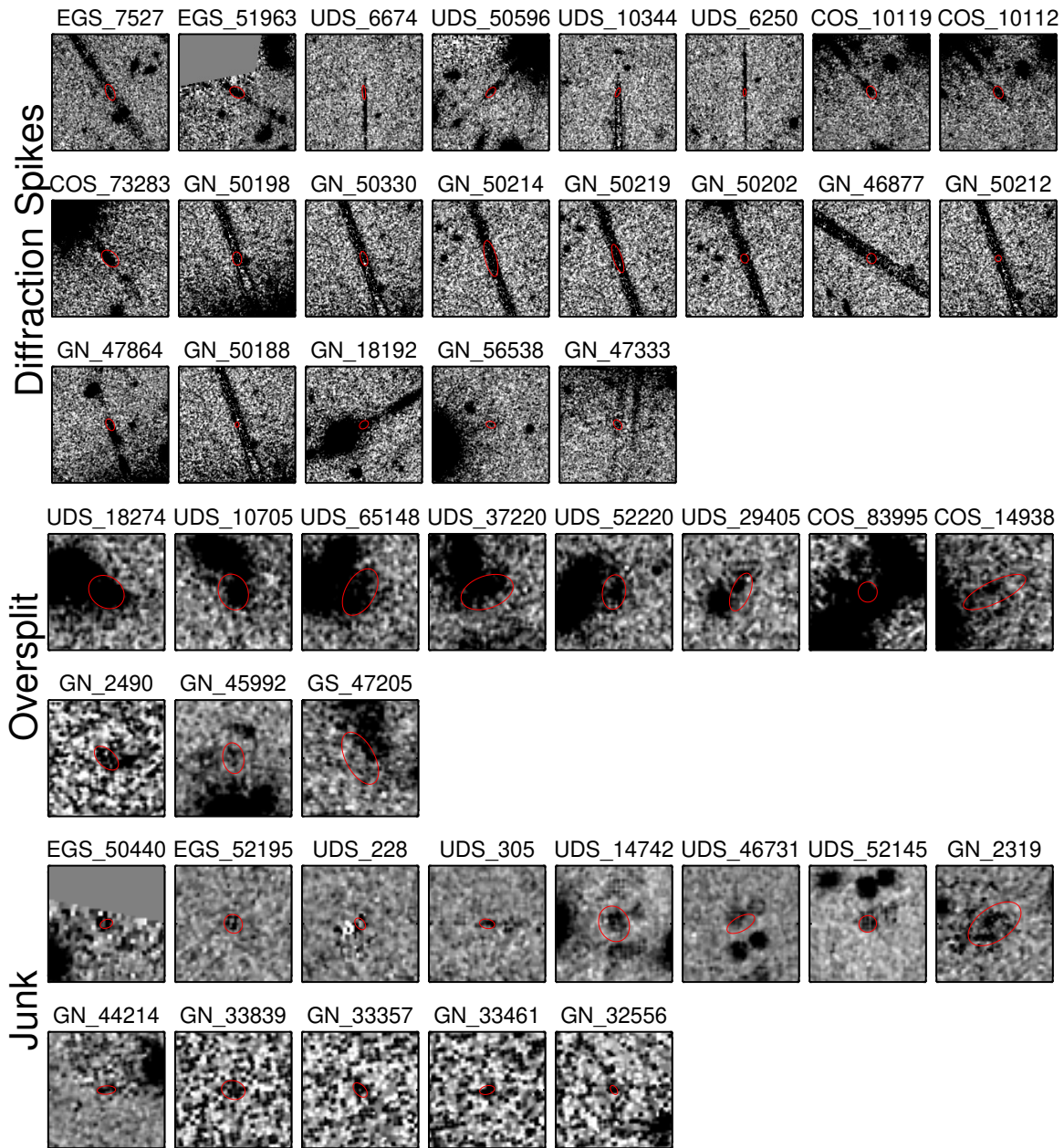


Figure 24. Objects removed from our initial sample following visual inspection. In the top section, images are $9''$ in length, while they are $3''$ in the remaining two sections. In all cutout images the red ellipses denotes the small Kron aperture identified for the source. The titles for each image show the field it was detected in, and its identification number in our photometric catalog. The top section shows objects identified as being a part of a diffraction spike. The middle section shows objects identified as being an oversplit region of a nearby bright galaxy. The bottom section shows other objects determined to be non-real sources, either due to residing near an image edge or other region of enhanced noise, missed persistence (in the case of the UDS objects), or having a morphology inconsistent with a real galaxy, indicative of an image defect.

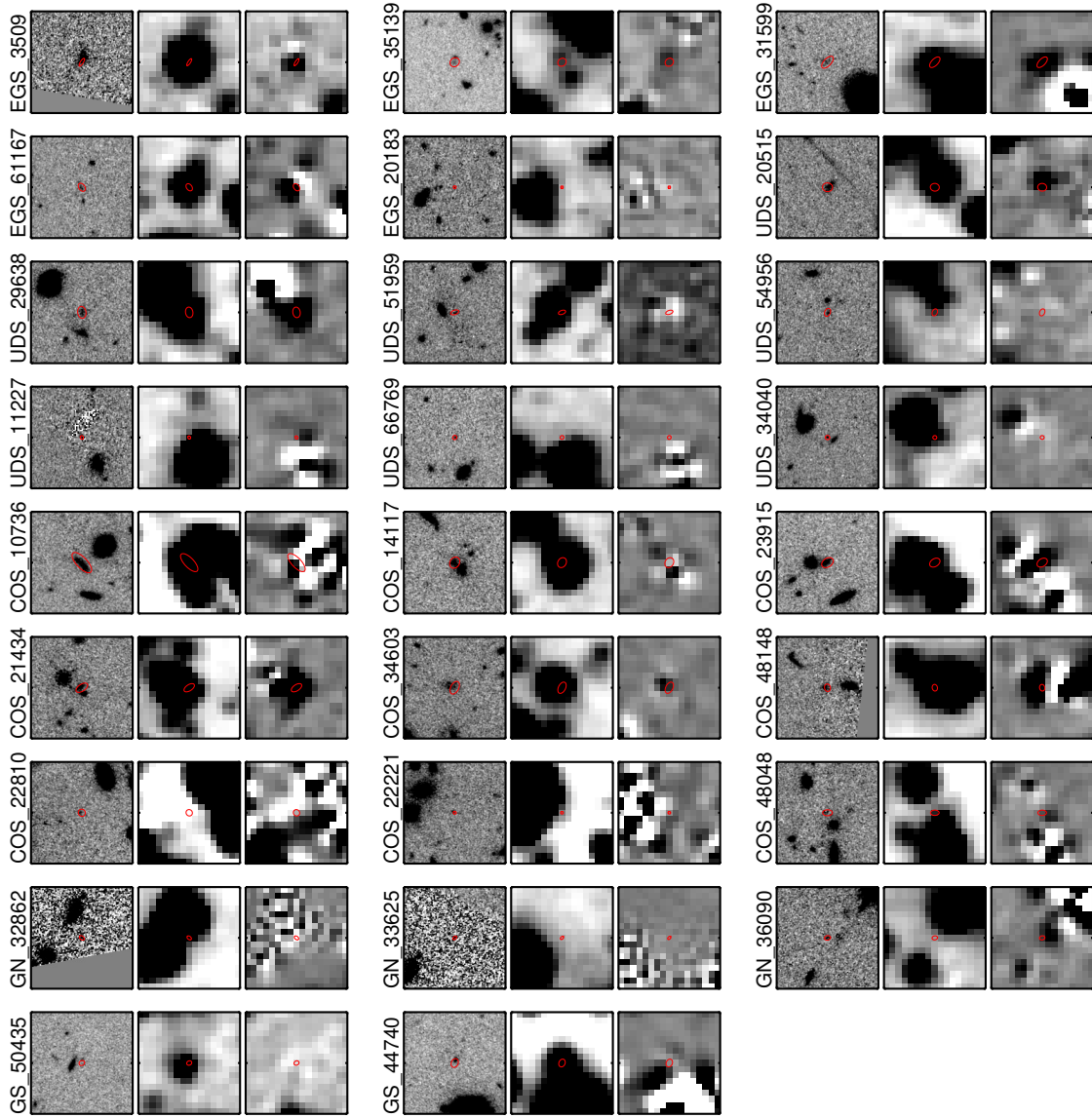


Figure 25. Cutout images of the 26 objects removed from our sample when visual inspection determined that the TPHOT deblended IRAC photometry was unreliable, and the photometric redshift probability distribution function without the IRAC photometry did not satisfy our sample selection criteria. From left-to-right, for each object we show the H_{160} -band image, the $3.6\mu\text{m}$ image, and the $3.6\mu\text{m}$ residual image, where the source of interest was not subtracted (the *HST* and IRAC cutouts are $9''$ and $10''$, respectively).